MODELLING AND CONTROL OF MULTI-MODE MOTION OCEAN WAVE ENERGY CONVERTERS

by

ZHIJING LIAO

Submitted in fulfillment of the requirements of the Degree of

Doctor of Philosophy

School of Engineering and Materials Science

Queen Mary University of London

United Kingdom

2021

Statement of originality

I, Zhijing Liao, confirm that the research included within this thesis is my own work or that where it has been carried out in collaboration with, or supported by others, that this is duly acknowledged below and my contribution indicated. Previously published material is also acknowledged below.

I attest that I have exercised reasonable care to ensure that the work is original, and does not to the best of my knowledge break any UK law, infringe any third party's copyright or other Intellectual Property Right, or contain any confidential material.

I accept that the College has the right to use plagiarism detection software to check the electronic version of the thesis.

I confirm that this thesis has not been previously submitted for the award of a degree by this or any other university.

The copyright of this thesis rests with the author and no quotation from it or information derived from it may be published without the prior written consent of the author.

Signature: Zhijing Liao

Date: 01/05/2021

Details of collaboration and publications:

- Z. Liao, N. Gai, P. Stansby, and G. Li, "Control-oriented modelling of wave energy converter M4." Taipei, Taiwan: *Asian Wave and Tidal Energy Confer-*

ence, 2018.

- Z. Liao, N. Gai, P. Stansby, and G. Li. "Linear non-causal optimal control of an attenuator type wave energy converter M4." *IEEE Transactions on Sustainable Energy*, pages 1–1, 2019.

- Z. Liao, P. Stansby, and G. Li. A generic linear non-causal optimal control framework integrated with wave excitation force prediction for multi-mode wave energy converters with application to M4. *Applied Ocean Research*, 97:102056, 2020.

- Z. Liao, P. Stansby, G. Li and E. Carpintero. Moreno. "High-capacity wave energy conversion by multi-float, multi-PTO, control and prediction: generalised state-space modelling with linear optimal control and arbitrary headings." *IEEE Transactions on Sustainable Energy, accepted.*, 2021.

Abstract

This thesis deals with the modelling and control problems for the multi-mode motion wave energy converters (WECs). This type of WEC has a higher potential power capture capability but involves hydrodynamic models of increased complexity. A typical multi-mode motion WEC, namely M4, is chosen for this case study.

In the first part, the hydrodynamics of M4 are analysed. A control-oriented state-space model is then built for the purpose of controller design. This is done by firstly using the Euler-Lagrangian equation to derive the motion equation on a constrained coordinate. A system identification method is then introduced to model the radiation effects, and a model order reduction method is used to reduce the order of the radiation subsystems. The fidelity of the derived state-space model is validated against experimental data.

In the second part, the linear non-causal optimal control (LNOC) framework is designed to tackle the energy maximising problem of the M4 WEC. This framework has three key components: a linear optimal controller, a Kalman filter with a random-walk wave-force model to estimate the system states and wave excitation force and an excitation-force predictor based on an autoregressive (AR) model. Their mathematical formulations are presented, followed by numerical simulations to demonstrate the control performance of the integrated framework. The results show that the AR wave excitation force predictor can provide preview wave force information accurately for around 2 peak periods of time, which is sufficient for control. The LNOC framework can effectively improve the energy conversion of M4 without introducing significant costs in terms of extra hardware components and

computational loads.

In the last part, a variation of the M4 design, with four power take-offs (PTOs) instead of one, is studied. The goal is to showcase that the energy conversion capacity of a multi-PTO M-WEC, integrated with the LNOC framework, can be similar to that of an offshore wind turbine, which is desirable for electricity supply to the power grid. The effect of off-design, arbitrary WEC headings in various incoming wave direction is investigated as a vital sensitivity check to provide useful quantification for implementing the LNOC framework in practice. The improvement of captured power by the LNOC framework in all cases is shown to be substantial.

To my family and my fiancée Shushu.

Acknowledgements

Firstly, I would like to express sincere gratitude to my research advisor Dr Guang Li for the continuous support of my PhD study and research. I also thank him for introducing me to an exciting and challenging research area and providing me the opportunities to work with many excellent researchers. He has been a helpful and professional mentor on my research as well as a dear friend who offers motivation and inspiration at times I need them most.

Besides, I would also like to thank all my colleagues from Dr Li's control group. I appreciate their company and feedback on my research work. In particular, I would like to thank Siyuan Zhan, Yingbo Huang, Yao Zhang, Sajjad and Salman. I learn so much from their work and their company have been enjoyable. I also thank Dr Zhenchun Wang, who taught me a lot in hardware and experiments.

Finally, I express my deepest gratitude to my family for their unconditional support and love.

Contents

List of Figures

List of Tables

Abbreviations

WEC: Wave Energy Converter

S-WEC: Single-mode Motion Wave Energy Converter

M-WEC: Multi-mode Motion Wave Energy Converter

PTO: Power Take-Off

LCOE: Levelised Cost Of Electricity LNOC: Linear Non-causal Optimal Control

DARE: Discrete-time Riccati Equation

DP: Dynamic Programming

AR: Autoregressive

MPC: Model Predictive Control

CWR: Capture Width Ratio

JONSWAP: Joint North Sea Wave Observation Project

Chapter 1

Introduction

This thesis is concerned with the modelling and control of a raft-type wave energy converter, which can be referred to as an attenuator. This multi-mode motion attenuator's idealised power capture is higher than that of a single-mode motion point absorber. However, the dynamic modelling and control design is more challenging in a multi-mode attenuator. In this thesis, a time-domain control-oriented modelling method is introduced. Based on this model, a generic linear non-causal optimal control framework is proposed to tackle the attenuator's energy maximisation control problem. Three of the key components in this framework (the optimal controller, the state and wave force estimator and the wave force predictor) are investigated. In this chapter, the motivation for this work is addressed. Also, the thesis structure is presented.

1.1 Motivation

To meet the increasing demand of electricity globally and slow down global warming caused by coal power generation, renewable energy technology has been developed rapidly in the past few decades. In 2018, 25.8% of world electricity was generated by renewable sources; this number was only 18.7% in 2000 [1]. This number has continued to increase rapidly, reaching 27.3% in 2019 [2], due mainly to contributions from hydro and wind power.

Ocean wave energy has an untapped potential to contribute even more as a renewable energy source. Ocean wave power has a worldwide average of about 2 TW [3], which is similar to wind and largely unexploited. Wave energy converter (WEC) device capacities have been much smaller than those of wind turbines [4] and with higher levelised cost of electricity (LCOE). Research in wave energy and wave energy harnessing technology have been actively conducted in recent years. The design of wave energy harnessing devices with higher potential capacities and their integration with advanced control strategies are believed to be two key factors for reducing the LCOE of wave energy.

WECs are devices of various design that can turn the motion of ocean waves into usable electrical power. This conversion process can usually be divided into two phases: (1) the WEC captures the power contained in the ocean wave and turns it into mechanical power with the WEC body or a hydro turbine; (2) an electricity generation system, also known as the power-take-off (PTO) system, utilizes this mechanical power to generate electricity that can be stored or transferred directly to the power grid. Power conversion efficiency is vital at either phase, and technologies from various disciplines are needed to improve them.

Control has been found to be critically important to improve the power conversion efficiency of WECs. One reason is that a WEC device, as a mechanical oscillator, has a fixed natural frequency of vibration, while the frequencies of ocean waves are subject to change. Without active control, it is difficult to match the WEC's natural frequency to the dominant frequency of the ocean waves; thus, a resonance effect, which would imply maximal power conversion, cannot be achieved. Moreover, WECs operate in a harsh ocean environment. Introducing active control strategies to WECs enable them to handle tough operational constraints and protect themselves against destructive sea conditions, which helps reduce their operational costs and thus the LCOE. The power conversion of WECs also benefits from a prediction of future wave status, which cannot be achieved without active control. Like most of the studies conducted in the WEC control domain, this thesis's primary focus is maximizing the power conversion efficiency of phase one (i.e., the conversion

of wave power to the mechanical power of the WEC).

Unlike wind or solar energy, the development of wave energy technology tends to be very diversified. There are a remarkable number of design concepts of WECs that can be classified in different ways, such as by their operation location, working principle, degrees of freedom (DOFs) of body motions, etc. Figure 1.1 shows five typical types of WECs classified by their working principle of converting wave power. A point absorber converts wave power into a heave motion of the float. Attenuator and inverted pendulum designs convert wave power into rotational motion of the bodies. Overtopping devices and oscillating water columns convert wave power to the kinetic power of their turbines.

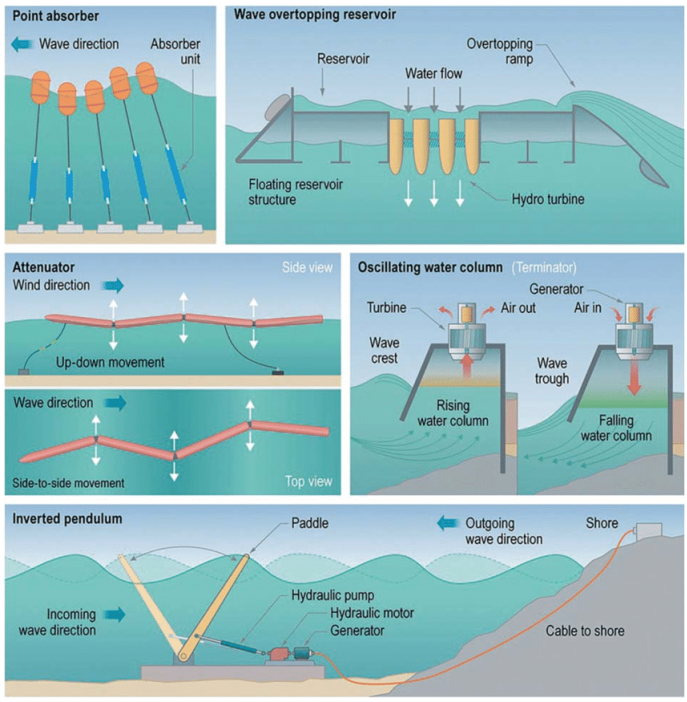

Figure 1.1: Typical types of wave energy converters classified by working principle [5].

In this thesis, WECs are distinguished based on the DOFs their body motion has because this determines their theoretical limit of power conversion [6]. WECs with motion with only one DOF are termed single-mode motion WECs (S-WEC), such as single-mode point absorber. WECs with more than one DOF of motion are

termed multi-mode motion WECs (M-WEC). Two types of WECs will be discussed primarily: the single-mode motion point absorber and the multi-mode motion attenuator. Although attenuators have higher power conversion efficiency due to their added DOFs of motion, most control research for WEC still focusses on S-WECs, such as point absorbers. This is probably because the dynamics of M-WECs are more complicated, which makes modelling and controller design more challenging.

We aim to fill this gap by investigating the difficulties in modelling and control design for M-WECs. A generic linear non-causal optimal control (LNOC) framework is proposed to tackle the energy maximising problem of M-WECs. Although this framework can also be applied to S-WEC, an M-WEC called M4 is chosen as a case study. This involves introducing a time-domain control-oriented modelling method to deal with the high- order dynamics modelling problem, whose efficacy is quantified against experimental data. The enabling components of the LNOC framework, including the non-causal optimal controller, a state and wave force estimator and a wave force predictor are introduced in proper order. Numerical simulations are used to demonstrate the efficacy of the control framework. Unlike the symmetrical S-WEC point absorber, various incoming wave directions have a greater impact on the performance of the asymmetric M-WEC. This effect is also examined within the LNOC framework by applying it to a multiple PTO M4 WEC as a sensitivity study.

1.2 Thesis layout

The content of this thesis is organised as follows.

In Chapter 2, more technical background on WECs is introduced. Firstly, the differences between a single-mode motion point absorber WEC and a multi-mode motion raft-type WEC is briefly explained. Then, the multiple floats multi-mode motion WEC M4 is introduced. Finally, existing control strategies from the literature are reviewed.

In Chapter 3, based on the linear wave assumption, the control-oriented model of the M4 WEC is built. A time-domain method is adopted, and the model is

presented in state-space form, which is idealised for controller design. Experimental data from tank testing of the M4 WEC are used to validate model fidelity.

In Chapter 4, the LNOC framework is proposed with details. The control problem is formulated in a classical optimal control fashion using the control-oriented state-space model in discrete time. The control policy is then derived using dynamic programming. A Kalman observer is designed to provide state information in real time. At this stage, the wave force prediction information is assumed to be ideal. This allows numerical simulations to be run to quantify the performance of this non-causal optimal controller.

In Chapter 5, the LNOC framework is completed by introducing a short-term wave predictor using the autoregressive model. Since this is a relatively independent research area, an introduction is presented to clarify some important concepts, and then the existing wave prediction techniques are surveyed. Subsequently, the autoregressive wave force predictor and the Kalman state and wave force estimator are proposed to accomplish the LNOC framework, followed by more numerical simulation results to demonstrate its efficacy. The computational effectiveness is briefly discussed as well.

In Chapter 6, a more sophisticated configuration of the M4 WEC, the 8-float M4 with four PTOs, is studied. This aims to showcase that by integrating an M-WEC with multi-PTO and the advanced LNOC framework, the capacity of wave energy can be similar or even greater than offshore wind turbines. The performance in off-design, non-zero headings scenarios for this prototype with LNOC is also studied as an important sensitivity check.

In Chapter 7, the main results of this thesis will be concluded, and potential future work is discussed.

Chapter 2

Wave Energy Conversion: a review of the current state of the art

Structures that absorb wave power by their body motion also generate waves during operation, termed radiated waves. Generally speaking, good wave absorbers must be good wave makers [6]. The upper limit of power conversion of WECs is different, and this is closely related to their capabilities of radiating waves. To reach a power absorption of above 50%, asymmetric waves have to be radiated, but this cannot be done by an S-WEC with a symmetrical body that operating only one DOF. Hence, WECs that have multiple DOFs of motion have higher idealised power capture.

Most of the existing WEC developments have come from S-WEC of point absorber form, e.g. AWS [7], Corpower [8], Seabased [9], Ocean Energy [10]. For an S-WEC operating only in heave mode, the idealised power capture due to body motion in regular waves is equal to propagating wave power per metre crest width times wavelength divided by 2π [7, 8, 9]. This value is multiplied by two when operating in surge or pitch and multiplied by three when operating in heave and surge and/or pitch. The theory has been reviewed in [6]. For raft-type devices with two hinged beams, the limit is slightly less, shown theoretically in [11]. There are hybrid raft-type devices with heave, pitch and surge forcing, such as Seapower [12], Mocean [13] and the M4 [14, 15] discussed in the next section. Examples of some

S-WECs are shown in Fig. 2.1 and some M-WECs are shown in Fig. 2.2.

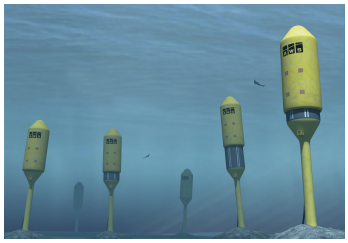

(a) The AWS WEC [7].

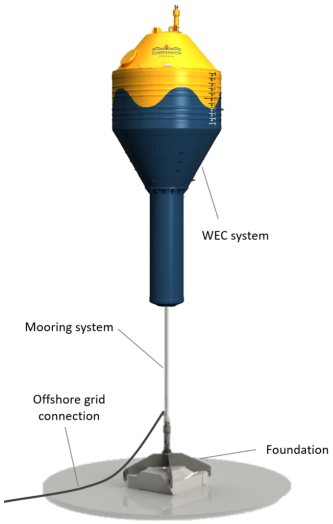

(b) The Corpower WEC [8].

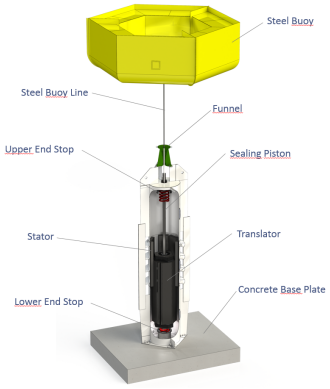

(c) The Seabased WEC [9].

Figure 2.1: Examples of some S-WECs.

(a) The Seapower WEC [12].

(b) The Mocean WEC [13].

Figure 2.2: Examples of some M-WECs.

2.1 The M4 WEC

M4 is a modular hinged raft-type WEC system with multiple floats responding in multi-mode motion. There are essentially bow, mid and stern floats, with adjacent floats connected by beams with hinges above the mid floats. There is one bow float

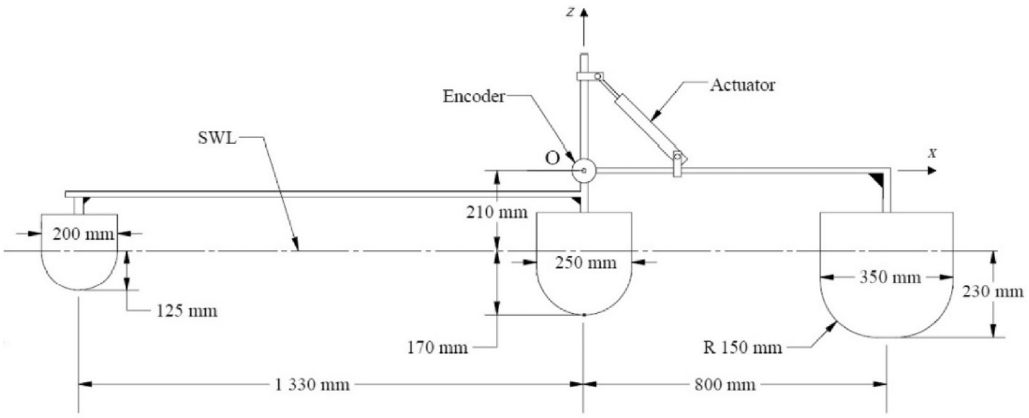

Figure 2.3: Side view of the laboratory scale M4 [15].

and, in its simplest form, one mid and one stern float, of increasing size from bow to stern, so that wave drift forces cause alignment with the wave direction. There is one PTO. Figure 2.3 shows the geometry of the three-float 1-1-1 M4 WEC.

The M4 system can be reconfigured with more mid and stern floats and more hinges, which enable more PTOs, thus greater power capture. Figure 2.4a shows the top views of some of the M4 multi-float configurations. Figure 2.4b shows a 3-D view of the 8- float 1-3-4 M4. In this thesis, we mainly consider the modelling and control problem for the 3-float 1-1-1 M4 WEC. Although increasing the float number leads to a more sophisticated dynamic, due to the consistent design principle among the different configurations, there is no loss of generality.

In the M4 system, power from forcing modes associated with each float combine constructively. There is negligible drag due to the rounded or hemi-spherical bases. The system has been demonstrated to be essentially linear by comparing modelling results with tank testing data [15].

2.2 Existing Control Strategies

Control has been widely applied to increase the power capture of WECs. A review of some existing control strategies are presented is this section.

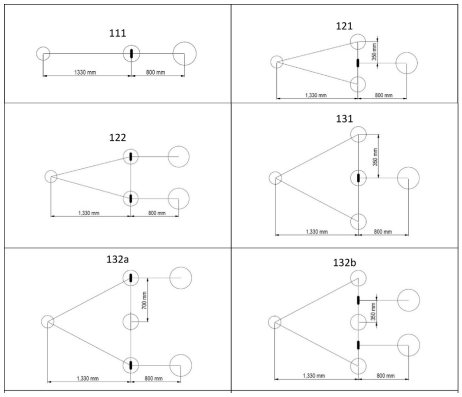

(a) Top view of various configurations of the M4 system.

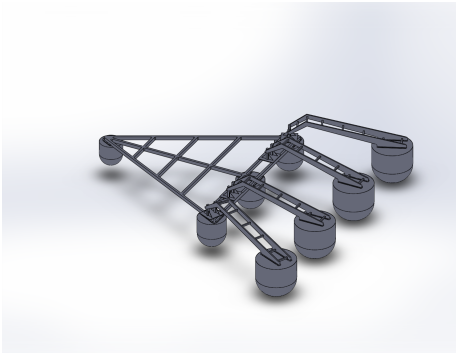

(b) 3-D view of the 8 floats 1-3-4 M4 configuration.

Figure 2.4: Examples of different M4 configurations.

In the 1970s a control method based on the impedance matching principle was developed for regular waves. The method was called reactive control in [16] or complex-conjugate control in [17]. The idea is to adjust the natural frequency of the WEC body to match the wave frequency, so that resonant oscillation and optimum power capture could be achieved. It was tested experimentally on the possibly earliest prototype of WEC, the Salter's Duck [18] in the mid-1970s. Budal and Falnes improved this method and reported that it can also be used in realistic irregular waves provided that the wave spectrum is reasonably narrow [19]. The advantage of this method is it guarantees optimum power absorption in regular incident wave and in irregular incident wave with sufficiently narrow spectrum. On-line optimisation is not required, thus the computational burden is trivial. However, there are two obvious drawbacks: 1)the controller relies on the assumption of a stationary sea state, if the sea state change dramatically the control solution need to be recalculated to match the impedance of the WEC to the new incident wave frequency. 2)operational constraints cannot be handled, there is no protective mechanism to avoid unexpected huge actuation given by the control solution, leading to potential damage of the WEC body. Note that for optimum power absorption forward wave prediction and reactive power is required.

In recent years, Fusco and Ringwood [20] presented a simple controller with two layers: the top-level algorithm is of the same reactive type as discussed above, and it provides the velocity reference to be followed by the low-level velocity tracker. This method, sometimes can be referred as approximated velocity tracking (AVT) control, is applied to a M-WEC called WaveSub recently. Up to 80% mean power improvement has been achieved [21]. By introducing the extra layer velocity tracking controller, several drawbacks of the reactive controller can be overcome. For example, control input constraints can be introduced by either pre-assessing the optimum velocity trajectory or adjusting the control strategy on the low-level velocity tracker. Stability of the control system can be assured by the well-known Linear Quadratic Regulator (LQR) state feedback controller used as the velocity tracker. It will be interesting to see how the controller performs when sea state is varying, which means the optimum velocity trajectory will change rapidly. Also, the computational burden of the AVT method is not investigated in this latest study.

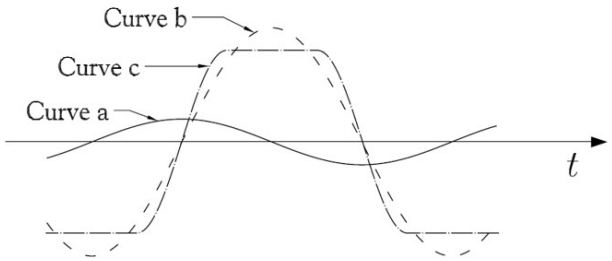

Figure 2.5: The idea of latching control [6].

Another method proposed by Budal and Falnes [22] was named latching control or phase control. Instead of focussing on tuning the device's mechanical parameters to reach resonance, this method aims to keep the body velocity in phase with wave excitation. The idea is to apply a force to lock the motion of the WEC body when its velocity vanishes and to release the body after a certain time period. Fig. 2.5 shows the basic idea of latching control. Curve a can be viewed as the external excitation force exerted on the WEC body. Curve b is the displacement of a WEC body that is at resonance. Curve c shows the displacement of a WEC body with a

non-resonance natural frequency controlled by latching. By restricting the motion of the WEC body for a certain time period, the velocity of the WEC body can be manipulated to be in phase with the excitation force in the rest of the time. The WEC control problem is then transformed into a calculation of the time profile for locking the WEC. Many studies have been proposed to investigate the strategy of latching [23, 24]. Marked power capture improvements are obtained by applying this method, in regular wave three times and in irregular wave two times compared with no control [25, 26]. However, the practical implementation of latching control is later questioned due to the requirement of excessive loads on the latching mechanism [27, 28]. The author thinks the inherent sub-optimality of latching control (only phase but not amplitude optimum condition is met) restrains further research focus onto this WEC control strategy.

Some other trendy control methods are based on optimisation over a specific objective function, e.g. model predictive control (MPC). A suitably designed objective function is vital for these kind of control methods, as it determines the feasibility of the control problem and the neediness of numerical approximation while solving it. In [29], a integral objective function representing the negative of absorbed energy is chosen with an interior penalty term to handle state constraint. The resulting optimal control problem is not convex, preventing the usage of the well-developed quadratic programming algorithm. The author approximates the control problem and resolved it using dynamic programming. Although massive improvement of the energy output can be seen, it is reported by the author that the computational burden will increased exponentially as the model order increases, which is not ideal for M-WEC with complicated dynamics. In [30], the same integral objective function is chosen but with two extra quadratic weighted term to penalize the control input and system state. It is reported by the author that, with this objective function, convexity of the control problem can be guaranteed, which means the control problem can be solved efficiently by the well-developed quadratic programming algorithm. The benefit is that the optimisation process can not only take care of maximising the power capture, but it can also handle operational constraints explicitly. Note that

these methods often require the WEC model to be written in state-space form. The performance relies heavily on model fidelity, especially when the control problem involves higher DOFs. Also, as already mentioned above, real-time optimisation can be computationally demanding and require high performance microprocessor in real-time control implementation. The improvement of absorbed energy provided by on-line optimisation should be great enough to worth the cost. Unfortunately these are rarely assessed in literatures probably due to lack of experimental data from real-time. Some of the other relative studies are shown in [31, 32, 33, 34, 29, 30].

It is also important to point out that most of the control strategies mentioned above focus on S-WECs. It is questionable if these controllers cope with the increased complexity of M-WECs. For example, for latching control, determining the locking time profile and implementing a multiple DOFs latching mechanism into the M-WEC would be challenging. This issue is briefly addressed by [27, 35] on an M-WEC of point absorber type and studied very recently on a raft-type M-WEC by [36].

As almost all the control methods proposed are based on linear wave assumptions, the issue of non-linear effects in WEC dynamics are also worthy of attention. Since control generally increases response to improve power capture, the importance of non-linear effects increases, as discussed for example in [37]. However, including fully non-linear effects can be excessively computationally demanding [38].

In rough conclusion, all the proposed control methods have their own advantages in resolving control problems for specific S-WEC system. However, when it comes to M-WEC system with multi-DOF and high model orders (usually more than a hundred), these control methods are not ideal. A new control strategy needs to be developed to tackle the M-WEC control problem. This strategy should at least has the below features: 1)guarantee optimum or near-optimum energy output. Theoretically this requires forward wave information to be incorporated, which means the designed controller need to interact with wave prediction constructively; 2)has tractable computational burden, preferably an off-line optimisation controller, as

the high model order of M-WEC will inevitably increase the computational load on on-line optimisation process; 3)can handle harsh or soft constraints in WEC operation, if not, it should prove its robustness when constraints (e.g. actuation torque limit) are active. A control-oriented model that can maintain high fidelity of the M-WEC dynamic while suitable for designing controller that meets the aforementioned requirements is preliminarily needed. These can all be viewed as the main research objective in this thesis.

In the following chapters, a generic linear non-causal optimal control framework is proposed for the introduced M-WEC M4. It is essentially a reactive type of controller derived in a time-domain and discrete-time manner. A quadratic cost function is introduced and solved using dynamic programming. The stabilizable feature of the control-oriented enables the control policy to be obtained off-line, so that the resultant control law does not require on-line optimisation, which means the computational load is trivial. The quadratic cost function taken from [30] not only assures feasibility of the control solution, but also introduces two tunable control parameter Q and r (see Chapter 4) to handle soft operational constraints. The control framework can cope with sea wave prediction and utilize these non-causal information to achieve optimum power conversion. The details of this framework are presented in Chapter 4 and 5 after the control-oriented model for the M4 WEC being introduced in Chapter 3.

Chapter 3

Control-oriented modelling for the raft-type M-WEC: M4

In order to describe the WEC control problem in a mathematical way, the WEC dynamic model needs to be presented. In this chapter, an energy-based Lagrangian method is used to derived the motion equation for the M-WEC M4, using the simplest 1-1-1 format as an example. Then, the hydrodynamic is analysed using the linear wave forces theory. The final control-oriented model for the M4 WEC is presented in state-space equations form. Although only the 1-1-1 format of the M4 WEC is modelled, this modelling method can also be used for other formats of the M4 WEC as well as other raft-type M-WECs.

Some useful notations for this chapter are shown in Table 3.1.

3.0.1 M4 dynamic modelling

An energy-based Lagrangian modelling method is presented in [39] for a two-raft-type wave energy converter. This method is adopted and extended for the time domain dynamic modelling of the 1-1-1 type M4 with 3 floats. In this section the motion equation is deduced and the process to derive the final state-space model is demonstrated.

The six DOFs surge, sway, heave, roll, pitch and yaw of a float are denoted as

Table 3.1: Chapter 3 Notation List

Symbol	Description
i	index of each part
r_i	radius of float i
x_i	surge motion of i
z_i	heave motion of i
x_0	surge motion of hinge O
z_0	heave motion of hinge O
θ_1	pitch of i which are on the left of the hinge O
θ_2	pitch of i which are on the right of the hinge O
h_i	horizontal distance from COG of i to hinge O
v_i	vertical distance from COG of i to hinge O
m_i	mass of i, including ballast if it's a float
I_i	inertia of i relative to its own COG
ρ	water density
g	gravitational constant

mode from 1 to 6, respectively. The device is moored from the bow float and it aligns naturally with the wave direction. Roll motion of the device is prevented by outrigger buoys added to the bow float (see Fig. 3.1). Then for simplicity and consistency, the concern will be only motion in x-o-z plane. Therefore, the linear wave forces are also considered only in mode 1, 3 and 5.

The Euler-Lagrangian equation is used to derive the motion equation for this multi-float device with displacement and rotation about the hinge point. First, the generalized coordinate is chosen as $q = [x_0\, z_0\, \theta_1\, \theta_2]^T$. This generalized coordinate

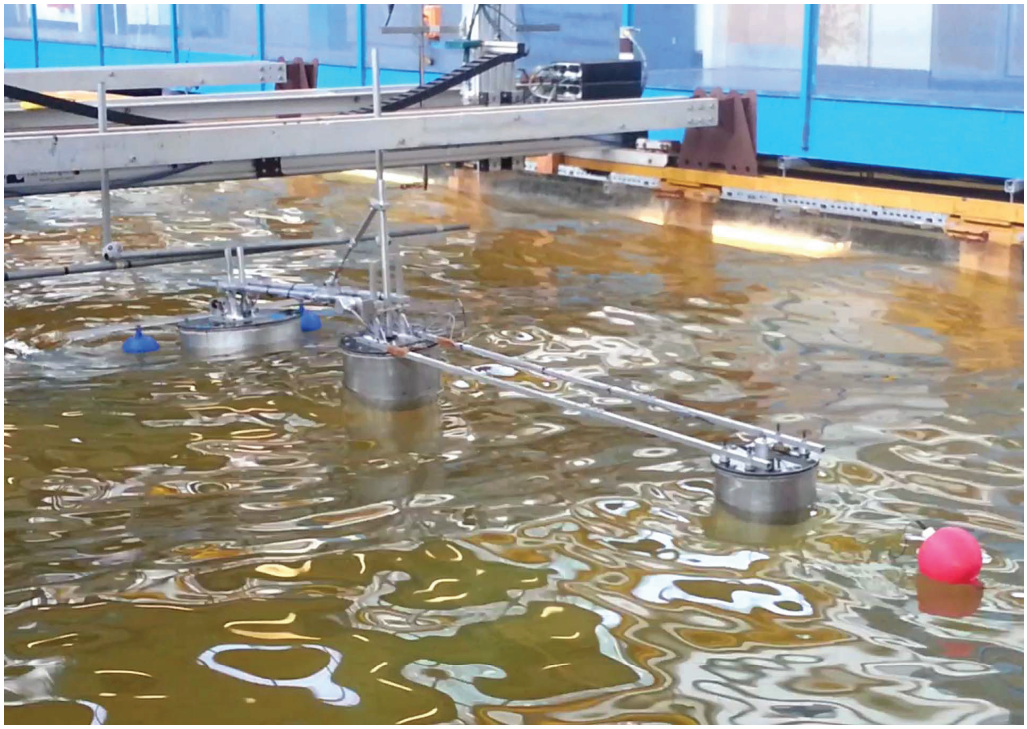

Figure 3.1: Tank experiment of M4 in Manchester [15].

is proven to be independent, complete and holonomic to describe the plane motion of the system. Then for each part of the device, the surge and heave motion can be expressed by the generalized coordinate, as shown in (3.1). Since θ is small, approximations $\sin\theta \approx \theta$ is used in the following coordinate transformation:

$$\begin{aligned}
x_1 &= x_0 - v_1\theta_1, \quad z_1 = z_0 + h_1\theta_1 \\
x_2 &= x_0 - v_2\theta_1, \quad z_2 = z_0 + h_2\theta_1 \\
x_3 &= x_0 - v_3\theta_2, \quad z_3 = z_0 - h_3\theta_2 \\
x_4 &= x_0 - v_4\theta_1, \quad z_4 = z_0 + h_4\theta_1 \\
x_5 &= x_0 - v_5\theta_2, \quad z_5 = z_0 - h_5\theta_2 \\
x_6 &= x_0 - v_6\theta_2, \quad z_6 = z_0 - h_6\theta_2
\end{aligned} \tag{3.1}$$

The dynamics of the M4 device can be expressed by a generic Euler-Lagrangian equation

$$\frac{\mathrm{d}}{\mathrm{d}t}\left(\frac{\partial L}{\partial \dot{q}}\right) - \frac{\partial L}{\partial q} = Q \tag{3.2}$$

$$M = \begin{bmatrix} \sum_{i=1}^{6} m_i & 0 & -m_1v_1-m_2v_2-m_4v_4 & -m_3v_3-m_5v_5-m_6v_6 \\ 0 & \sum_{i=1}^{6} m_i & m_1h_1+m_2h_2+m_4h_4 & -m_3h_3-m_5h_5-m_6h_6 \\ -m_1v_1-m_2v_2-m_4v_4 & m_1h_1+m_2h_2+m_4h_4 & \sum_{i=1,2,4}(I_i+m_i(h_i^2+v_i^2)) & 0 \\ -m_3v_3-m_5v_5-m_6v_6 & -m_3h_3-m_5h_5-m_6h_6 & 0 & \sum_{i=3,5,6}(I_i+m_i(h_i^2+v_i^2)) \end{bmatrix} \tag{3.7}$$

where the Lagrangian $L := T - V$, with T as the total kinetic energy

$$\begin{aligned} T = &\sum_{i=1,2,4} \left[\frac{1}{2} m_i(\dot{x}_i^2 + \dot{z}_i^2) + \frac{1}{2} I_i \dot{\theta}_1^2\right] \\ &+ \sum_{i=3,5,6} \left[\frac{1}{2} m_i(\dot{x}_i^2 + \dot{z}_i^2) + \frac{1}{2} I_i \dot{\theta}_2^2\right] \end{aligned} \tag{3.3}$$

and V is the total potential energy:

$$V = \sum_{i=1}^{6} m_i g z_i \tag{3.4}$$

Q is the generalized force acting on the system, and represents the virtual work done by all non-conservative forces when the system is displaced by an infinitesimal value of the generalized coordinate:

$$Q = f_{b,q} + f_{w,q} + f_{moor,q} + f_{drag,q} + f_{pto,q} \tag{3.5}$$

where $f_{b,q}$ denotes buoyancy force, $f_{w,q}$ denotes linear wave forces, and $f_{pto,q}$ denotes PTO unit moment. $f_{moor,q}$ denotes the mooring force which has a negligible influence on the energy conversion, and is neglected here. $f_{drag,q}$ denotes the drag force on the device, which is also negligible for M4 because of its rounded float base design. These are supported by experiment and computational fluid dynamics and drag is reduced further at full scale [40].

From the Lagrangian equation, we derive

$$M\ddot{q}(t) + C = f_{b,q}(t) + f_{w,q}(t) + f_{pto,q}(t) \tag{3.6}$$

Here M is from the kinetic energy derivative, shown in (3.7). Diagonal terms are summation of mass and inertia with the hinge point O as the reference. Non-diagonal terms account for the coupling dynamics between displacement and rotation. C is

from the potential energy derivative, and is expressed by

$$C = \begin{bmatrix} 0 \\ \sum_{i=1}^{6} m_i \\ m_1 h_1 + m_2 h_2 + m_4 h_4 \\ -m_3 h_3 - m_5 h_5 - m_6 h_6 \end{bmatrix} g \tag{3.8}$$

C indicates the gravity force acting on the system, and it is cancelled by the generalized buoyancy force $f_{b,q}$ at equilibrium [6].

According to linear wave theory, the linear wave force $f_{w,q}$ is composed of the excitation force, radiation damping force and hydrostatic restoring force [41], and is denoted by

$$f_{w,q} = f_{e,q} + f_{rd,q} + f_{rs,q} \tag{3.9}$$

The dynamic equation (3.6) can now be written as,

$$M\ddot{q}(t) = f_{e,q}(t) + f_{rd,q}(t) + f_{rs,q}(t) + f_{pto,q}(t) \tag{3.10}$$

We replace the generalized coordinate index q by i,j to denote the forces or torques acting on float i in j mode, with $j = 1, 3, 5$ denoting surge, heave and pitch mode, respectively. Thus, the generalized linear wave forces can be calculated as (3.11), (3.12), and (3.13). Note that all 'f's are functions of time. Linear wave forces act only on floats. Beams and the PTO unit are above the water surface and have no interaction with waves. In reality, floats can have big heave motion and rise above water surface, especially for the bow and stern float. This will violate the linear assumption in the modelling and introduce non-linearity that is not modelled. However, these effects are not often seen in previous experiment [42]. Without active control response of the floats are not significant and the dynamic of the WEC are reasonably linear. Even with extreme wave height the bow and stern floats will not rise above the water by a huge margin, thanks to the dunking effect of the mid float [42].

$$f_{e,q}(t) = \begin{bmatrix} f_{e,1,1} + f_{e,2,1} + f_{e,3,1} \\ f_{e,1,3} + f_{e,2,3} + f_{e,3,3} \\ f_{e,1,5} + f_{e,2,5} - f_{e,1,1}v_1 - f_{e,2,1}v_2 + f_{e,1,3}h_1 + f_{e,2,3}h_2 \\ f_{e,3,5} - f_{e,3,1}v_3 - f_{e,3,3}h_3 \end{bmatrix} \tag{3.11}$$

$$f_{rd,q}(t) = \begin{bmatrix} f_{rd,1,1} + f_{rd,2,1} + f_{rd,3,1} \\ f_{rd,1,3} + f_{rd,2,3} + f_{rd,3,3} \\ f_{rd,1,5} + f_{rd,2,5} - f_{rd,1,1}v_1 - f_{rd,2,1}v_2 + f_{rd,1,3}h_1 + f_{rd,2,3}h_2 \\ f_{rd,3,5} - f_{rd,3,1}v_3 - f_{rd,3,3}h_3 \end{bmatrix} \tag{3.12}$$

$$f_{rs,q}(t) = \begin{bmatrix} f_{rs,1,1} + f_{rs,2,1} + f_{rs,3,1} \\ f_{rs,1,3} + f_{rs,2,3} + f_{rs,3,3} \\ f_{rs,1,5} + f_{rs,2,5} - f_{rs,1,1}v_1 - f_{rs,2,1}v_2 + f_{rs,1,3}h_1 + f_{rs,2,3}h_2 \\ f_{rs,3,5} - f_{rs,3,1}v_3 - f_{rs,3,3}h_3 \end{bmatrix} \tag{3.13}$$

3.0.2 Hydrodynamic coefficients and linear wave forces

Hydrodynamic coefficients, derived from hydrodynamic software WAMIT, are used to calculate the linear wave forces for each float. WAMIT is a computer program for analyzing floating or submerged bodies based on linear and second-order potential theory [43] The coefficients include excitation force amplitude F_{ex}, excitation force phase ϕ, infinity added mass matrix A_{inf} and radiation damping coefficient $B_{mn}(\omega)$. These forces are calculated as follows:

Wave excitation force

Wave excitation force is independent of the system, and it is treated as a disturbance input to the control system. We use the JONSWAP (Joint North Sea Wave Project) wave model to generate irregular wave spectrum with a frequency intervals 200, which is the same as the wave profile used in [15]. Thus, F_{ex} and ϕ are matrices of size 200×18 (here $18 = 3$ floats $\times$ 6 DOFs). The excitation force for float i in mode

j is

$$f_{e,i,j} = \sum_{n=1}^{200} H(\omega_n) F_{ex}(n, 6(i-1)+j) \cos(\phi(n, 6(i-1)+j) + \phi(\omega_n)) \tag{3.14}$$

where $H(\omega_n)$ and $\phi(\omega_n)$ are the amplitude and random phase of JONSWAP wave spectrum, of size 200×1. Substituting all the 'f' terms in (3.11) by the expression of (3.14) yields the final generalized excitation force, which is a 4×1 vector.

Radiation damping force

Radiation damping force can be expressed by Cummins equation which is a convolution of impulse response function (IRF) and the first derivative of a motion. The IRF L_{mn} is calculated by the radiation damping matrix B_{mn} for m, $n = 1 \ldots 18$,

$$L_{mn}(t) = \frac{2}{\pi} \int_0^\infty B_{mn}(\omega) \cos(\omega t) d\omega \tag{3.15}$$

Thus the radiation damping force for float i in mode j in time domain can be calculated as,

$$\begin{aligned} f_{rd,i,j} = & \sum_{n=1}^{3} \dot{x}_n * L_{6(i-1)+j,6(n-1)+1}(t) \\ & + \sum_{n=1}^{3} \dot{z}_n * L_{6(i-1)+j,6(n-1)+3}(t) \\ & + \sum_{n=1}^{2} \dot{\theta}_1 * L_{6(i-1)+j,6(n-1)+5}(t) \\ & + \dot{\theta}_2 * L_{6(i-1)+j,6(n-1)+5|_{n=3}}(t) \end{aligned} \tag{3.16}$$

Here the summation index n refers to each float. Notation '$*$' denotes convolution with upper and lower limits for integration as t and $-\infty$. For example, the portion of radiation damping force acting on float 1 in surge direction caused by the heave motion of float 2 is,

$$f(t) = \int_{-\infty}^{t} L_{1,9}(t-\tau) \dot{z}_2(\tau) d\tau \tag{3.17}$$

The lower limit can be set to $t - 4T_p$ with sufficient accuracy [15], where T_p is the wave peak period.

Convolution calculation is time-consuming, and there are 81 convolutions in total to be calculated according to the above analysis. Substituting all 'f's in (3.12) with (3.16), applying the linear property of convolution and introducing the motions of each float into the generalized variable by (3.1), we can write the generalized radiation force in a matrix form

$$f_{rd,q}(t) = \int_{t-4T_p}^{t} F_{rd}(t-\tau)\dot{q}(\tau)d\tau \tag{3.18}$$

where F_{rd} is a 4×4 matrix with an IRF of length $4T_p$ in each entry. $\dot{q}$ is first derivative of the generalized coordinate vector. Now the number of convolutions need to be calculated is reduced to 16.

A state-space model can be derived from each convolution term, as shown in [44]. The Hankel singular value decomposition algorithm is used to convert each convolution term to a state-space model. The order of the model is proportional to the length of the IRF $F_{rd,mn}$ and can be very high; in this case study, it is around 400. Then assembling the 16 converted state-space models into one state-space model with with an order of around 6400×6400, which is too high for model-based control algorithms. Thus, model order reduction is necessary for reducing each state-space model. The truncated balanced reduction method [45] is employed to reduce the originally converted state-space model with an order of around 400 to a model with an order of 3 to 8. System identification and truncated balanced reduction method are implemented using MATLAB routines $imp2ss()$ and $balmr()$, respectively. A generic way to decide the order of the reduced radiation model is by performing a convergence check. This can be done by repeatedly simulate the final state-space model with increasing radiation order using the same input wave profile. The average absorbed power should converge to a fixed value as the radiation order increases, meaning the lose of model fidelity caused by model order reduction is minimized. In this specific case, the average power converges at order 20 and order 8 for each subsystem is chosen for the final state-space model with acceptable accuracy.

Now the generalized radiation damping force can be expressed as,

$$\begin{aligned} \dot{z}_s &= A_s z_s + B_s \dot{q}(t) \\ f_{rd,q}(t) &= C_s z_s + D_s \dot{q}(t) \end{aligned} \tag{3.19}$$

where $\dot{z}_s$ is the state variable of the identified and assembled system with an order of 128 and has no physical meaning. $A_s,\ B_s,\ C_s,\ D_s$ are the state-space representation matrixes. Their sizes are 128×128, 128×4, 4×128, 4×4, respectively.

The added mass matrix A_{inf} when the frequency approaches infinity is of size 18×18, with only a constant value in each entry. The added mass term can be viewed as a force relative to second derivative of the generalized variable, $\ddot{q}(t)$. It can also be added to the matrix M, after reassembled to a 4×4 matrix m_∞ following the same way of radiation damping force in (3.12), which is adopted here.

Hydrostatic restoring force

Hydrostatic restoring force is dependent on the heave displacement and pitch rotation, but not on surge, i.e. $f_{rs,i,1} = 0$. The heave restoring force for float i is $f_{rs,i,3} = -\rho g \pi r_i^2 z_i$, and the pitch restoring torque for float i is $f_{rs,i,5} = -\rho g \pi \frac{r_i^4}{4} \theta_{1or2}$. From (3.13), the generalized hydrostatic restoring force can be written in a matrix form

$$f_{rs,q}(t) = Kq(t) \tag{3.20}$$

where K is the 4×4 hydrostatic restoring force matrix,

$$K = \begin{bmatrix} 0 & 0 & 0 & 0 \\ 0 & \sum_{i=1}^{3} k_{zi} & k_{z1}h_1 + k_{z2}h_2 & -k_{z3}h_3 \\ 0 & k_{z1}h_1 + k_{z2}h_2 & \sum_{i=1}^{2} k_{ri} + k_{zi}h_i^2 & 0 \\ 0 & -k_{z3}h_3 & 0 & k_{r3} + k_{z3}h_3^2 \end{bmatrix} \tag{3.21}$$

$k_{zi} = -\rho g \pi r_i^2$, $k_{ri} = -\rho g \pi \frac{r_i^4}{4}$ are respectively the restoring coefficients for heave force and pitch moment of float i.

To sum up, the motion equation for M4 can be written as,

$$\begin{aligned}(M + m_\infty)\ddot{q}(t) + f_{rd,q}(t) + Kq(t) &= f_{e,q}(t) + f_{pto,q}(t) \\ \dot{z}_s &= A_s z_s + B_s \dot{q}(t) \\ f_{rd,q}(t) &= C_s z_s + D_s \dot{q}(t)\end{aligned} \tag{3.22}$$

Modelling the PTO

The PTO moment M_{mech} is modelled as $M_{mech} = -B_{mech}\dot{\theta}_r$, where B_{mech} is a constant coefficient and $\dot{\theta}_r := \dot{\theta}_1 - \dot{\theta}_2$ is the relative pitch rotation velocity. However, the generalized PTO force can be viewed as a manipulable control input to the whole system at the controller design stage and takes the form of

$$f_{pto,q}(t) = \begin{bmatrix} 0 \\ 0 \\ -M_{mech}(t) \\ M_{mech}(t) \end{bmatrix} \tag{3.23}$$

By defining a new state vector $x := [q,\ \dot{q},\ z_s]^T$, the final state-space representation of the M4 control-oriented model can be written as

$$\begin{aligned}\dot{x} &= Ax + B_w f_{e,q}(t) + B_u f_{pto,q}(t) \\ y &= Cx + Du\end{aligned} \tag{3.24}$$

where the system matrices are

$$A = \begin{bmatrix} 0_{4\times4} & I_{4\times4} & 0_{4\times n} \\ -(M+m_\infty)^{-1}K & -(M+m_\infty)^{-1}D_s & -(M+m_\infty)^{-1}C_s \\ 0_{n\times4} & B_s & A_s \end{bmatrix}$$

$$B_w = \begin{bmatrix} 0_{4\times4} \\ (M+m_\infty)^{-1} \\ 0_{n\times4} \end{bmatrix}$$

$$B_u = \begin{bmatrix} 0_{4\times1} \\ (M+m_\infty)^{-1}[0,0,1,-1]^\top \\ 0_{n\times1} \end{bmatrix}$$

$$C = \begin{bmatrix} I_{8\times8} & 0_{n\times8} \end{bmatrix}$$

$$D = \begin{bmatrix} 0_{8\times8} \end{bmatrix}$$

with $A \in \mathbb{R}^{136\times136}$.

This multi-input-multi-output state-space model has 4 inputs including the wave excitation the manipulable PTO control inputs and 8 outputs which are the generalized motion and its velocity.

3.0.3 Validation by numerical simulations

In order to validate the fidelity of the control-oriented model for the M4 WEC, numerical simulations are run.

Radiation subsystems

It has been discussed in the previous sections that the radiation forces calculated by convolutions are replaced by state-space subsystems through system identification and model order reduction methods. Here, the IRF and bode diagram of the identified subsystems with different orders are compared, with the original convolution kernel F_{rd} as a benchmark. Note that only mode $1,1$ and $3,3$ in the kernel F_{rd} are investigated as an example. Fig. 3.2 and Fig. 3.3 show these results.

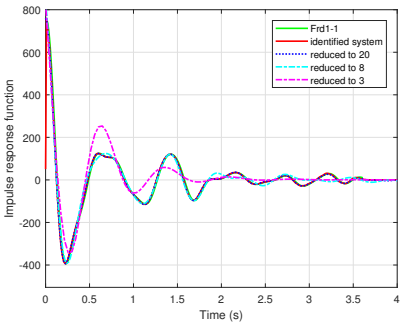

(a) Impulse response function of subsystems for $F_{rd,1,1}$.

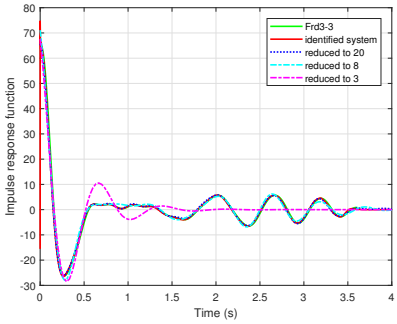

(b) Impulse response function of subsystems for $F_{rd,3,3}$.

Figure 3.2: Validation of subsystems fidelity using impulse response function.

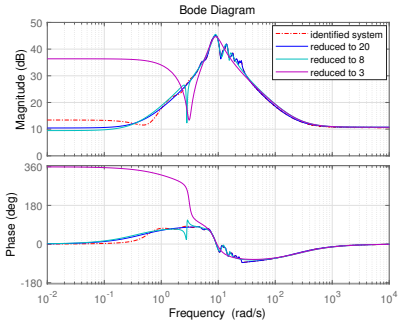

(a) Bode diagram of subsystems for $F_{rd,1,1}$.

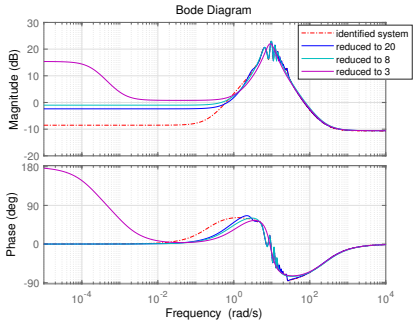

(b) Bode diagram of subsystems for $F_{rd,3,3}$.

Figure 3.3: Validation of subsystems fidelity using bode diagram.

It can be observed that, a subsystem with order reduced to 20 (from hundreds) preserve the radiation dynamics relatively well, compared with the IRFs of the identified system. If the order is reduced to 8, the IRF perturbation is still acceptable. However, if the order is reduced to 3, significant perturbation can be observed from the IRF, which means the error caused by model order reduction is relatively huge. The same result can be noticed from the bode diagram plot as well. For the subsystem of order 3, the perturbation of both magnitude and phase response are huge for lower frequency range. Based on these analysis, a subsystem of order 8 can be picked for the radiation in mode $(1, 1)$ and $(3, 3)$. The same comparison has to be

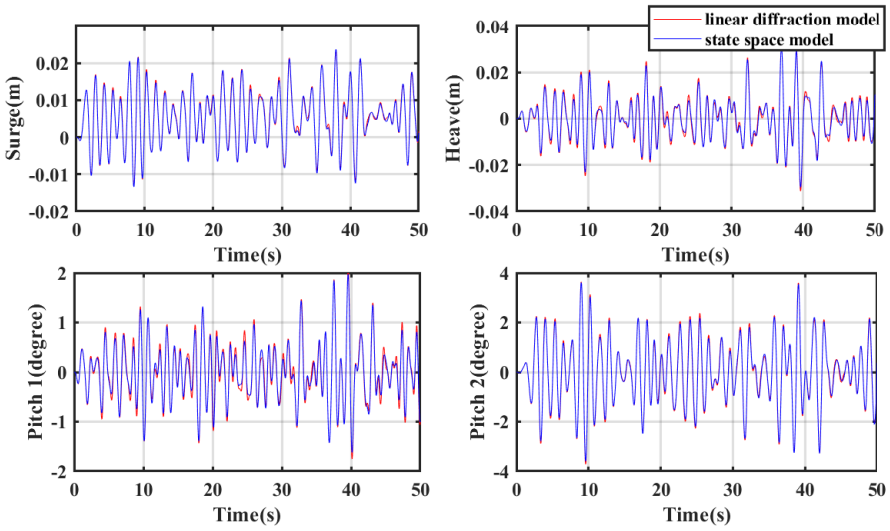

Figure 3.4: Time responses comparison between the state-space model and linear diffraction model of the M4 WEC.

made for all of the 16 modes of the convolution kernel F_{rd}. Note that reducing the number of concerned DOFs from 18 to 4 clearly ease the efforts to be made here, as otherwise there will be 324 modes to be analysed.

Model fidelity

In order to further validate the fidelity of the final control-oriented model, the model responses with JONSWAP irregular wave profile as an input are presented and shown in Fig. 3.4. Note that for this specific simulation, the sea condition is chosen as significant wave height $H_s = 0.04m$ and peak period $T_p = 1.8s$.

Here, comparison is made between the state-space model and the linear diffraction model used in [15] where comparisons are made with experimental data. The differences between the state-space model and the linear diffraction model exist because in the linear diffraction model the radiation effects are calculated via convolutions based on Cummin's method.

It can be observed from Fig. 3.4 that the responses in all the considered DOFs are almost identical for both of these time domain model. In other words, there is negligible model error brought in by approximating the radiation force and reducing

the order of the subsystems.

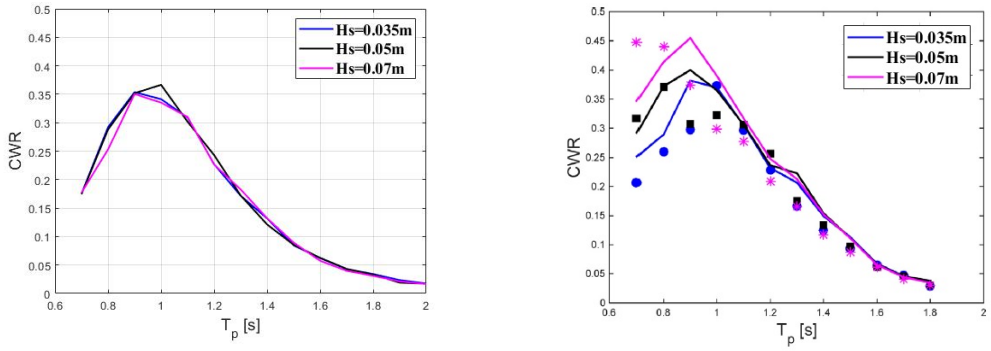

(a) capture width ratio from state-space model

(b) capture width ratio from tank experiment [15].

Figure 3.5: CWR comparisons between the state-space model, linear diffraction model and experimental results.

Fig. 3.5 validates the control-oriented state-space model against the experimental data from [15]. Here the performance index capture width ratio (CWR) is utilized to show results in various sea conditions. CWR is defined as the captured power P_{av} divided by the wave power per meter wave crest P_w again divided by the wavelength L_e associated with the energy period T_e. This definition will be used across this thesis and the benefit of using this definition is that the performance of WEC can be compared with theoretical limits shown in [6].

Fig. 3.5b shows the CWR from experimental data (dotted plot) as well as the CWR from the linear diffraction model (solid linear plot). In comparison, the CWR from the state-space model are shown in Fig. 3.5a. Note that simulations are run in Matlab for T_p ranges from $0.7s$ to $1.8s$ with $0.1s$ interval. H_s are selected to be $0.035m$, $0.05m$ and $0.07m$, to be consistent with the experimental data. Theoretically speaking, the CWR curves should be independent of H_s for constant passive damping ratio B_{mech}. Fig. 3.5a shows that the state-space model has good fidelity in this regard. The CWR for the linear diffraction model does not collapse because different damp ratio is used for simulation to match with experiment results. In terms of the model fidelity, the CWR from the state-space model have good agreement

with the experimental results for most of the sea conditions except for higher wave height ($H_s = 0.7s$) in low frequencies ($T_p = 0.7s, 0.8s$). A reason for this maybe the ignored non-linear effects occur when responses are huge. Overall, the state-space model works well and this pave the way for developing model-based control strategies for the M4 WEC.

In conclusion, a control-oriented model is presented for the 3-float M-WEC M4. State-space representation is adopted as it serves the purpose for developing model-based advanced control methods. System identification and model order reduction method are used to derive the final state-space model. The model order reduction method is necessary for obtaining a low order state space representation, which can benefit controller design in regard of computational effectiveness. The way of choosing the best model order (a balance point between model fidelity and model order) is briefly discussed. The fidelity of the final control-oriented model is validated against experimental data. These pay the way for designing advance control method for M-WECs.

Chapter 4

The linear non-causal optimal controller

Based on the derived dynamic model presented in the last chapter, the energy-maximizing control problem for M-WECs can be formulated. In this chapter, this optimal control problem for M-WECs is solved in discrete-time using dynamic programming method based on the Bellman optimality principle, taking the introduced 3-float M4 WEC as a case study. Similar to the modelling method discussed in the last chapter, the control method can also be applied to other M-WECs.

4.1 Control policy derivation

Firstly, the control-oriented dynamic model presented in (6.7) is discretized using the Zero-Order Hold (ZOH) method. The discrete-time dynamic model can be written as:

$$\begin{aligned} x_{k+1} &= Ax_k + B_w w_k + B_u u_k \\ z_k &= Cx_k \end{aligned} \tag{4.1}$$

where x_k, u_k represent the states and input of the system, w_k represents the incoming wave excitation force, z_k represents the system output which is defined as the hinge

velocity of the M4 WEC.

Therefore, the absorbed instant power can be written as: $P_k = -z_k u_k$. The energy-maximizing control problem can then be formulated as:

$$\min_{u_0,\ldots,u_N} \Sigma_{k=0}^{N} \left\{ z_k u_k + \frac{1}{2} x_k^T Q x_k + \frac{1}{2} R u_k^2 \right\} \tag{4.2}$$

subject to (4.1).

Here, N is the length of the control horizon. The goal is to find a control sequence $\{u_0, \ldots, u_N\}$ that minimizes the cost function. The cost function consists of three parts: 1) the negative of the instant power $z_k u_k$, minimizing this is equivalent to maximizing the power; 2) $\frac{1}{2} x_k^T Q x_k$ which is used to penalize the system state x_k; 3) $\frac{1}{2} R u_k^2$ which is used to penalize the control input u_k. The reason for including these two penalization terms in the cost function is that at optimality the control policy for energy-maximizing problem is of "bang-bang" type, which means the control input only takes the maximal and minimal possible value. This can cause extremely large response at hinge rotation for the M-WECs, which is not ideal for the operation of these WECs. By adding these soft constraints in the cost function and tuning the weight Q and R for different sea conditions the safe operation of M-WECs can be achieved. Note that operational constraints, e.g. position/velocity limits, control torque limits, etc, are not explicitly dealt with in this controller. Dealing with these constraints has meaningful impact in WEC control problem but will inevitably increase computational burden of the controller. Here I focus on designing a simple controller that can sufficiently improve the power absorption of M4.

This optimization problem is solved here using dynamic programming based on the Bellman's principle of optimality:

An optimal policy has the property that whatever the initial state and initial decisions are, the remaining decisions must constitute an optimal policy with regard to the state resulting from the first decision [46].

Rewrite the cost function in (4.2) as

$$L_k = z_k u_k + \frac{1}{2} x_k^T Q x_k + \frac{1}{2} r u_k^2 \tag{4.3}$$

and define an optimal cost-to-go function as:

$$v(x,k) = \frac{1}{2}x_k^\top V_k x_k + x_k^\top s_k + a_k \tag{4.4}$$

As there is no constraint on the final state x_N, we can also add that:

$$v(x,N) = \frac{1}{2}x_k^\top V_N x_k + x_k^\top s_N + a_N = 0 \tag{4.5}$$

Thus, the boundary conditions are $V_N = 0$, $s_N = 0$ and $a_N = 0$.

According to the Bellman's principle of optimality, the optimality condition for this energy-maximizing control problem is:

$$v(x,k) = \min_{u_k}\{L(x_k,u_k) + v(x,k+1)\} \tag{4.6}$$

In other words, the optimal control input u_k at time k is the u_k that achieves the minimum in (4.6). To solve for u_k, let $\frac{\partial(L(x_k,u_k)+v(x,k+1))}{\partial u_k} = 0$, we can get:

$$\begin{aligned} u_k &= -(R + B_u^\top V_{k+1} B_u)^{-1}[(B_u^\top V_{k+1} A + C)x_k + B_u^\top V_{k+1} B_w w_k + B_u^\top s_{k+1}] \\ &= K_{x,k}x_k + K_{w,k}w_k + K_{s,k}s_{k+1} \end{aligned} \tag{4.7}$$

where

$$K_x = -(R + B_u^\top V_{k+1} B_u)^{-1}(B_u^\top V_{k+1} A + C) \tag{4.8}$$

$$K_w = -(R + B_u^\top V_{k+1} B_u)^{-1} B_u^\top V_{k+1} B_w \tag{4.9}$$

$$K_s = -(R + B_u^\top V_{k+1} B_u)^{-1} B_u^\top \tag{4.10}$$

Obviously, the optimal input u_k has to be determined by working backward in time from the final stage $k = N$. The so called discrete-time Riccati equations (DARE) for backward iterations can be found by substituting (4.7) into (4.6):

$$V_k = Q + A^\top V_{k+1} A - (C + B_u^\top V_{k+1} A)^\top (R + B_u^\top V_{k+1} B_u)^{-1}(C + B_u^\top V_{k+1} A) \tag{4.11}$$

and

$$s_k = (A + B_u K_{x,k})^\top (V_{k+1} B_w w_k + s_{k+1}) \tag{4.12}$$

For infinite horizon optimal control problem, i.e. $N \to \infty$, a steady state solution for the DARE is required. This solution exists when the original dynamic system is

stabilizable and the tuning parameters Q are R are positive definite, in which case the time index k can be dropped for the DARE [47]. With these results, the control policy (4.7) can be further simplified. Define $\Phi = (A + B_u K_x)^\top$, notice that:

$$s_{k+1} = \Phi s_{k+2} + \Phi V B_w w_{k+1} \tag{4.13}$$

$$s_{k+2} = \Phi s_{k+3} + \Phi V B_w w_{k+2} \tag{4.14}$$

$$s_{k+1} = \Phi^2 s_{k+3} + \Phi^2 V B_w w_{k+2} + \Phi V B_w w_{k+1} \tag{4.15}$$

Suppose the wave excitation force sequence are available for n_p steps into the future,

$$s_{k+1} = \Phi^{n_p-1} s_{n_p} + [0, \Phi V B_w, \ldots, \Phi^{n_p-1} V B_w][w_k, w_{k+1}, \ldots, w_{k+n_p-1}]^\top \tag{4.16}$$

Also notice that $K_w = K_s V B_w$, define $\Psi = [V B_w, \Phi V B_w, \ldots, \Phi^{n_p-1} V B_w]$, the control policy (4.7) can be rewritten as:

$$u_k = K_x x_k + K_d w_{k,n_p} \tag{4.17}$$

where $K_d = -(r + B_u^\top V B_u)^{-1} B_u^\top \Psi$ is the control gain and $w_{k,n_p} = [w_k, w_{k+1}, \ldots, w_{k+n_p-1}]^\top$ is the sequence of predicted wave excitation forces.

The resulting control policy is naturally divided into two parts: a feedback part with regard to the system states x_k through a constant gain K_x and a feed-forward part with regard to the future incoming excitation forces through a constant gain K_d. The fact that K_x and K_d can be pre-calculated once the dynamic system is fixed is ideal for real-time implementation of the controller. In the following section, the technique for realizing feedback is discussed. Note that in this chapter, without further notice, the wave prediction sequence w_{k,n_p} is assumed to be perfect, which means no matter how long the prediction horizon n_p is, there is no error in the prediction. Practical wave prediction techniques will be introduced in the next chapter.

Since mooring is not modelled, the state-space model is not stable in surge mode. In order to have a steady state solution from the DARE, a small stiffness term is added to the surge mode of the restoring matrix K mentioned in the last chapter.

This will not affect the power performance of the WEC model but guarantee that a control solution to be obtained. In practice, the eigenvalue of the close loop control system given from matrix $(A - B_u * K_x)$ need to be checked and all the eigenvalues should be located within the unit circle.

4.2 Observer design

In order to realize feedback control the state information x_k is required. However, as discussed in Chapter 2, some of the states in x_k (e.g. the states representing the radiation sub-systems) do not have any physical meaning, which means these information can not be measured with sensors in reality. To get the full knowledge of the state information x_k in real-time, an observer has to be designed. Here a standard Kalman filter is adopted and its structure will be discussed as it is necessary for completing the simulations. Simulation results to demonstrate the efficacy of control are shown in the next section. Note that in the next chapter this observer will be altered to also serve the purpose of short term wave prediction.

This standard Kalman observer has the M4 control input u_k and output y_k from measurement as the observer's inputs and an estimated state information $\hat{x}_k$ as the output. In the simulations it runs at every time step for the state estimation.

We denote the former input of non-causal controller with observer $\hat{u}_{k-1}$, and the estimated state $\hat{x}_{k-1}$. The Kalman observer algorithm runs as follows: firstly, calculate a priori estimation with the former state information

$$\hat{x}_k^- = A\hat{x}_{k-1} + B_u\hat{u}_{k-1} + B_w w_{k-1} \tag{4.18}$$

and then the error covariance P_k^- of this priori estimation is calculated with the predefined model error covariance Q_{kal}

$$P_k^- = AP_{k-1}A^T + Q_{kal} \tag{4.19}$$

The Kalman observer gain is

$$K_{kal} = P_k^- C^T (CP_k^- C^T + R_{kal})^{-1} \tag{4.20}$$

where R_{kal} is the covariance of the measurement. The estimated state information can be calculated as

$$\hat{x}_k = \hat{x}_k^- + K_{kal}(y_k - Cx_k^-) \tag{4.21}$$

The last step in a Kalman algorithm loop is to update the error covariance matrix P_k for the next time step

$$P_k = (I - K_{kal}C)P_k^- \tag{4.22}$$

The non-causal optimal control policy with the states estimated by a Kalman observer can be rewritten as

$$\hat{u}_k = K_x\hat{x}_k + K_d w_{k,np} \tag{4.23}$$

In simulation, the measurement of system output y_k is set to be the state space model output $z_k = y_k = Cx_k$ with added random measurement errors which have a pre-defined error covariance.

4.3 Numerical simulations

Numerical simulations are carried out to demonstrate the efficacy of the proposed LNOC algorithm. Comparisons are made between the designed non-causal optimal controller and a well-tuned passive damper. The passive damper ratio is obtained by trial and error the value that offers most energy output is $B_{mech} = 6$. For each simulation, the JONSWAP wave spectrum with specific significant wave height H_s, peak period T_p and enhancement factor γ is used to generate the irregular wave excitation force profile. At each time step the excitation force w_k is applied to the state equation and the prediction sequence w_{k,n_p} is utilized for the LNOC. Since w_{k,n_p} is pre-calculated in this case it is ideal. The same excitation force profile is used for both passive damper and the LNOC. The sampling rate T_s is set to be dependent on the peak period as $T_s = T_p/200$ so that 200 times steps are run for each peak period regardless of its actual length. Simulation time is set as 700 seconds for calculating the average absorbed power.

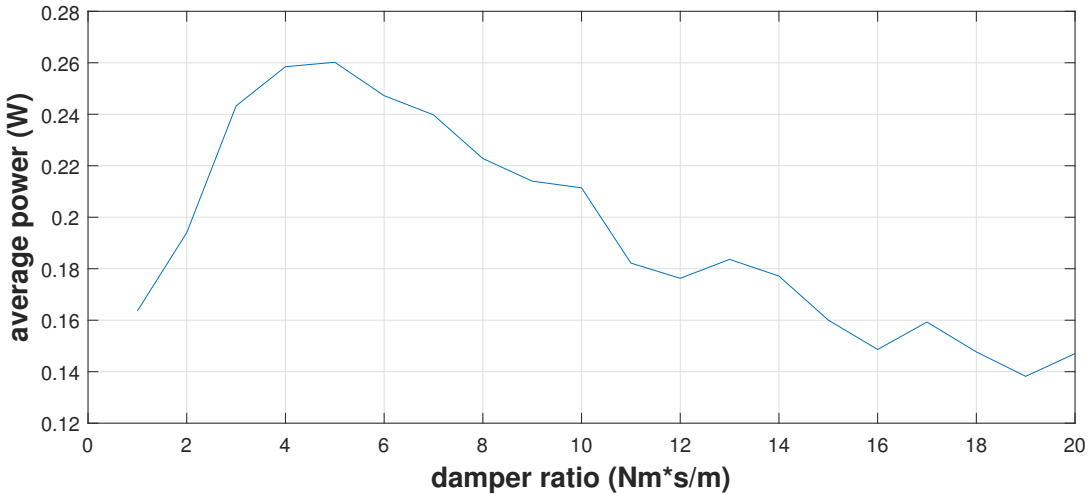

Figure 4.1: Trial and error for tuning the optimal passive damping ratio, specifically for sea state $H_s = 0.04m$, $T_p = 1.0s$.

Here a demonstration of finding the optimal passive damping ratio using trial and error method is shown in Fig. 4.1. For this specific sea state, $H_s = 0.04m$, $T_p = 1.0s$, the damping ratio is varied from 1 to 20 to simulate for average absorbed power. It can be noticed that for this sea state the optimal damping ratio is 5. However, as the WEC is designed to operate in a range of wave periods, the damping ratio need to be tuned to give the best absorbed power across all the wave periods, in this case from $T_p = 0.7s$ to $1.8s$. The overall best fit value of damping ratio is found to be 6. The tuning curve for other sea states are not shown here for the sake of space.

4.3.1 Energy conversion improvement

Firstly, simulation with a JONSWAP wave profile ($H_s = 0.04m, T_p = 1.8s$, $\gamma = 1$) is used to demonstrate the controller performance. Controller is implemented with the pre-tuned parameters Q, R and fixed wave prediction horizon n_p. Energy, power, control input and relative pitch angle of the device are all plotted to give complete observation and comparison.

Fig. 4.2 and Fig. 4.3 show that with the same wave profile ($H_s = 0.04m, T_p = 1.8s$) as in the modelling stage, the non-causal optimal controller with a 3.6 sec-

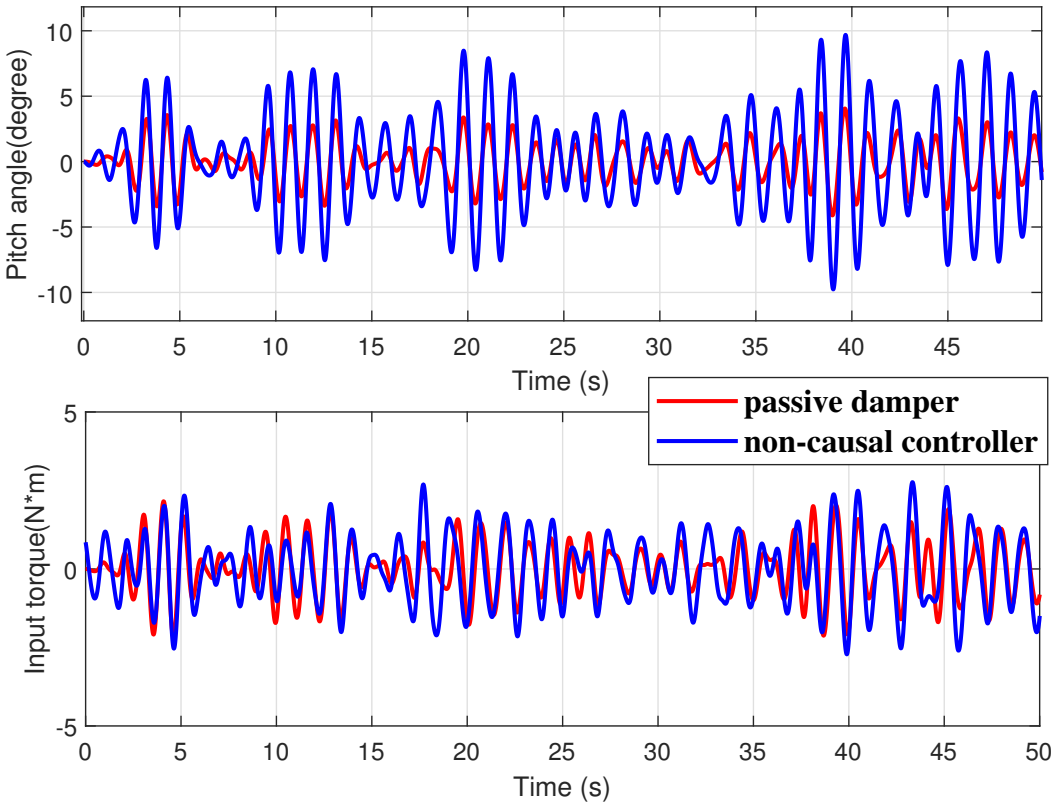

Figure 4.2: Relative pitch and input torque, JONSWAP wave $H_s = 0.04m$, $T_p = 1.8s$, $\gamma = 1$, prediction horizon $2T_p = 3.6s$ ($n_p = 400$).

onds ($2T_p$) forward wave excitation force prediction remarkably improves the energy output by around 80% (at 50 seconds going from $6.06J$ with a well-tuned passive damper to $10.89J$ with the controller). The relative pitch angle also has an increase from 1.54° to 3.74° (RMS value). Note that negative value can be seen in Fig. 4.3 for the non-causal controller. These are reactive power that required to improve the performance of the WEC. A mechanical or electrical design to realize this bi-directional power flow is needed in practice. These are practical aspects that will not be discussed at this stage.

It can be seen from the input torque figure that, the control input from LNOC has phase differences compared to the passive damper who tends to follow the hinge velocity. A good example can be observed from 0 to 5 seconds of the input torque figure: the passive damper input is small due to the absence of any wave peak, while

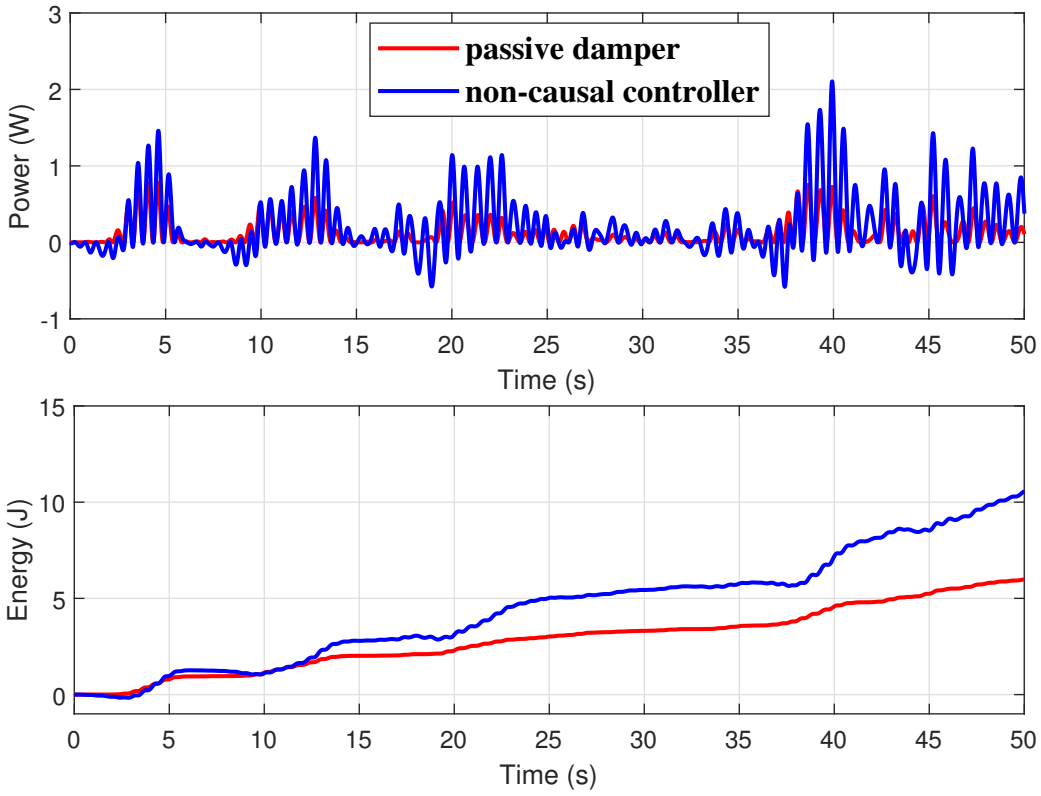

Figure 4.3: Power and energy, JONSWAP wave $H_s = 0.04m$, $T_p = 1.8s$, $\gamma = 1$, prediction horizon $2T_p = 3.6s$ ($n_p = 400$).

the LNOC input is being relatively active thanks to the prevision of the incoming wave peak incorporated by the non-causal controller. The input torque maximum amplitude resulting from the LNOC is however quite similar to the case of a passive damper. This means the non-causal controller does not require a higher demand on the torque limit of the actuator, which is very costly in practice.

Instead of looking at only one sea states, simulations are then run for various sea conditions and the performance index CWR is used to show the control performances. Fig. 4.4 shows the CWR of the device obtained from a wide range of simulations with JONSWAP wave spectrum of $H_s = 0.035m$, $H_s = 0.05m$ and $H_s = 0.07m$. Wave peak periods range from $0.7s$ to $1.8s$ with $0.1s$ interval. Enhancement factor $\gamma = 1$. Results with a passive damper (dashed line) are close to the CWR obtained in a tank experiment [15], validating the modelling fidelity

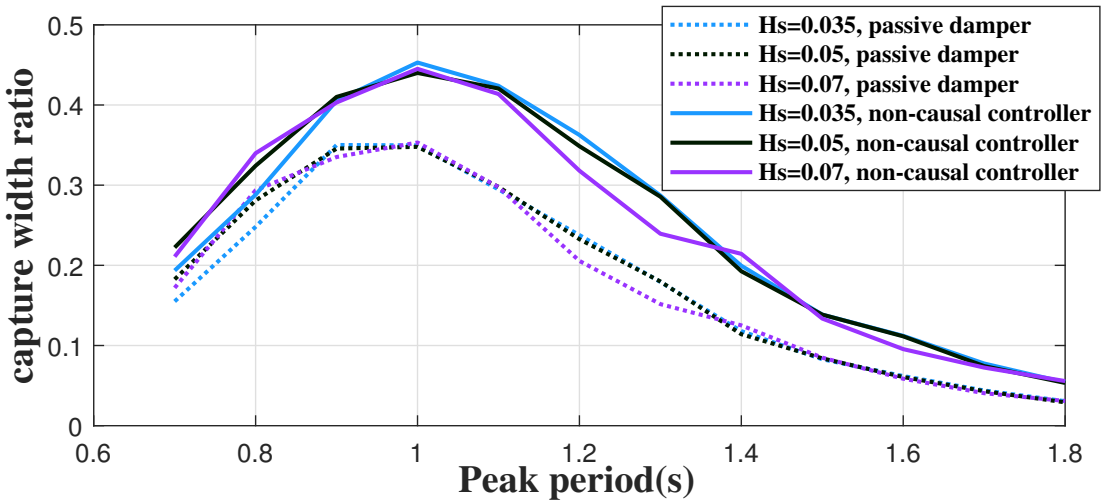

Figure 4.4: Capture width ratio in different wave height and peak period, prediction horizon $5T_p$.

again. With the non-causal controller (solid line), the CWR of the device improves across a wide range of peak periods. Within peak wave periods of 1-1.8 seconds tank scale (6-11 seconds in full scale), the improvement changes from 40% at wave peak period $T_p = 1s$ to 100% at wave peak period $T_p = 1.8s$. Note that the same controller parameters Q and R are used for different wave conditions (significant heights and peak periods). It can also be seen that CWR is almost independent of the significant wave height and is determined by the wave peak periods as expected with this form of non-dimensional CWR.

4.3.2 Non-ideal wave prediction

Secondly, prediction errors are introduced to demonstrate how robust the controller is against wave prediction errors.

Fig. 4.5 shows the energy conversion when wave predictions are subject to errors.Two types of errors to the prediction are introduced as can be seen in the upper sub-plot of Fig. 4.5. The black line shows the case when prediction is contaminated by measurement noise represented by White Gaussian Noise (WGN). For the pink line a sequence of noises with ramped magnitudes are added to prediction to en-

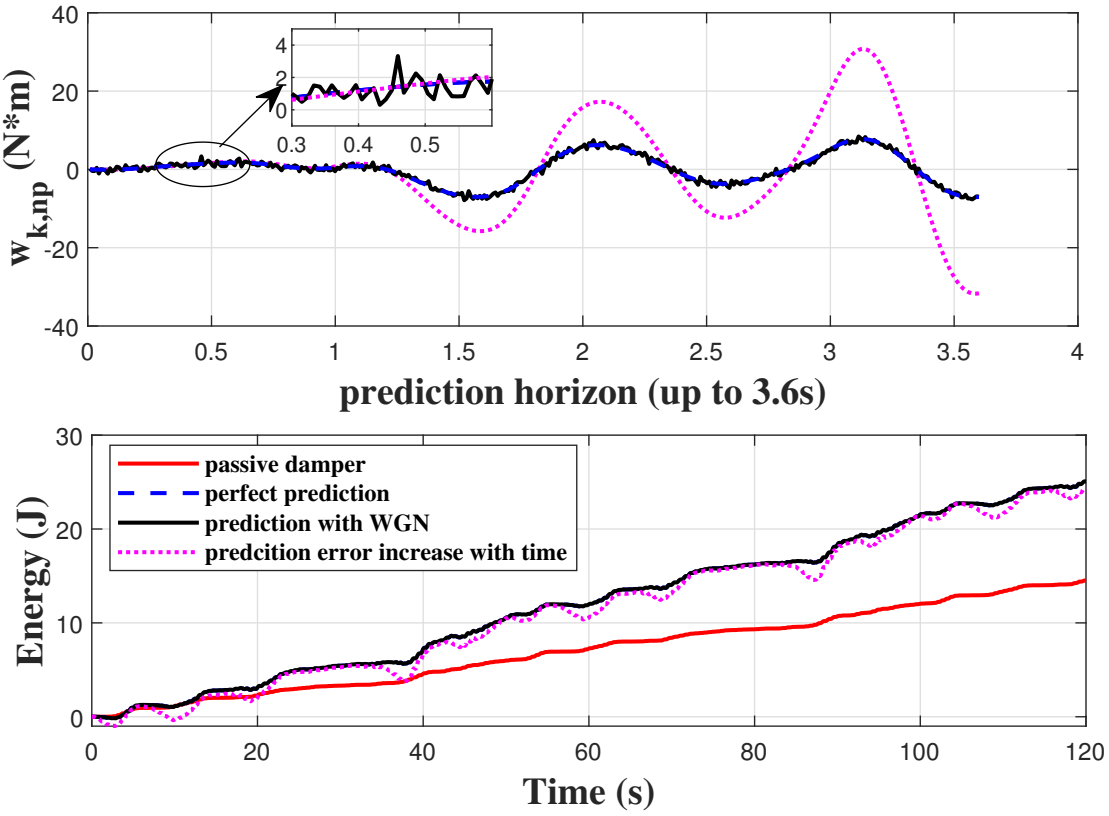

Figure 4.5: Energy conversion with prediction error.

large the prediction error with time. The reason for doing this is that most of the wave prediction techniques can provide better prediction in the near future than for longer times. Energy conversion of both cases can be seen in the bottom sub-plot of Fig. 4.5 and compared to the results of Fig. 4.3. For the WGN case energy conversion is hardly affected. This shows the controller is very robust against this kind of prediction error, which normally occurs with sensors. When the prediction error increases with time, the controller performs slightly worse compared with the WGN case.

4.3.3 The effect of prediction horizon

Thirdly, the length of wave prediction n_p is varied to show how it affects the control performance. This is a rather important issue because the assumption of perfect

wave prediction is unrealistic. Regardless of the techniques adopted for wave prediction, prediction errors exist and generally the prediction error increases with the length of the prediction horizon.

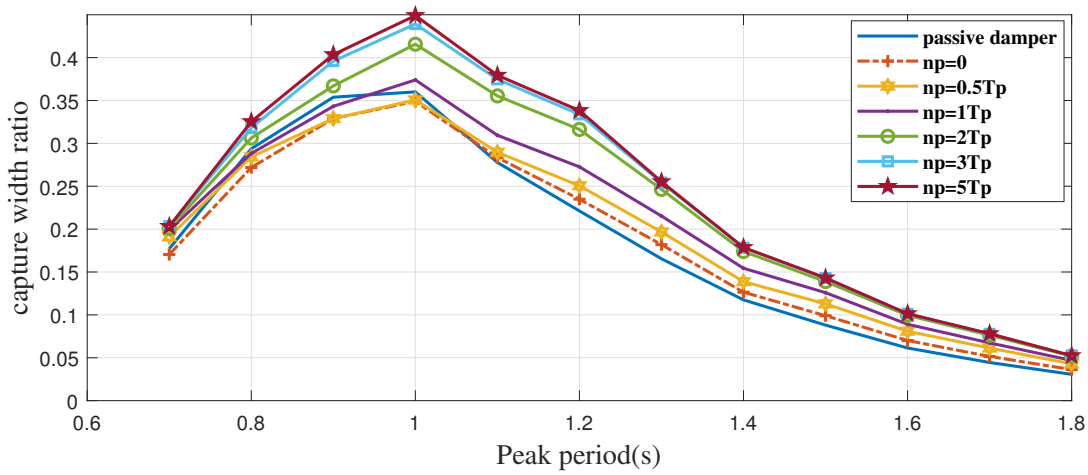

Figure 4.6: Capture width ratio with different length of forward wave prediction n_p

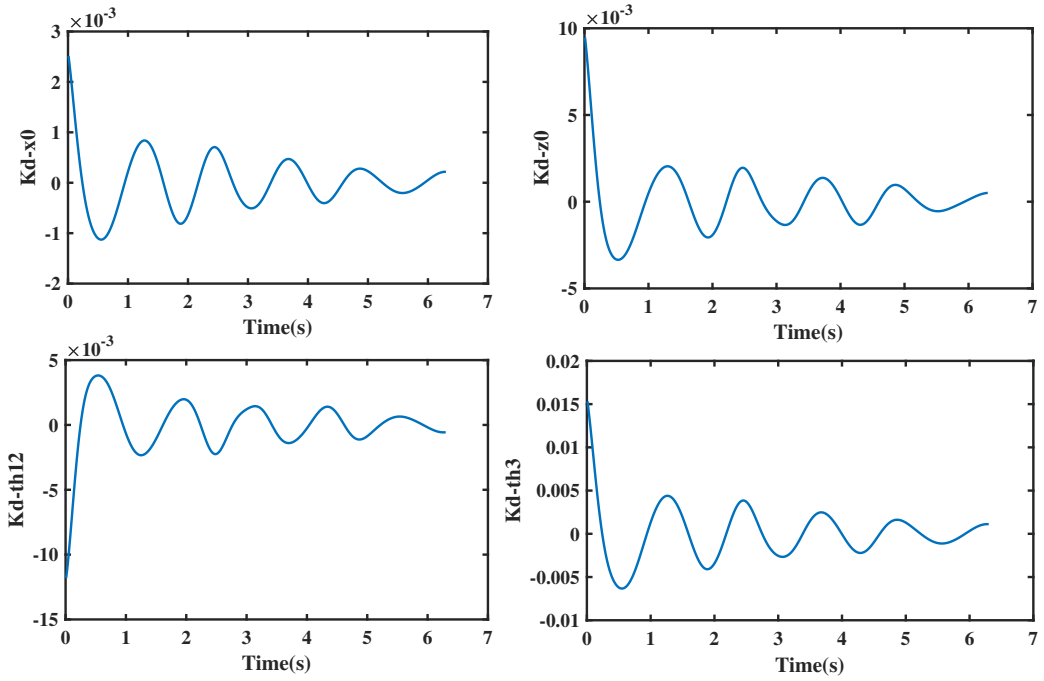

Figure 4.7: Feed forward gain K_d in surge, heave, pitch mode, as prediction horizon proceeds.

Fig. 4.6 shows the non-causal optimal controller's performance with different prediction horizons. The length of prediction is normalised with the peak wave period T_p. CWR plot shows that with a longer prediction horizon n_p, the controller has better performance. With no prediction ($n_p = 0$), the advantage of control is trivial. The controller tries to improve performance by adjusting the stiffness and damping of the WEC model. With n_p increase from $0T_p$ to $2T_p$, the non-causal controller provides more energy output. However, the influence of the prediction horizon starts to decrease as n_p increases to a big enough value. $n_p = 3T_p$ provides almost optimal control performance. Fig. 4.7 provides better observation for the feed-forward gain K_d which decreases to 0 as the prediction horizon prolongs. This explains the conclusion drawn from Fig. 4.6.

4.3.4 Tuning of control parameters Q and r

Figs. 4.8,4.9,4.10 provide more insights on how to tune the controller weighting matrices Q and r. Simulations are run using JONSWAP waves with $H_s = 0.035m$, and a wave prediction horizon of 3.6 seconds ($n_p = 400$). The red line is the CWR of the device with a passive damper for comparison purpose. The states weighting matrix Q is divided into two parts which are tuned separately. The first part is for the first eight states which are the displacement and velocity of the device, denoted by q_1. The second part is for the states without any physical meaning corresponding to the radiation subsystems, denoted by q_2. The structure of Q is in the form of

$$Q = \begin{bmatrix} q_1 I_8 & 0 \\ 0 & q_2 I_n \end{bmatrix} \tag{4.24}$$

with I_n denoting an n by n identity matrix. Control input weighting is denoted by r. Note that tuning of parameter r should be considered together with the control actuator torque limit since a smaller value of r can lead to larger control input magnitude. $r = 0.08$ is chosen for simulations carried out in this paper after the tuning procedure.

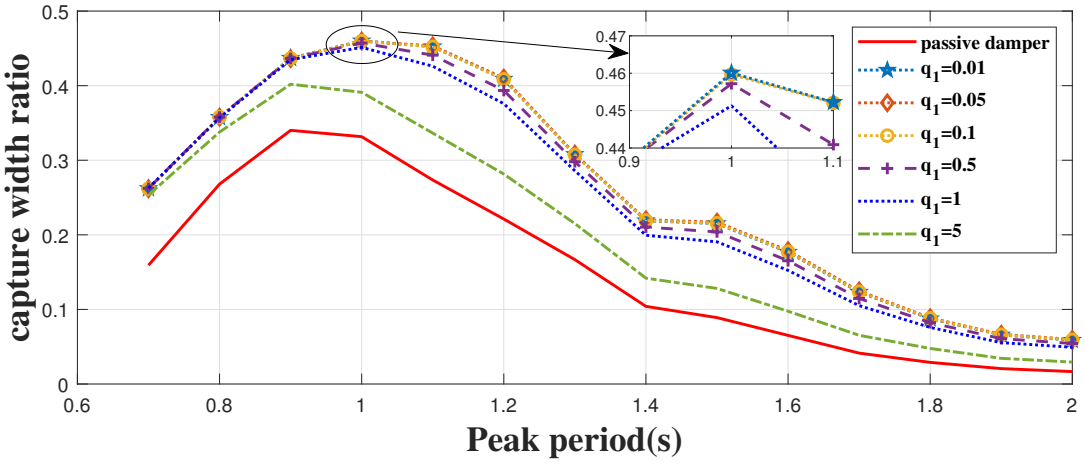

Figure 4.8: Tuning of controller parameter Q, for states with physical meanings.

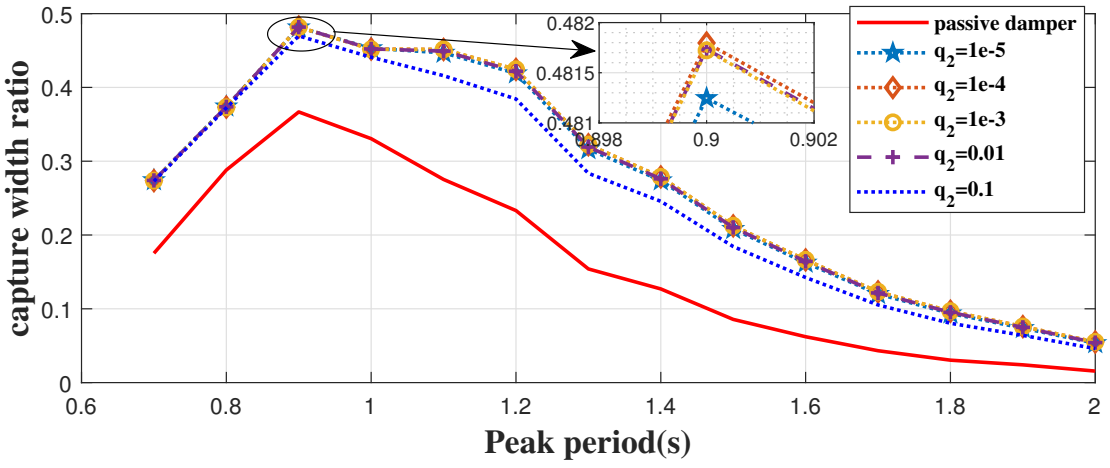

Figure 4.9: Tuning of controller parameter Q, for states without physical meanings.

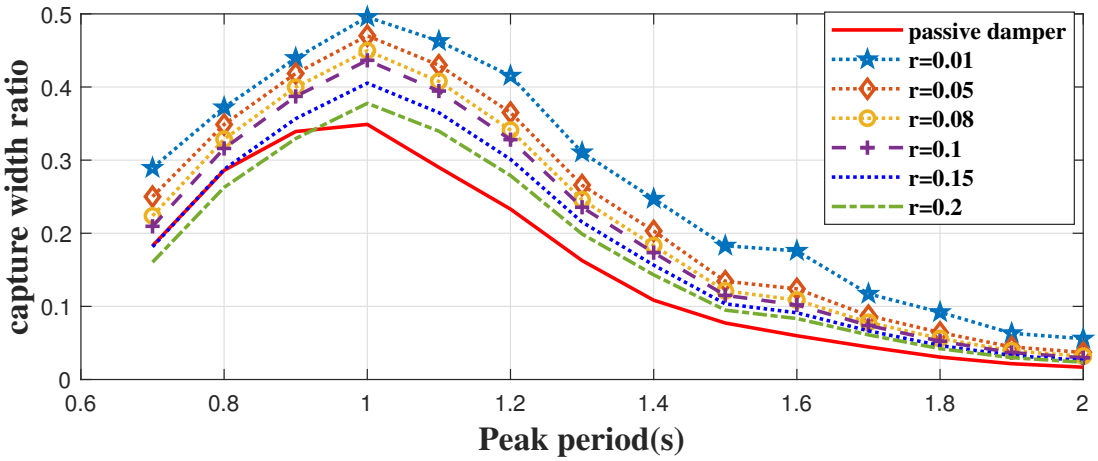

Figure 4.10: Tuning of controller parameter r.

Chapter 5

Short-term sea wave prediction using an autoregressive model

5.1 Introduction

It has been pointed out in [6] that, for the optimum energy absorption control of WEC, the future information of either the excitation force or wave elevation is needed, depending on which is used as the wave input. The analysis has been made mainly in the frequency domain. The LNOC derivation presented in the last chapter leads to the same conclusion in the time domain. Recall the control policy of LNOC:

$$u_k = K_x x_k + K_d w_{k,n_p} \tag{5.1}$$

One can notice that this equation not only states that the future information is necessary, but is also naturally a way to incorporate this non-causal information. w_{k,n_p} is the wave excitation force prediction sequence, from time instance k, n_p steps into the future. In this chapter, the autoregressive (AR) model will be introduced and used to predict the wave excitation force w_{k,n_p}. Before that, it is valuable to discuss the relation between wave elevation and wave excitation force, as well as some other wave prediction techniques.

Ocean waves harvested by WECs are normally generated by wind or storms in

the distance. With the assumption of linear waves, the wave elevation at the location of the coordinate (x,y) at time t on the sea surface can be written as the summation of a series of monochromatic waves:

$$h(x, y, t) = \sum_{n=1}^{N} H(\omega_n) \cos[k_n x + k_n y - \omega_n t + \phi(\omega_n)] \tag{5.2}$$

considering uni-directional wave. ω_n represents the angular frequency of the nth wave component and k_n is its corresponding wave number. N is the total number of frequencies adopted. $H(\omega_n)$ and $\phi(\omega_n)$ are the amplitude and phase spectrum.

On the other hand, the wave excitation force, under the same linear wave assumption, can be calculated using the same amplitude and phase spectrum. This has been briefly addressed in chapter 2, where the control-oriented model of the M4 WEC is built but presented here again for clarification. The wave excitation force $w(x, y, t)$ can be calculated as:

$$w(x, y, t) = \sum_{n=1}^{N} H(\omega_n) F_{ex}(\omega_n) \cos(k_n x + k_n y - \omega_n t + \phi(\omega_n)) \tag{5.3}$$

where $F_{ex}(\omega_n)$ is the excitation force exerted by unit amplitude monochromatic wave of frequency ω_n. In hydrodynamic software like WAMIT, when the geometry of the WEC body is defined, a range of frequency can be selected, in this case from $0.02Hz$ to $4Hz$. Then, unit amplitude monochromatic waves with these frequencies are generated as input to the linear potential flow solver, by which the hydrodynamic loads on the WEC body exerted by these waves are solved. These loads are saved as hydrodynamic coefficients, including radiation and excitation in this case. In simulations, excitation force exerted by irregular waves with spectral data $H(\omega_n)$ and $\phi(\omega_n)$ can be calculated using (5.3) by superposition principle.

Obviously if access to the actual wave spectrum data is possible, it is straightforward to transfer these data to the wave elevation or excitation force (under the linear wave assumption) through Eq. (5.2) or (5.3); however, this is only possible in numerical simulations. In practice, wave spectrum data have to be estimated by applying the Fourier transformation to the wave elevation data, which can be measured by buoys, wave gauges or other wave sensors. However, the excitation

force is generally more difficult to measure; hence, it is sometimes more preferable to use the excitation force as the input to the control system.

Given the relation between wave elevation and excitation force, there are basically three ways to introduce wave prediction to the WEC control system:

1) Instead of using the excitation force as the system input, alter the control-oriented model to take wave elevation as the system input. This can be achieved by taking the inverse Fourier transformation of Eq. (5.3) and using a state-space subsystem to approximate this convolution process with a non-causal kernel. The subsystem will have the wave elevation as the input and the excitation force as the output. It has been shown in [41] that a subsystem order of five is sufficient to represent these excitation force dynamics for a vertical cylinder in heave. The state-space subsystem can then be easily combined with the original control-oriented model. As the overall control model now takes wave elevation as the input, any predicted wave elevation can easily be incorporated by the controller.

2) Keep using the excitation force as input to the WEC model. Directly measure the wave elevation or indirectly predict the elevation at the WEC reference point. Next, use these measurements to estimate the wave spectrum data, which can then be used to calculate the future excitation force through Eq. (5.3).

3) Apply wave prediction algorithms directly to the excitation force data. As mentioned before, the excitation force is not easy to measure, which means an alternative way to acquire the excitation force data is needed. This can be done by introducing a proper observer to observe the excitation force through the WEC dynamic model and other measurable quantities, e.g. WEC motions and PTO torques.

Table 5.1 shows a more detailed comparison for these three methods. There is no obvious advantage in terms of the selection of system input. It is merely the result of different WEC modelling methods.

Table 5.1: Comparison between three prediction schemes

	method 1	method 2	method 3
model input	elevation	excitation force	excitation force
prediction on	elevation	elevation	excitation force
neediness of external sensor	elevation sensor	elevation sensor	none

On the prediction side, most of the existing wave prediction techniques are focused on elevation prediction, as it is generally more applicable to ocean engineering applications. As a result, method 1) and method 2) appear more frequently in the literature on WEC control. Deterministic sea wave prediction (DSWP) is a technique proposed to predict the future surface elevation at a specific sea location based on the measured data at a certain distance to the point of interest and a propagation model for the sea wave whose parameters can be identified from the measurements. The theory of DSWP as well as some implementation applications can be seen in [48, 49, 50]. It is reported that the DSWP can provide an accurate prediction for a few tens of seconds, which is more than enough for the LNOC even at a full scale. The price to pay is some external sensors to be deployed at a distance for collecting the elevation measurements. On the other hand, the autoregressive (AR) model has been studied in recent years for WEC control purposes [51, 52, 53]. The main differences between the AR and the DSWP are: a) the AR model does not require upstream wave measurements and; b) the AR model does not need to identify a wave propagation model like the DSWP does. It is reported that the AR model can accurately predict up to two wave periods. Overall, the AR model is relatively simpler and more cost effective. Note that in order to train the AR model, the surface elevation data at the point of interest are still required.

In this thesis, method 3) is investigated. The AR model is adopted but trained using acquired excitation force data and then used to forecast the future excitation force sequence necessary for the LNOC energy maximising algorithm. A Kalman filter with the random walk wave model (KFRW) is employed as the excitation force estimator. The benefit here is that only WEC body motion sensors are needed for wave prediction, which are normally also needed for controllers. No extra sensors are required for elevation measurements, so the cost of the control framework is relatively low compared to methods 1) and 2) in this regard. Note that these comparisons are only made under the assumption of linear and unidirectional wave propagation model, i.e. (5.2) or (5.3). In reality sea waves are multi-directional and non-linear. That being said, these methods provide a good starting point of developing wave prediction techniques for WEC control problem. In the next chapter the multi-directional wave issue will be discussed with a multi-PTO M4 system.

The two key techniques mentioned above (the excitation force estimator and the AR predictor) are discussed in the following two sections. The overall LNOC control framework is introduced after this discussion, and its efficacy is demonstrated by numerical simulations.

5.2 Short-term wave force prediction using autoregressive model

The autoregressive model is a simple and accurate model used to predict ocean wave elevation in a short prediction horizon. As discussed before, the wave elevation and the exerted excitation force are governed by the same wave spectrum data in reality. This means that if the AR model can predict the wave elevation, it should also be able to predict the exerted excitation force equally well.

The fundamental assumption of an AR model is that the value w_k depends linearly on its previous values $w_{k-p}, \ldots, w_{k-1}$, through a set of parameters $\Lambda :=$

$[\lambda_1, \ldots, \lambda_p]$. This assumption can be written in the form of

$$\hat{w}_k = \sum_{i=1}^{p} \lambda_i w_{k-i} \tag{5.4}$$

where notation $\hat{w}_k$ represents the predicted value of w_k. p is the order of the AR model. An AR model of order p is denoted as AR(p).

To resolve the set of parameters Λ, a set of training data with length N is used to train the model. Λ can be obtained by minimizing the sum of prediction errors over the training horizon N,

$$J = \sum_{k=p+1}^{N} (w_k - \hat{w}_k)^2 \tag{5.5}$$

which leads to a linear least-square (LLS) problem. The total number of data needed for one training process is $N + p$. With these $N + p$ data the AR(p) model training process can be written as,

$$\begin{bmatrix} w_{p+1} \\ w_{p+2} \\ \cdots \\ w_{p+N} \end{bmatrix} = \begin{bmatrix} w_1 & w_2 & \cdots & w_p \\ w_2 & w_3 & \cdots & w_{p+1} \\ \cdots & \cdots & \cdots & \cdots \\ w_{N-p} & w_{N-p+1} & \cdots & w_{N-1} \end{bmatrix} \begin{bmatrix} \lambda_1 \\ \lambda_2 \\ \cdots \\ \lambda_p \end{bmatrix} \tag{5.6}$$

or in matrix form

$$Y = X\Lambda \tag{5.7}$$

Solving the LLS problem gives the AR(p) coefficient set as

$$\Lambda = (X^\top X)^{-1} X^\top Y \tag{5.8}$$

The preview wave excitation force term w_{k,n_p} can then be formed by using this AR(p) model recursively with the past p estimated wave excitation forces,

$$w_{k,n_p} = [\hat{w}_k, \hat{w}_{k+1}, \ldots, \hat{w}_{k+n_p-1}]^\top \tag{5.9}$$

Although the AR model is simple to derive, there are several critical points to be addressed for the wave excitation force prediction purpose. Note that the following analysis are made by training the AR model using generated excitation

force sequence from the same JONSWAP spectrum data as used for the LNOC simulations. The trained AR model is then used to predict the successive excitation force, compared with the generated ones to show the prediction accuracy.

- **Order of the model** p

  The order of an AR model is the key to its performance. There are several methods proposed to select a suitable order for an autoregressive model, e.g. Akaike's information theoretical criterion [54]. Implementing these methods will inevitably increase the overall computational load because one needs to evaluate the fitness of the model repeatedly and change the model order accordingly. For non-causal control applications, the AR model has to be retrained at a relatively high frequency, so it is more efficient to fix the model order for a longer time. By trail and error we found $p = 100$ is a good choice for predicting wave excitation force with JONSWAP wave profile with significant wave height $H_s = 0.04m$ and different peak periods; the spectral peakedness factor is $\gamma = 1$ in all cases. Lower order gives worse prediction and high order does not increase the accuracy. Fig. 5.1 and Fig. 5.2 show the performance comparison between the reference data, AR(10) and AR(100). Blue vertical line separates the training set and the prediction set.

- **Training data length** N

  It is reported in [55] that $N \approx 15 \times p$ gives desired performance and longer training data length does not further improve the prediction accuracy. However, in a discrete time control application with high sample frequency (in this case sampling time $T_s = 0.009s$), the length of training data affects the computation efficiency. We found that by re-sampling the training data with a lower sampling rate, which means that fewer training data are used in the training process, the computation load can be reduced while not losing prediction accuracy. Fig. 5.3 shows an AR(100) model with $N = 8000$ but re-sampled with $T_s = 0.09s$ so only 800 sampling data are used. The performance improves to over 2 seconds prediction while computation time remains the same.

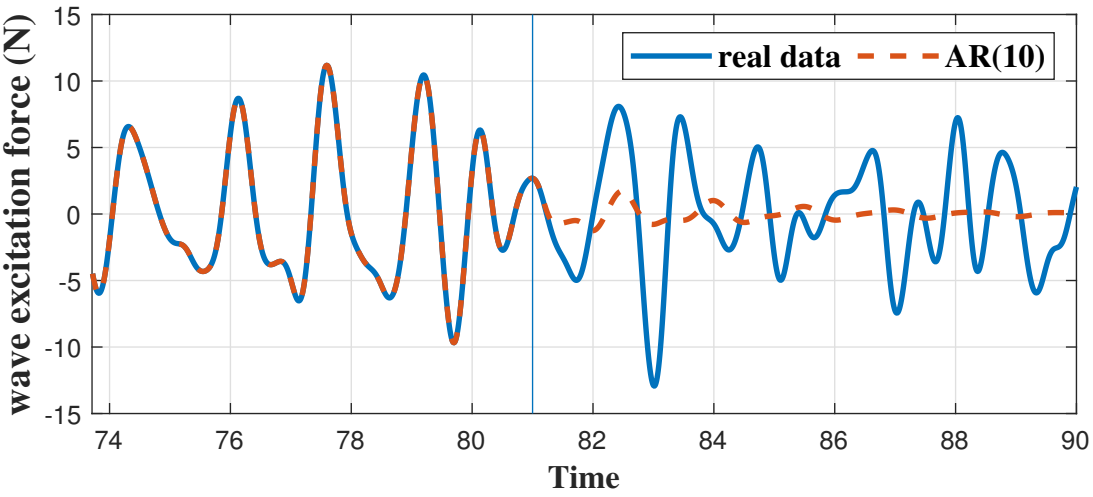

Figure 5.1: AR model with $p = 10$, $N = 800$ to predict wave excitation force in heave with JONSWAP wave peakedness factor $\gamma = 1$, significant height $H_s = 0.04m$ and peak period $T_p = 1.8s$.

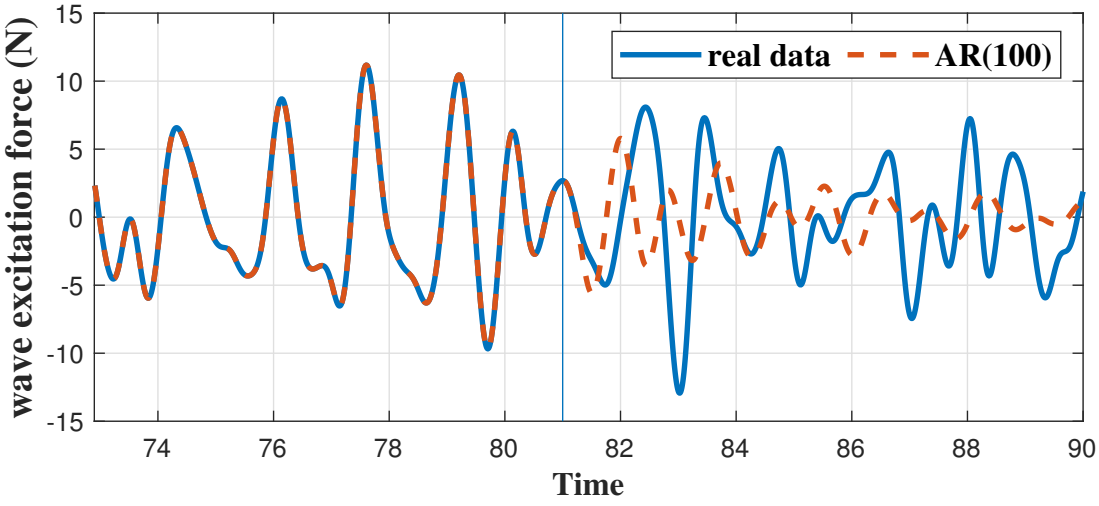

Figure 5.2: AR model with $p = 100$, $N = 800$ to predict wave excitation force in heave with JONSWAP wave peakedness factor $\gamma = 1$, significant height $H_s = 0.04m$ and peak period $T_p = 1.8s$.

- **Retrain period L**

  Theoretically speaking, the best retraining strategy is to retrain the model every time step since all estimated values are utilized instantly. But technically,

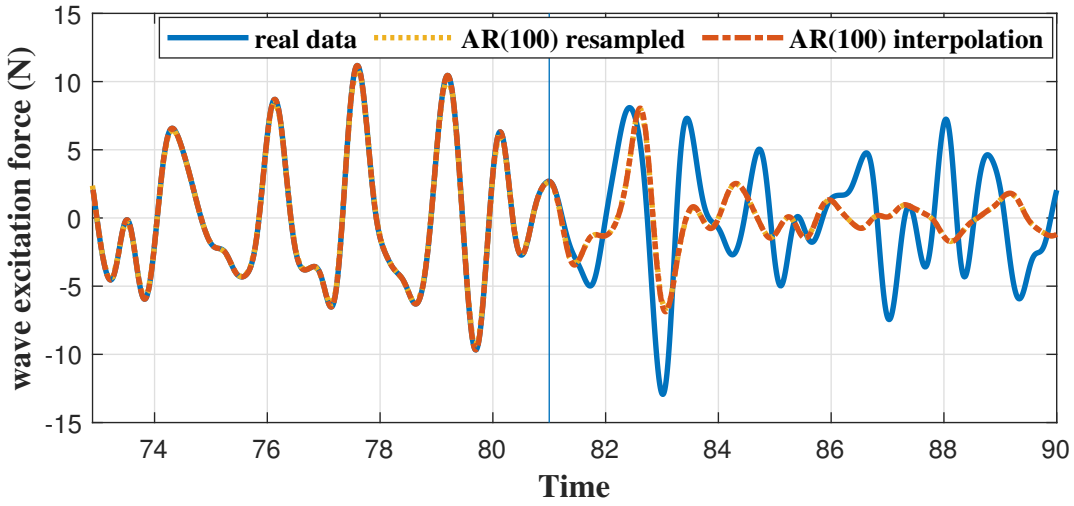

Figure 5.3: AR model with $p = 100$, $N = 8000$ re-sampled to predict wave excitation force in heave with JONSWAP wave peakedness factor $\gamma = 1$, significant height $H_s = 0.04m$ and peak period $T_p = 1.8s$.

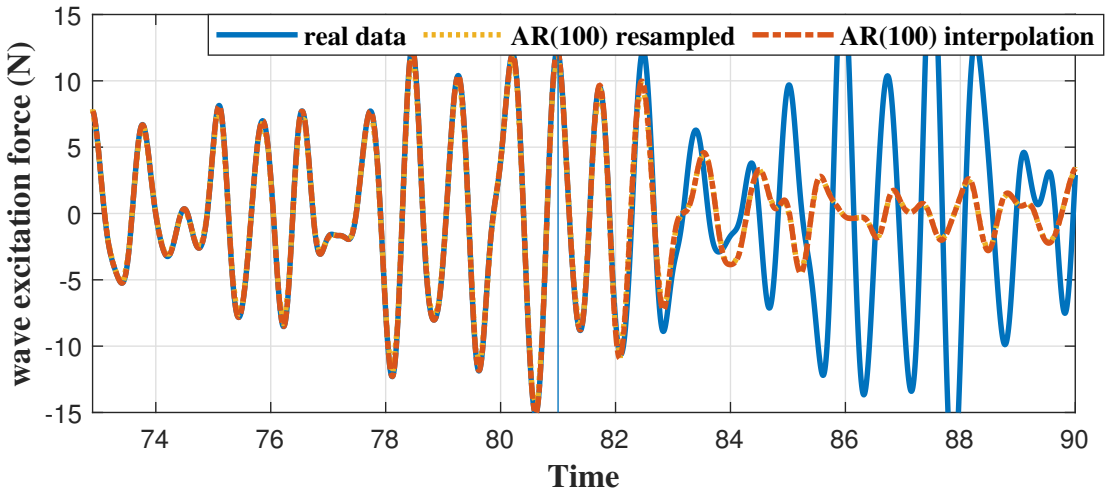

Figure 5.4: AR model with $p = 100$, $N = 8000$ re-sampled to predict wave excitation force in heave with JONSWAP wave peakedness factor $\gamma = 1$, significant height $H_s = 0.04m$ and peak period $T_p = 1s$.

it is not computationally efficient to do so. So a suitable L should be picked for balancing control performance and computation load. Since the AR(100) can predict accurately up to 2 seconds (with $T_s = 0.009s$ it means around

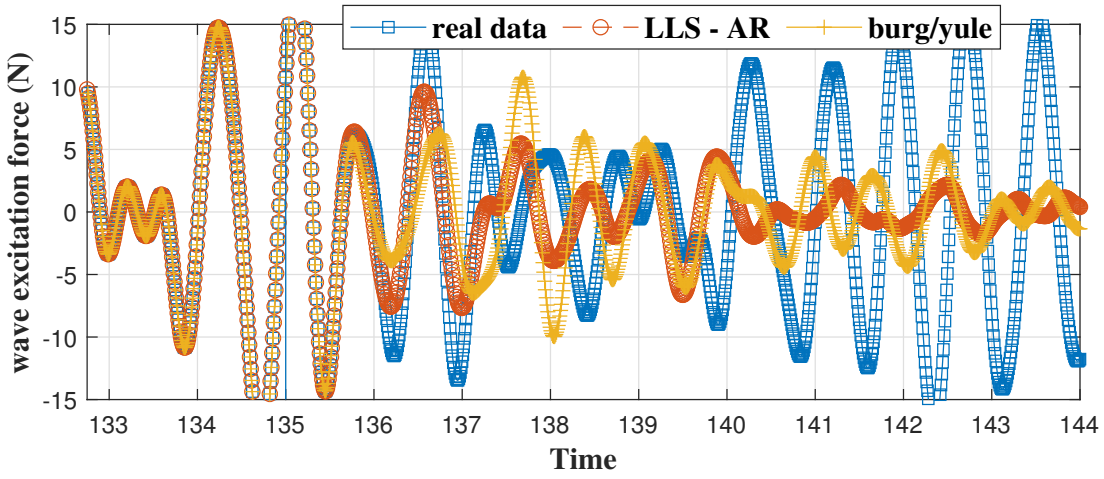

Figure 5.5: AR model with $p = 100$, $N = 800$ to predict wave excitation force in heave, with JONSWAP wave peakedness factor $\gamma = 1$, significant height $H_s = 0.07m$ and peak period $T_p = 1s$. Comparing real data, directly solving LLS and using Burg's method to guarantee stability.

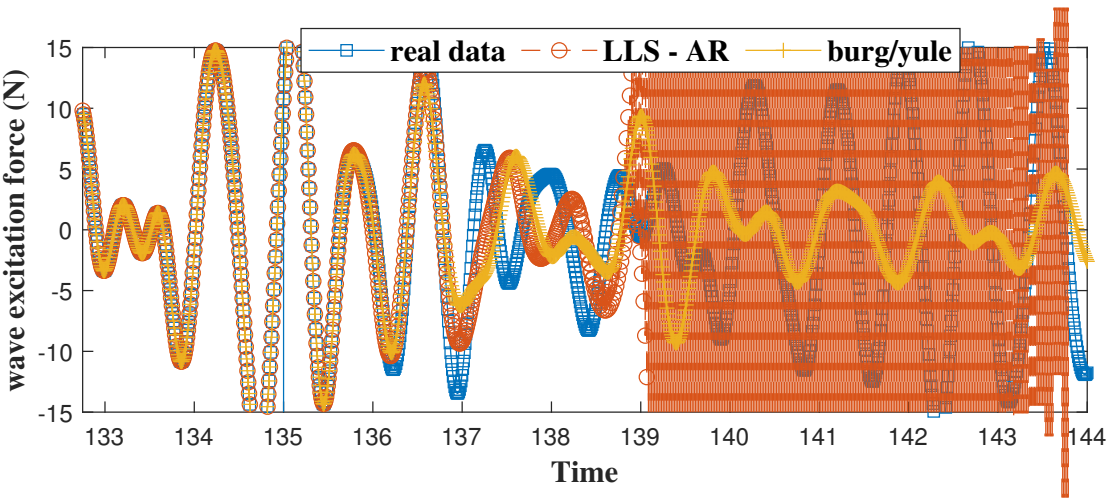

Figure 5.6: AR model with $p = 100$, $N = 1500$ to predict wave excitation force in heave, with JONSWAP wave peakedness factor $\gamma = 1$, significant height $H_s = 0.07m$ and peak period $T_p = 1s$. Comparing real data, directly solving LLS and using Burg's method to guarantee stability.

200 samples), we found that to retrain the model with $L = 100$ (half of the prediction horizon) time steps is a satisfactory option.

- **Prediction horizon n_p**

  Prediction horizon is not a tuning factor of the AR model, but of the controller. However, it will be affected by the AR model performance limitation. For optimal control performance the LNOC requires $2T_p$ prediction horizon which means 3.6 seconds or $n_p = 400$ time steps in the case of $T_p = 1.8s$. If the AR model can provide accurate and consistent prediction of $2T_p$ time, the LNOC optimal performance can be maintained. Otherwise, a shorter prediction horizon n_p should be chosen.

  Fig. 5.3 above shows that at $T_p = 1.8s$ AR predicts precisely over 2 seconds in the future but less well over 3.6 seconds, so control performance degrades at $T_p = 1.8s$ is expected. Fig. 5.4 shows a better performance with the same AR model used, but at a different peak period $T_p = 1s$. The AR model predicts precisely over 3 seconds. This is more than enough to guarantee optimal control performance. Note that peak periods from 1-1.8 seconds at tank testing scale correspond to peak periods from 6-11 seconds at full scale ocean waves, which are considered the most common sea conditions. Provided that the AR model scales well, the results we obtained here are similar to the published results in [55] reporting that the AR model can predict well for several peak periods into the future.

- **Stability of the AR wave force predictor**

  Note that directly solving the system (5.6) could result in an AR model that is unstable. This can cause severe drawback in real-time implementation of the AR predictor. Many algorithms have been developed to guarantee the stability of the AR model, e.g. Burg's method or Yule's method [56]. These methods can be used via MATLAB routines $arburg()$ and $aryule()$. Fig. 5.5 and 5.6 show the comparison between directly solving the LLS and using Burg's method. In the first figure, training data length is set to be 800 samples and the LLS solution is stable. Similar prediction accuracy can be seen from both methods. Howeverm in the second figure, when training data length is

changed to 1500 samples, instability model is provided by directly solving the LLS problem, while the AR model provided by Burg's method is still stable.

5.3 The Kalman estimator with a random walk wave model

In the last section, all the excitation force training data are generated numerically, using the predefined JONSWAP spectrum. In practice, these excitation force data are unmeasurable because all the hydrodynamic forces are coupled. In this section, the KFRW wave excitation force estimator is introduced. The basic idea is augmenting the state vector of the original state-space model to include the excitation force term w_k, then using the same linear Kalman filter to observe the original state x_k and the excitation force w_k simultaneously.

Recall the discrete-time state-space model in the last chapter,

$$\begin{aligned} x_{k+1} &= Ax_k + B_w w_k + B_u u_k \\ z_k &= Cx_k \end{aligned} \tag{5.10}$$

The system output vector z_k consists of the displacement and velocity of the WEC which can be measured by motion sensors. The task of the wave excitation force estimator is to estimate x_k and w_k based on the information of z_k and u_k.

In the KFRW method, an augmented state vector η_k is introduced to include both x_k and w_k. To this end, a mathematical model is necessary to perform the time transition of w_k. A random walk model is adopted in [57] for this purpose,

$$w_{k+1} = w_k + \epsilon_{w,k} \tag{5.11}$$

where $\epsilon_{w,k}$ is the random step at time k that w_k takes to reach w_{k+1}. This is essentially an AR model of order 1 with parameter $\lambda_1 = 1$ if $\epsilon_{w,k}$ is considered a zero-mean white noise process that is uncorrelated to any w_i with $i < k$. With some minor modifications the system equations and the random walk model can be

summarized as,

$$x_{k+1} = Ax_k + B_w w_k + B_u u_k + \epsilon_{x,k} \tag{5.12}$$

$$w_{k+1} = w_k + \epsilon_{w,k} \tag{5.13}$$

$$y_k = z_k = C_{kal} x_k + \mu_k \tag{5.14}$$

where $\epsilon_{x,k}$ represents modelling errors, y_k represents the measurement of system output (WEC motions) and μ_k represents the measurement errors. Note that the output matrix C is now $C_{kal} = [I_{8\times 8}, 0_{8\times n}]^\top$ since the displacement and velocity of all dimensions are measurable. Defining the augmented state vector as $\eta_k := [x_k, w_k]^\top$, the state-space representation of the augmented state can be written as,

$$\begin{aligned} \eta_{k+1} &= A_a \eta_k + B_a u_k + \epsilon_k \\ y_k = z_k &= C_a \eta_k + \mu_k \end{aligned} \tag{5.15}$$

where $\epsilon_k = [\epsilon_{x,k}, \epsilon_{w,k}]^\top$ is the lumped modelling error term. The state transition matrix, input and output matrices are

$$A_a = \begin{bmatrix} A & B \\ 0 & 1 \end{bmatrix} \tag{5.16}$$

$$B_a = \begin{bmatrix} B_u \\ 0 \end{bmatrix} \tag{5.17}$$

$$C_a = \begin{bmatrix} C_{kal} & 0_{8\times 4} \end{bmatrix} \tag{5.18}$$

Now the wave excitation force estimation problem becomes a state estimation problem, which can be tackled by a Kalman Filter. By the assumption of a standard Kalman Filter, the model error ϵ_k and the measurement error μ_k should be uncorrelated zero-mean white Gaussian noise process with covariance matrices Q_{kal}, R_{kal}, respectively, which are tuning parameters to ensure the estimation accuracy.

The KFRW algorithm is summarized briefly for completeness. It takes the control input u_k and output y_k from measurement as the estimator's inputs, and an estimated state information $\hat{\eta}_k$ as the output. It runs at every time step for the estimation.

We denote the former input of the non-causal controller with observer $\hat{u}_{k-1}$, and the estimated state $\hat{\eta}_{k-1}$. Firstly, calculate a priori estimation with the former state information

$$\hat{\eta}_k^- = A_a\hat{\eta}_{k-1} + B_a\hat{u}_{k-1} \tag{5.19}$$

and then the error covariance P_k^- of this priori estimation is calculated with the predefined model error covariance Q_{kal}

$$P_k^- = A_a P_{k-1} A_a^\top + Q_{kal} \tag{5.20}$$

The Kalman gain is

$$K_{kal} = P_k^- C_a^T (C_a P_k^- C_a^T + R_{kal})^{-1} \tag{5.21}$$

The estimated state information can be calculated as

$$\hat{\eta}_k = \hat{\eta}_k^- + K_{kal}(y_k - C_a\eta_k^-) \tag{5.22}$$

The last step in a Kalman algorithm loop is to update the error covariance matrix P_k for the next time step

$$P_k = (I - K_{kal}C_a)P_k^- \tag{5.23}$$

The non-causal optimal control policy with the states estimated by the KFRW estimator can be rewritten as

$$\hat{u}_k = K_x\hat{x}_k + K_d w_{k,n_p} \tag{5.24}$$

where $\hat{x}_k$ is taken from the estimated augmented state $\hat{\eta}_k$. The estimated wave excitation force can also be taken from $\hat{\eta}_k$ noted as $\hat{w}_k$. Note that the augmented state-space model is only used for estimation purpose, the control gain K_x and K_d are calculated using the original state-space model.

5.4 The comprehensive LNOC framework

The comprehensive LNOC framework to maximise energy conversion by incorporating the wave excitation force prediction can now be summarised. This framework

is shown in Fig. 5.7 by block diagrams. It systematically combines: 1) the linear non-causal optimal controller, represented by the off-line calculated control gain K_x and K_d; 2) the Kalman filter with a random walk wave model to estimate the system state x_k and the wave excitation force input w_k; 3) the autoregressive model trained by the collected excitation force data to predict the incoming excitation force sequence w_{k,n_p}.

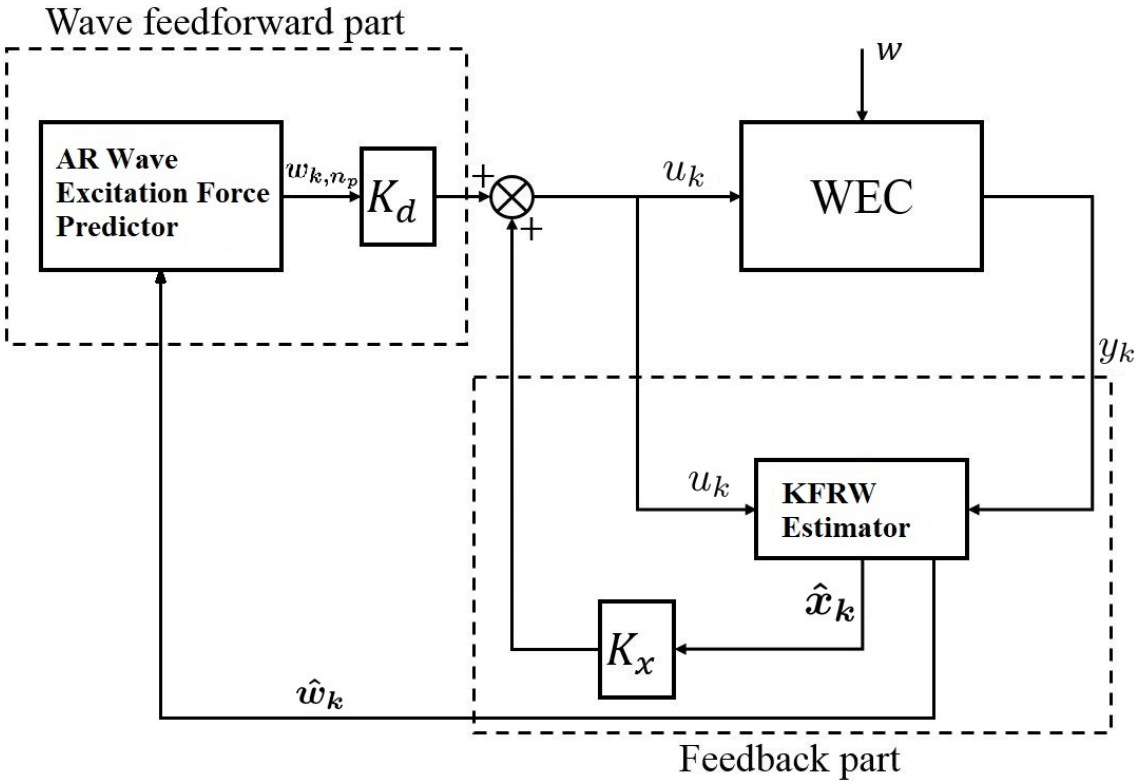

Figure 5.7: Complete linear non-causal optimal controller framework.

Compared with other non-causal control techniques, this framework does not require any external wave measurement sensors. The estimator input, PTO torque and WEC motion measurement are commonly required by any feedback controllers. The cost of deploying wave measurement units and signal processing are saved. From a computational effectiveness stand point, the linear optimal controller does not require any on-line optimization. The main contribution of computational load is from the AR wave force predictor, which is relatively not time consuming.

In the next section, numerical simulations will be carried out to demonstrate

the efficacy of the LNOC+AR framework, comparing to the ideal wave prediction performance shown in the last chapter. The computational issue will be quantified as well.

5.5 Numerical simulations

5.5.1 The LNOC+AR control efficacy

Numerical simulations are carried out to demonstrate the performance of the LNOC+AR control framework, with comparisons to the LNOC with ideal wave prediction and a well-tuned passive damper. A JONSWAP wave profile of peakedness factor $\gamma = 1$ with significant wave height $H_s = 0.04m$ is again adopted to generate wave excitation force profile. Peak periods of the sea states range from $T_p = 0.7s$ to $T_p = 1.8s$ in the simulations. The simulation time is 700 seconds, and the sampling time is set to be $T_s = 1/200T_p$.

For the AR wave excitation force predictor, the model order is chosen as $p = 100$, data length is $N = 800$, the AR predictor is retrained every half peak period, prediction horizon of the LNOC controller is chosen to be $2 \times T_p$ seconds. The main focus of the simulation results is to evaluate the degradation of control performance caused by the prediction errors of the AR predictor.

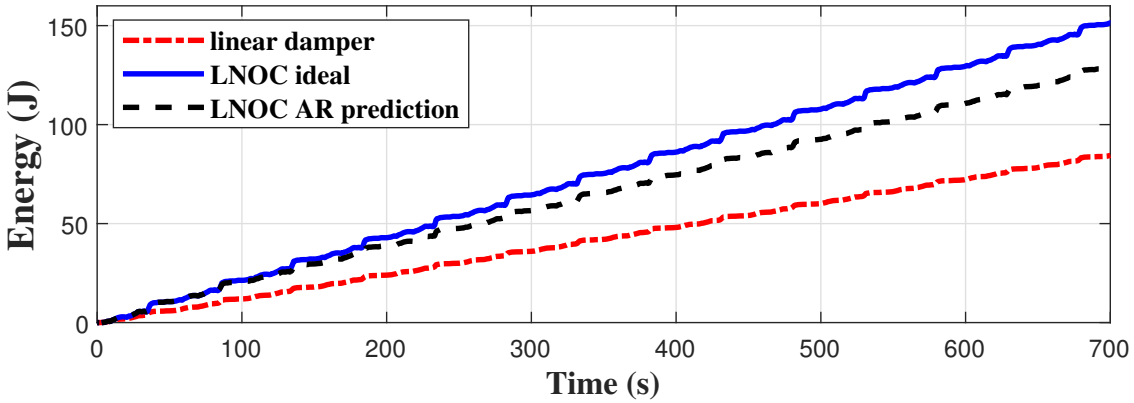

Figure 5.8: Energy captured, JONSWAP wave profile peakedness factor $\gamma = 1$, $H_s = 0.04m$, $T_p = 1.8s$.

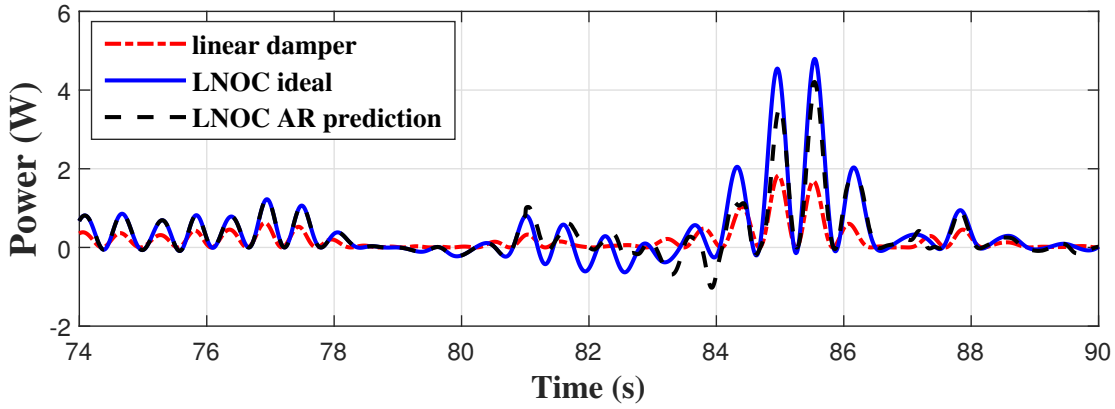

Figure 5.9: Power, JONSWAP wave profile peakedness factor $\gamma = 1$, $H_s = 0.04m$, $T_p = 1.8s$.

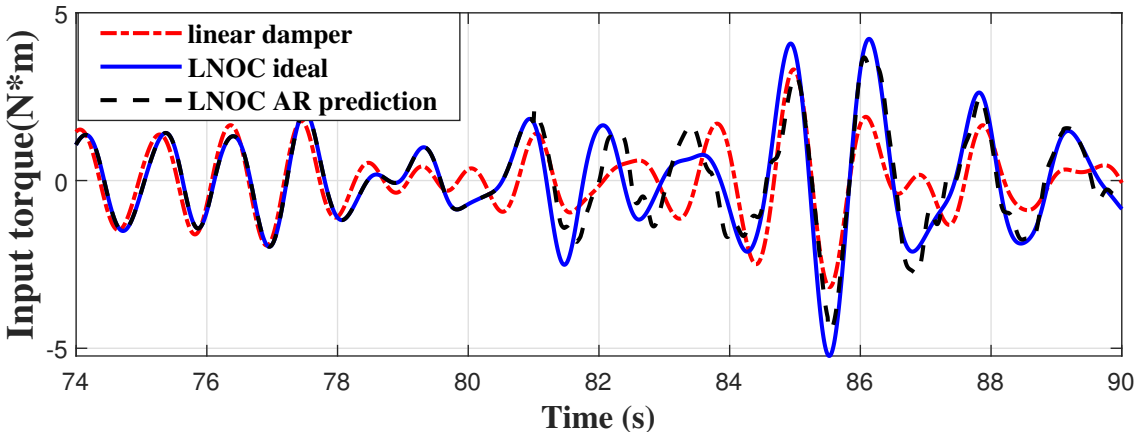

Figure 5.10: Input torque, JONSWAP wave profile peakedness factor $\gamma = 1$, $H_s = 0.04m$, $T_p = 1.8s$.

Fig. 5.8 shows the energy output of the WEC. For the passive damper case, energy output is $85.76J$. The LNOC with ideal prediction case reaches $153.55J$ (79% improvement) while the LNOC with AR predictor case ends at $130.66J$ (52% improvement). Fig. 5.9 shows the corresponding power plot. The better the AR predictor performs, the better the black line follows the ideal blue line in the figure. This can be used as an indicator to evaluate the performance of the AR model. It has been shown in Fig. 5.3 that at around 81 seconds of the simulation, the AR model does not provide accurate prediction up to $2T_p$ time, so in Fig. 5.9 at the

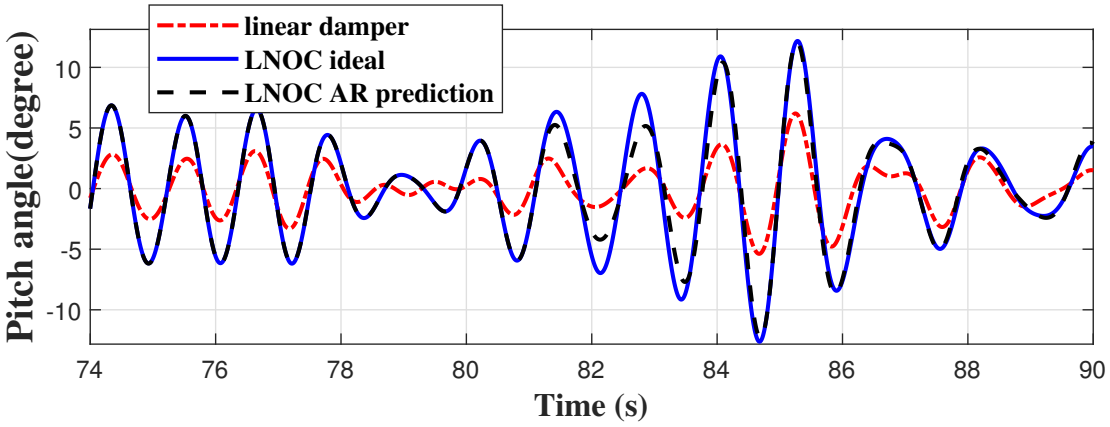

Figure 5.11: Pitch angle, JONSWAP wave profile peakedness factor $\gamma = 1$, $H_s = 0.04m$, $T_p = 1.8s$.

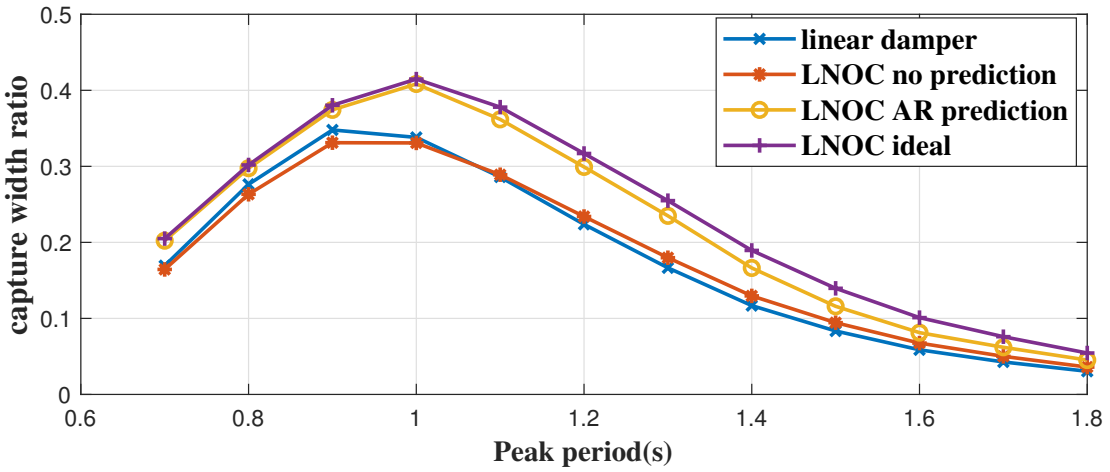

Figure 5.12: Capture width ratio, JONSWAP peakedness factor $\gamma = 1$, wave profile $H_s = 0.04m$, wave excitation force prediction horizon is $2 \times T_p$.

same time the black line starts to depart from the ideal blue line. In the meanwhile, the control input in Fig. 5.10 starts to have minor oscillations, while the pitch angle in Fig. 5.11 has smaller amplitude than the ideal case.

The overall control performance for different peak periods can be characterised by the CWR plot in Fig. 5.12. Twelve simulations of different peak periods ranging from $T_p = 0.7s$ to $T_p = 1.8s$ are run to evaluate all the CWRs. Significant wave height is fixed at $H_s = 0.04m$ although this is normalised in CWR. Fig. 5.12 validates that for shorter peak periods, the AR model performance is better, so is

the LNOC performance. The overall control performance degradation caused by the inaccuracy of the AR wave excitation force predictor is not significant. This can be also seen from Table 5.2 by comparing the CWR values of AR prediction and ideal prediction.

Table 5.2: LNOC performance in CWR

Peak period	passive damper	LNOC no prediction	LNOC AR prediction	LNOC ideal prediction
0.7s	0.169	0.164	0.202	0.205
0.8s	0.276	0.263	0.300	0.302
0.9s	0.348	0.331	0.374	0.380
1.0s	0.338	0.331	0.408	0.415
1.1s	0.286	0.289	0.362	0.378
1.2s	0.224	0.234	0.300	0.317
1.3s	0.167	0.180	0.235	0.255
1.4s	0.117	0.130	0.166	0.189
1.5s	0.083	0.094	0.116	0.140
1.6s	0.059	0.068	0.081	0.101
1.7s	0.043	0.050	0.062	0.076
1.8s	0.030	0.036	0.045	0.055

5.5.2 Computational effectiveness

Finally, some evaluations on computational load are given to show that the LNOC framework with AR predictor is applicable for real-time implementation. The average computational time for the whole simulation is 0.0035 second which is less than the designed sampling time 0.009 second. For time steps that AR model is

retrained, the computational time is roughly 0.1 second. This is larger than the sampling time so the AR model should be retrained at a slower rate separately. Because the retraining happens every half T_p time and the AR model can predict up to $2 \times T_p$ time, the computational time of $0.1s$ is acceptable. For time steps that retraining does not happens, the computational time is trivial since the controller is computed off-line. Note that at full scale the time scale is at least 6 times longer than the laboratory scale, so real time control becomes even easier.

Chapter 6

Modelling and control of Mutli-PTO M4 in multiple directional waves

In Chapter 4 and 5, the LNOC framework integrated with the KFRW wave force estimator and AR wave force predictor has been investigated. Significant energy conversion improvement is demonstrated through numerical simulation results, by applying the LNOC+AR framework to the single PTO 3-float (1-1-1) M-WEC M4.

As mentioned in Chapter 2, increasing the number of mid and stern floats results in various configurations of the M-WEC M4. This may enable multiple PTOs to be installed within one WEC device, further improving the single device power capture capability. For example the 6-float (1-3-2) M4 has two PTOs and the 8-float (1-3-4) M4 has four PTOs that can operate in parallel. A design diagram of the 1-3-4 M4 can be viewed in Fig. 6.1.

In this chapter, the genericness of the LNOC+AR framework is demonstrated by extending the methodology to be applied on the 8-float (1-3-4) M4 WEC with four PTOs. Compared to the previous studied 3-float (1-1-1) M4, the dynamic model order further increases due to the additional PTOs. The control problem now becomes a multiple input one.

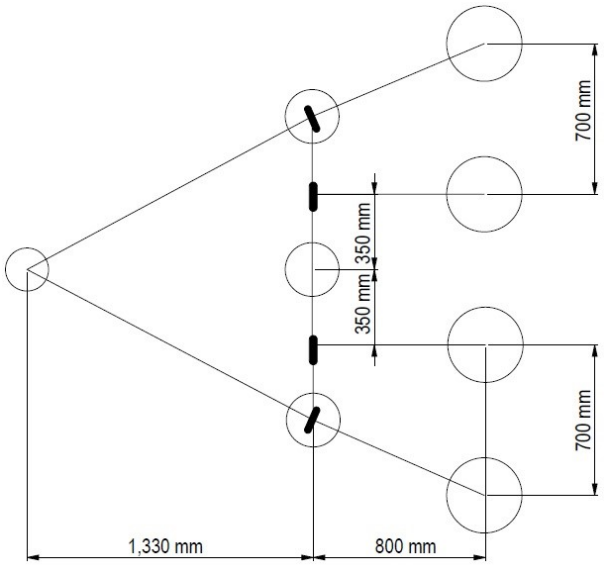

Figure 6.1: 8-float 1-3-4 M4 WEC plan view at laboratory scale. The four thick lines denote the hinges for PTO.

Besides, it has been assumed so far that the WEC aligns with the wave direction. In reality the WEC may veer away from this due to currents or windage, although currents are small in ocean conditions and wind is often aligned with the wave direction. Nevertheless this effect should be quantified to see how energy conversion can be affected. When non-zero degree heading occurs, the roll and sway motion of the WEC is not trivial any more. In order to quantified this effect, the hydrodynamic model of the WEC has be to extended to allow roll and sway motion as well as surge, heave and pitch, which introduces more challenges for the controller and wave predictor design.

6.1 Control-oriented state-space model

In this section the control-oriented state-space model for the 1-3-4 M4 is built. Since the modelling method is the same as what has been discussed in Chapter 3, only the parts that differ from the 1-1-1 M4 case will be reported, to showcase how the complexity of the model increases.

In Fig.6.1, the eight floats are indexed by $i = 1, 2, \ldots, 8$ from left to right and

from bottom to top, respectively. Coordinate origin O is at the hinge height above the mid float ($i = 3$) with x (surge) pointing towards right, y (sway) upwards and z (heave) outwards from the paper. Each float (i) has five degrees of freedom (DOF): surge, sway, heave, roll, pitch. Incoming wave angle is fixed and thus yaw can be neglected. For a float i, x_i, y_i, z_i are used to denote surge, sway and heave. Roll, pitch with respect to the WEC origin O are denoted by ψ_i, θ_i.

The generalized motion vector of the WEC can be chosen as :

$$q = [x_o, y_o, z_o, \psi_o, \theta_l, \theta_5, \theta_6, \theta_7, \theta_8]^\top \tag{6.1}$$

where θ_l is the pitch motion for the first four floats. θ_l equals θ_i for $i = 1, 2, 3, 4$ since they are one rigid body. θ_5, θ_6, θ_7, θ_8 are pitch motion of floats $5, 6, 7, 8$. All floats have the same roll motion ψ_o.

Denote h_i, t_i and v_i the horizontal, transversal and vertical distance from the gravitational center of float i to origin O. The translational motion of each float can be calculated by the following formulae, assuming small angle linearisation:

$$x_i = x_o + h_i - \theta_i v_i \tag{6.2}$$

$$y_i = y_o + t_i + \psi_o v_i \tag{6.3}$$

$$z_i = z_o + v_i - \theta_i h_i + \psi_o t_i \tag{6.4}$$

The motion equation for the 8-float M4 can be derived using Lagrangian equation as for the 3-float M4 in Chapter 3 or by applying Newton's second law at each DOF and merge into matrix form. The motion equation is in the following form:

$$M\ddot{q}(t) = f_{e,q}(t) + f_{rd,q}(t) + f_{rs,q}(t) + f_{pto,q}(t) \tag{6.5}$$

In this equation, M is the mass and inertia matrix of size 9×9, shown in Eq. (6.6). m_i applies to masses associated with each float 1-4, including float, ballast and beam, and terms with $\sum m_{5-8}$ also include associated masses of float, ballast and beam for floats 5-8. I_ψ denotes the inertia of roll of the WEC. I_{1234} denotes the inertia of floats 1 to 4 in pitch and I_5 to I_8 denote those of the other floats. All

inertias are relative to the origin O. All these specifications can be seen in Appendix A.

$\ddot{q}$ is the second derivative of q. On the right hand side there are linear wave forces including excitation force, radiation damping force, hydrostatic restoring force and the controllable PTO torque, respectively. Mooring force in the experiment and model for 6-float M4 caused the horizontal motion to be less than 1 cm [15], which has negligible effect on phase in this model.

$$M = \begin{bmatrix} \sum_{i=1}^{8} m_i & 0 & 0 & 0 & -\sum_{i=1}^{4} m_i v_i & -\sum m_5 v_5 & -\sum m_6 v_6 & -\sum m_7 v_7 & -\sum m_8 v_8 \\ 0 & \sum_{i=1}^{8} m_i & 0 & \sum_{i=1}^{8} m_i v_i & 0 & 0 & 0 & 0 & 0 \quad 0 \\ 0 & 0 & \sum_{i=1}^{8} m_i & \sum_{i=1}^{8} m_i t_i & -\sum_{i=1}^{4} m_i h_i & -\sum m_5 h_5 & -\sum m_6 h_6 & -\sum m_7 h_7 & -\sum m_8 h_8 \\ 0 & \sum_{i=1}^{8} m_i v_i & \sum_{i=1}^{8} m_i t_i & I_\psi & -\sum_{i=1}^{4} m_i h_i t_i & -\sum m_5 h_5 t_5 & -\sum m_6 h_6 t_6 & -\sum m_7 h_7 t_7 & -\sum m_8 h_8 t_8 \\ -\sum_{i=1}^{4} m_i v_i & 0 & -\sum_{i=1}^{4} m_i h_i & -\sum_{i=1}^{4} m_i t_i & I_{1234} & 0 & 0 & 0 & 0 \\ -\sum m_5 v_5 & 0 & -\sum m_5 h_5 & -\sum m_5 h_5 t_5 & 0 & I_5 & 0 & 0 & 0 \\ -\sum m_6 v_6 & 0 & -\sum m_6 h_6 & -\sum m_6 h_6 t_6 & 0 & 0 & I_6 & 0 & 0 \\ -\sum m_7 v_7 & 0 & -\sum m_7 h_7 & -\sum m_7 h_7 t_7 & 0 & 0 & 0 & I_7 & 0 \\ -\sum m_8 v_8 & 0 & -\sum m_8 h_8 & -\sum m_8 h_8 t_8 & 0 & 0 & 0 & 0 & I_8 \end{bmatrix} \tag{6.6}$$

Hydrodynamic coefficients for calculating linear wave forces are again obtained from WAMIT software [43]. These include all cross-coupled terms among floats. Since there are totally eight floats and each with six DOFs (yaw included but trivial), the size of hydrodynamics coefficients from WAMIT are 48×48. Converting them into 9×9 accordingly makes state-space modelling more straightforward. The processes are omitted here as similar to what has been presented in Chapter 3. The final state-space model is reported directly.

A new state vector $x := [q,\ \dot{q},\ z_s]^\top$ is defined, so that the state-space representation of the 8-float M4 control-oriented model can be written as

$$\begin{aligned} \dot{x} &= Ax + Bf_{e,q}(t) + Bf_{pto,q}(t) \\ y &= Cx + Du \end{aligned} \tag{6.7}$$

where the system matrices are

$$A = \begin{bmatrix} 0_{9\times 9} & I_{9\times 9} & 0_{9\times n} \\ -(M+A_\infty)^{-1}K & -(M+A_\infty)^{-1}D_s & -(M+A_\infty)^{-1}C_s \\ 0_{n\times 9} & B_s & A_s \end{bmatrix} \tag{6.8}$$

$$B_w = \begin{bmatrix} 0_{9\times 9} \\ (M+A_\infty)^{-1} \\ 0_{n\times 9} \end{bmatrix} \tag{6.9}$$

$$B_u = \begin{bmatrix} 0_{9\times 1} \\ (M+A_\infty)^{-1}[0,0,0,0,1,-1,-1,-1,-1]^\top \\ 0_{n\times 1} \end{bmatrix} \tag{6.10}$$

$$C = \begin{bmatrix} 0_{1\times 13} & 1 & -1 & 0 & 0 & 0 & 0_{1\times n} \\ 0_{1\times 13} & 1 & 0 & -1 & 0 & 0 & 0_{1\times n} \\ 0_{1\times 13} & 1 & 0 & 0 & -1 & 0 & 0_{1\times n} \\ 0_{1\times 13} & 1 & 0 & 0 & 0 & -1 & 0_{1\times n} \end{bmatrix} \tag{6.11}$$

Without control, the PTO torques are modelled as four passive dampers with the same damping constant B_{mech}. Note that the value of M_{mech} is selected by trail and error for best power capture performance.

The order of the state-space model derived for the 8-float 1-3-4 M4 is now around six hundreds, while for the 3-float 1-1-1 M4 it was slightly above a hundred.

Note that with non-zero degree headings, the excitation force coefficients F_{ex} and ϕ are changed. These are pre-calculated for headings ranging from 0 degree to 90 degrees, with 10 degrees interval. Other hydrodynamic coefficients are the same for various headings, so are the state-space representation.

6.2 LNOC+AR efficacy on the 8-float M4

The LNOC+AR control framework is now applied to the 8-float 1-3-4 M4. Numerical simulations are carried out to demonstrate control performances. These are presented in two parts: zero degrees heading angle and non-zero degrees heading angles. For both cases, sampling time is set dependent on peak period $T_s = T_p/200$ to maintain 200 time steps run in each peak period. For one simulation 100 peak periods are run. For each specific sea state one simulation is completed within ten minutes.

JONSWAP wave spectra with peakedness factor of 1 and 3.3 are both used to generate wave profiles. Significant wave height is fixed at $H_s = 0.04m$ although this

is normalized by the performance index CWR. Peak periods range from $T_p = 0.7s$ to $1.8s$, each with $0.1s$ interval. For Froude scaling these are 4.95 to 12.7 seconds in full scale which is typically 50 times the model scale. These wave profiles are fed as disturbances to the WEC model and WEC responses are recorded to calculate absorbed energy. For fair comparison to a passive damper only one set of control parameters Q and R are used for all wave conditions. The passive damping ratio $B_{mech} = 3NMs/rad$, identical for 4 PTOs.

6.2.1 Zero degree headings

Fig.6.2 shows the CWR plot for different peak periods. This can be viewed equivalently as normalised power capture and enables comparison to some idealised optimum value for point absorbers and hinged rafts in regular waves [6, 11]. Note that the CWR is independent of significant wave height.

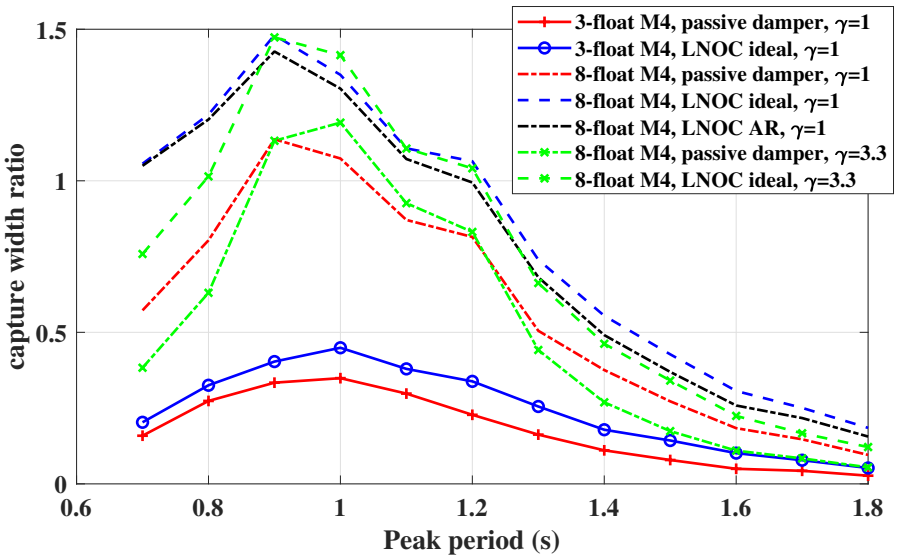

Figure 6.2: Capture width ratio, significant wave height $H_s = 0.04m$, zero degrees heading. Comparing the 3-float M4 CWR which was validated by experimental data with the 8-float M4 CWR derived by simulations.

In Fig.6.2 the solid line with '+' sign shows the CWR of 3-float M4 with a passive damper which has been validated by experiment data. This provides justification

for the fidelity of the 8-float M4 model as no experiment has been carried out yet. It can be seen that without control, the maximum CWR is 0.35 for the 3-float M4 with 1 PTO. For the 8-float M4 with 4 PTOs this is 1.13, slightly less than 4 times of the 3-float case.

The LNOC is applied to the 8-float M4 with incoming wave predictions. It can be seen that with LNOC and ideal prediction, the CWR at $Tp = 0.9s$ increases from about 1.13 to about 1.47 which is 30% improvement. At $Tp = 1.8s$ this improvement goes up to 93%. The average improvement for all peak periods is around 53%. The CWRs of 3-float M4 with passive damper and LNOC are also presented at the bottom. Control performances are similar for both WECs.

The AR model with non-perfect wave force predictions (black dash line) brings performance degradation but improvements of capture width are still significant compared to the passive damper case, in this case from 21% to 83%. These are run with a JONSWAP spectra with $\gamma = 1$.

To demonstrate that the LNOC also works in a narrow band spectrum, the JONSWAP spectra with $\gamma = 3.3$ is also shown in Fig.6.2 as the dash line with "x" symbol. The control performance is similar to the $\gamma = 1$ case.

Fig.6.3 to Fig.6.4 show the time responses at $T_p = 1.0s$, comparing the passive damper and LNOC with ideal wave force predictions and AR predictions. These include the PTO torque (control input) and the power capture for all the PTOs. It is clear that at zero degrees heading all PTOs are operating in parallel and their responses are almost identical. This shows the LNOC is able to control 4 PTOs simultaneously and enables the same power capture improvement for all of them.

6.2.2 Non-zero degree headings

Fig. 6.5 and 6.6 show the comparison of excitation force in heave and pitch mode, which contribute most to the average power. Readers should see how excitation force in these modes decrease as incoming wave angle increases.

Fig. 6.7 and Fig. 6.8 shows the CWR trends of passive damper and LNOC for

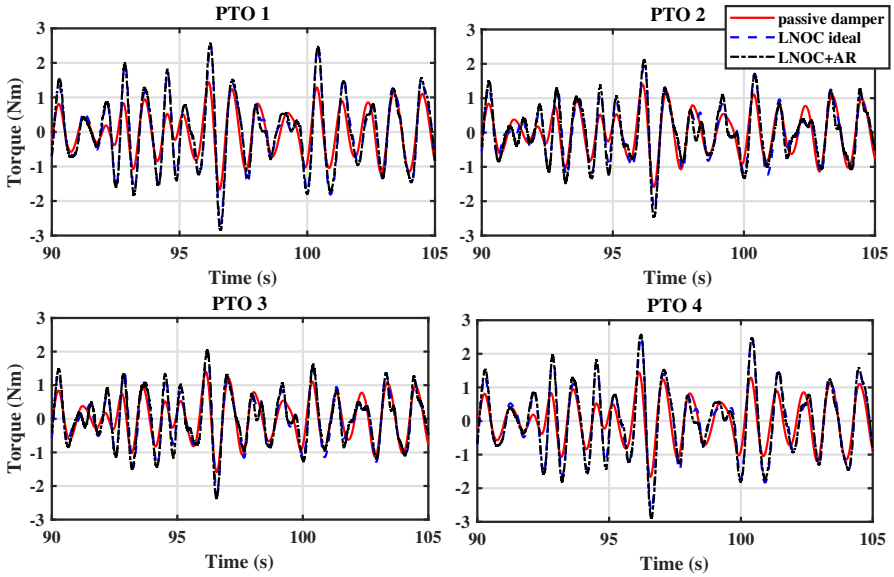

Figure 6.3: PTO control torque, significant wave height $H_s = 0.04m$, peak period $T_p = 1.0s$, $\gamma = 1$, zero degrees heading.

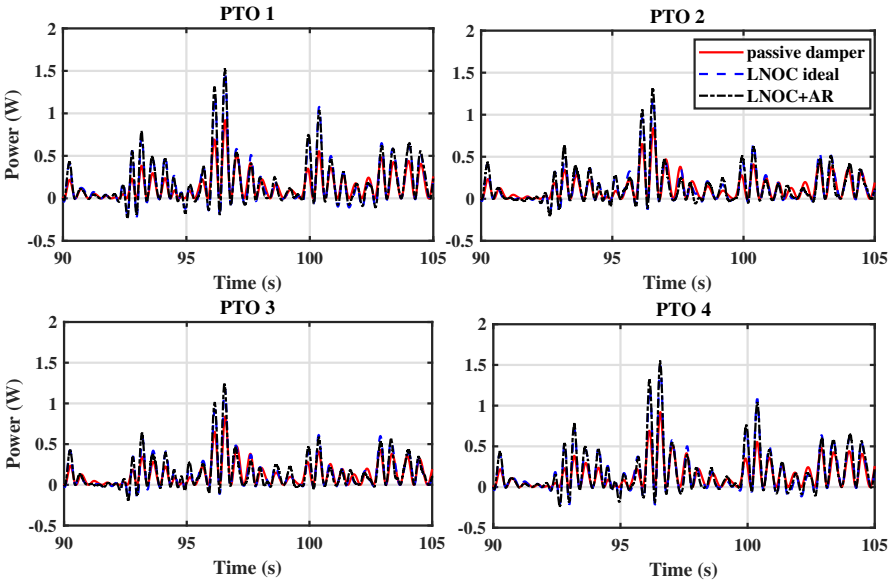

Figure 6.4: Instant power, significant wave height $H_s = 0.04m$, peak period $T_p = 1.0s$, $\gamma = 1$, zero degrees heading.

$T_p = 1.0s$ when WEC headings change from 0 degrees to 90 degrees, respectively for $\gamma = 1$ and $\gamma = 3.3$. Orange lines show rotation angles of roll motion and the RMS pitch angles for 4 PTOs in average.

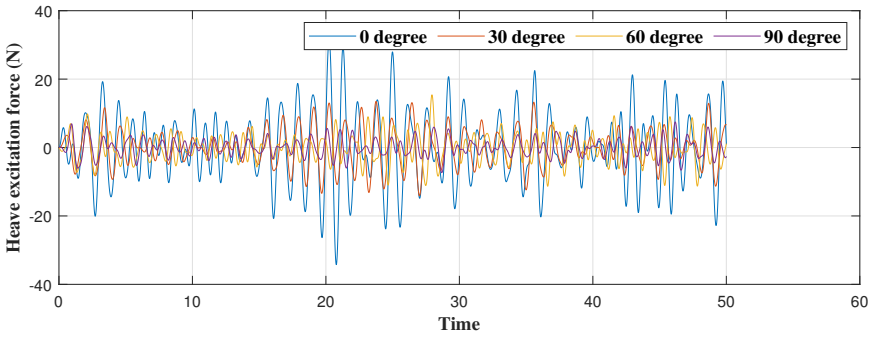

Figure 6.5: Excitation force in heave mode for various headings, significant wave height $H_s = 0.04m$, peak period $T_p = 1.0s$, $\gamma = 1$.

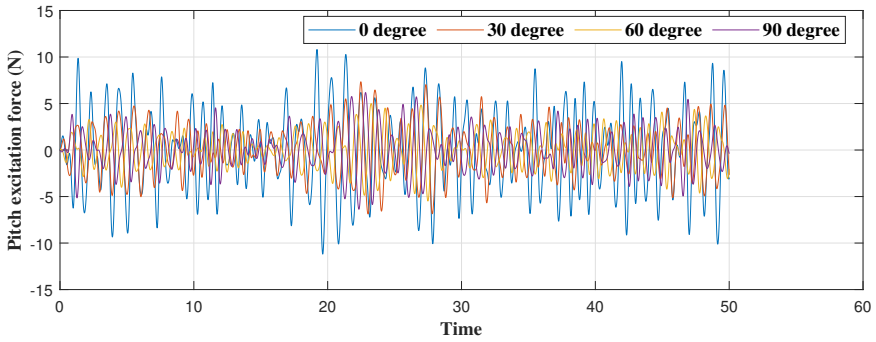

Figure 6.6: Excitation force in heave mode for various headings, significant wave height $H_s = 0.04m$, peak period $T_p = 1.0s$, $\gamma = 1$.

It can be observed that as incoming wave angle increases from zero, the relative pitch angle decreases, so do the CWRs. The roll motion of the whole WEC increases from almost zero at zero heading to a significant value compared with pitch at 30 degrees heading and then stays relatively stable. As the heading increases from 0 to 90 degrees, it can be observed clearly that as the roll motion increases, the pitch motion decreases.

The LNOC controller, for both ideal wave force prediction and AR cases, can improve CWR for all WEC heading angles. Surprisingly, the improvements for non-zero headings are more significant than for zero heading.

These observations are not sensitive to the change of peakness factor γ, which can be noticed by compared every two plots with the same peak period but different

value of γ. Fig. 6.9 to Fig. 6.14 show the comparisons made in different peak periods.

In a more realistic scenario, the WEC heading is likely to fluctuate around zero as wind and current exist. This result with unchanged control parameters ensures the LNOC can be applied and improve power capture of the WEC regardless of change of the WEC headings.

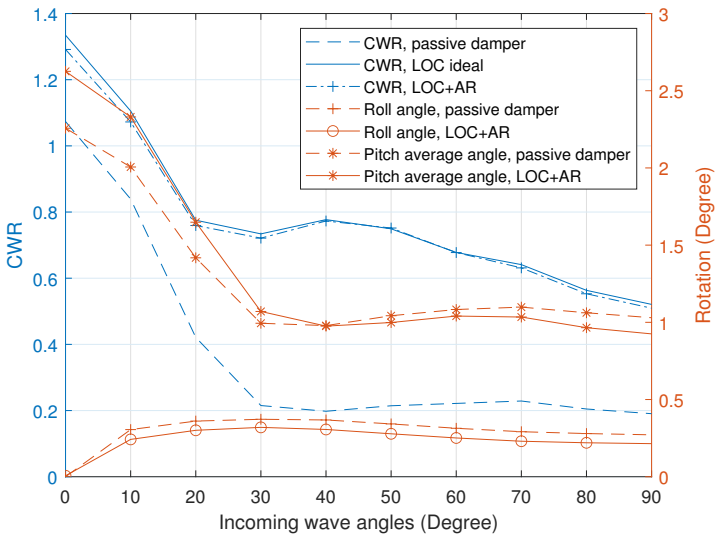

Figure 6.7: Left Y axis: CWR of passive damper and LNOC. Right Y axis, rotation motion angle (RMS value) of pitch and roll. X axis wave heading angle from 0 degrees to 90 degrees. Significant wave height $H_s = 0.04m$, peak period $T_p = 1.0s$, $\gamma = 1$.

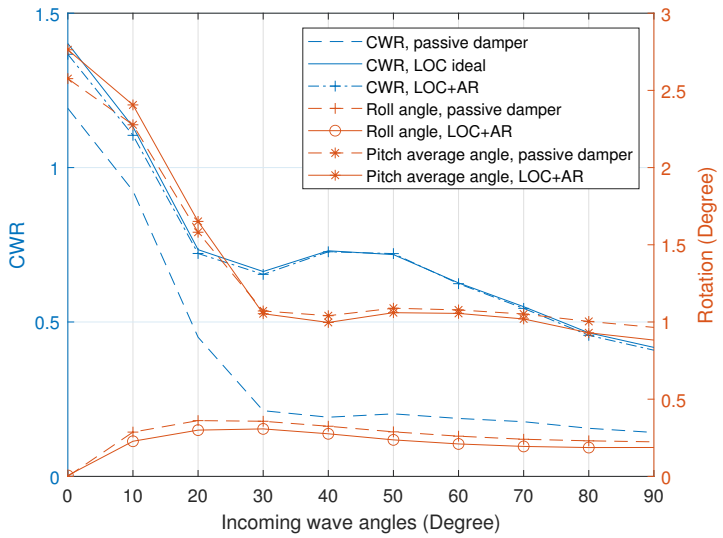

Figure 6.8: Left Y axis: CWR of passive damper and LNOC. Right Y axis, rotation motion angle (RMS value) of pitch and roll. X axis wave heading angle from 0 degrees to 90 degrees. Significant wave height $H_s = 0.04m$, peak period $T_p = 1.0s$, $\gamma = 3.3$.

6.3 Discussion of the results

The results obtained so far in this thesis show that high capacity wave energy systems are possible by capturing energy from multiple floats with multi-mode forcing, as incorporated in the M4 configuration. It is useful to compare the maximum possible CWR for point absorbers and hinged beam raft-type absorbers, available for regular waves at resonance. For point absorbers the maximum capture width ratio, normalised by wave length, is $1/2\pi$ for heave, $1/\pi$ for surge and pitch and $3/2\pi$ in combination [6]. For the hinged beam it is $4/3\pi$ [11]. In the 1-3-4 case here we have an M-WEC with 4 PTOs. For zero heading, as intended, if we considered this as 4 hinged beams the maximum CWR would be 1.7 while a maximum value of 1.2 is achieved in irregular waves, 1.5 with LNOC framework applied. If we considered 4 point absorbers operating in heave, surge and pitch the maximum value would be 1.9. If we considered this as 4 point absorbers and 4 hinged beams in combination then the maximum would be 3.6. But this would require $3 \times 4 = 12$ floats and here

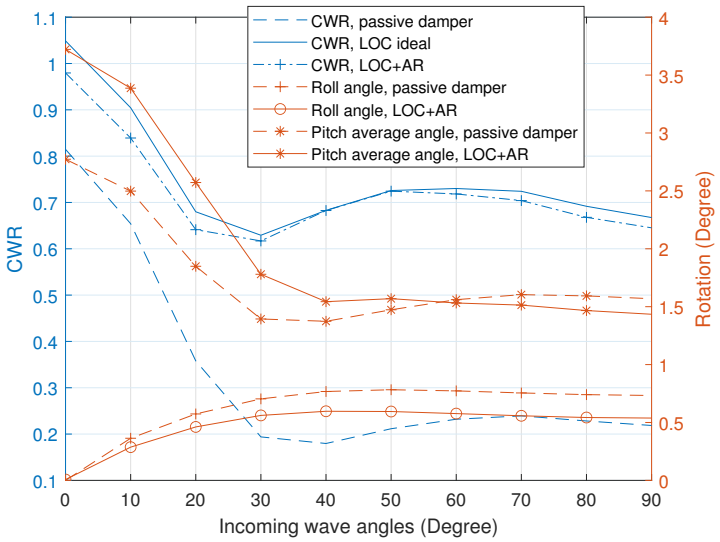

Figure 6.9: Left Y axis: CWR of passive damper and LNOC. Right Y axis, rotation motion angle (RMS value) of pitch and roll. X axis wave heading angle from 0 degrees to 90 degrees. Significant wave height $H_s = 0.04m$, peak period $T_p = 1.2s$, $\gamma = 1$.

we only use 8. A crude estimate of theoretical maximum might thus be 2.4. The intention is to compare with what is theoretically possible for power absorption. If this were to be called efficiency it would be around 62.5%.

With different headings the contributions from each mode will be different. However for a heading of 90 degrees the 4 stern floats are responding mainly in heave and the maximum CWR would be 0.63. With LNOC this is achieved with $T_p = 1.2s$ and $1.4s$ giving 100% efficiency while for $T_p = 1s$ and $1.8s$ it is 0.55 and 0.4 giving efficiencies of 87% and 63%. When converted into power, this is now greater for $T_p = 1.8s$ and $1.4s$ than for $T_p = 1.2s$ and $1s$. The system was designed for zero heading which will be the case for ocean conditions with small currents. With currents, e.g. on continental shelf regions, the situation is complex with variable heading and the optimum float configuration for maximum energy capture needs to be determined. For this configuration the average power is between 0.4 and $1.2W$ corresponding to 0.35 and $1.1MW$ at 1:50 scale with $H_s = 2m$. This would relate to

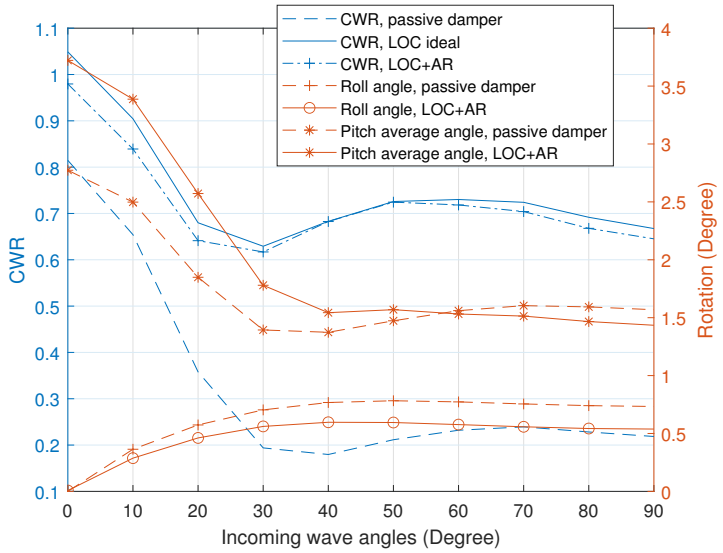

Figure 6.10: Left Y axis: CWR of passive damper and LNOC. Right Y axis, rotation motion angle (RMS value) of pitch and roll. X axis wave heading angle from 0 degrees to 90 degrees. Significant wave height $H_s = 0.04m$, peak period $T_p = 1.2s$, $\gamma = 3.3$.

the average wave conditions at Wavehub. But the average power is now comparable to off-shore wind turbines and this is clearly desirable for the further development of wave energy conversion system.

6.3.1 Discussion on power quality

Apart from maximising the average absorbed power, power quality is another important aspect of WEC technology development. A key performance index of power quality is the Peak to Average (P2A) ratio of the absorbed mechanical power. A high P2A ratio is not favourable for PTO design as the high voltage can damage power electronic components in the PTO. There are many potential ways to improve the power quality of WEC, for example an well-design layout of WEC array can reduce the total P2A by a factor of four by enabling the WEC to interact with the incoming wave out of phase and share the same DC-link, results reported in [58]. Energy storage and reactive power compensation can have huge impact in improving power

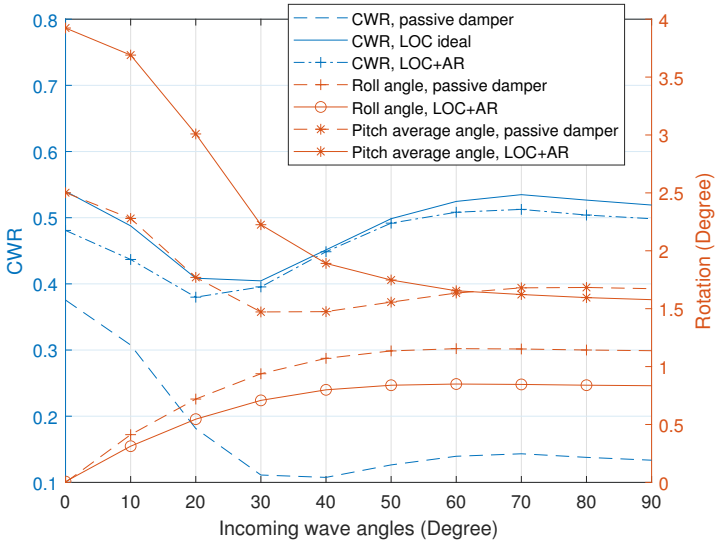

Figure 6.11: Left Y axis: CWR of passive damper and LNOC. Right Y axis, rotation motion angle (RMS value) of pitch and roll. X axis wave heading angle from 0 degrees to 90 degrees. Significant wave height $H_s = 0.04m$, peak period $T_p = 1.4s$, $\gamma = 1$.

quality as well [59].

Energy maximising control will have an impact on the P2A ratio of WEC, although this is hard to quantified as control will increase both the peak and average power. Control algorithms can be developed to explicitly limit/handle the undesirably high P2A ratio but can conflicts the maximisation of energy output. Improving power quality of WEC is overall a co-design problem.

Here, the potential advantage of multi-PTO M-WEC can have in improving power quality will be discussed. Fig. 6.15 shows the total power of the four PTOs when the WEC is operating at zero degree heading and the four PTOs are working in phase, resulting in a spiky peak power. In Fig. 6.16, the WEC is operating at 40 degrees heading, which means the four PTOs are working out of phase. It can be seen that in this case the total power is smoother, meaning the power quality is improved. The intention is not to prioritize non-zero headings as this is not ideal operational condition for the M4 WEC. However, if the four PTOs can be intentionally designed

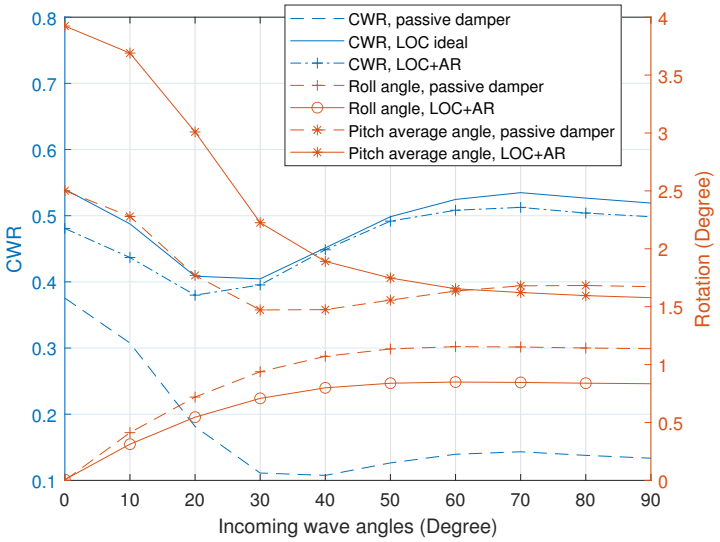

Figure 6.12: Left Y axis: CWR of passive damper and LNOC. Right Y axis, rotation motion angle (RMS value) of pitch and roll. X axis wave heading angle from 0 degrees to 90 degrees. Significant wave height $H_s = 0.04m$, peak period $T_p = 1.4s$, $\gamma = 3.3$.

to work out of phase even in zero heading, either by introducing an extra layer of control or alter the mechanical design, e.g. varies the length of beams connecting the stern floats, the power quality of the M-WEC M4 can be sufficiently improved. This is another advantage of M-WEC over S-WEC.

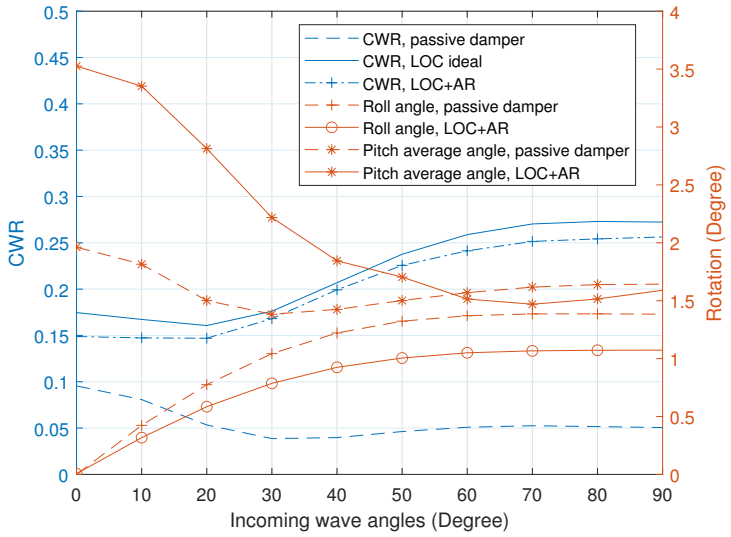

Figure 6.13: Left Y axis: CWR of passive damper and LNOC. Right Y axis, rotation motion angle (RMS value) of pitch and roll. X axis wave heading angle from 0 degrees to 90 degrees. Significant wave height $H_s = 0.04m$, peak period $T_p = 1.8s$, $\gamma = 1$.

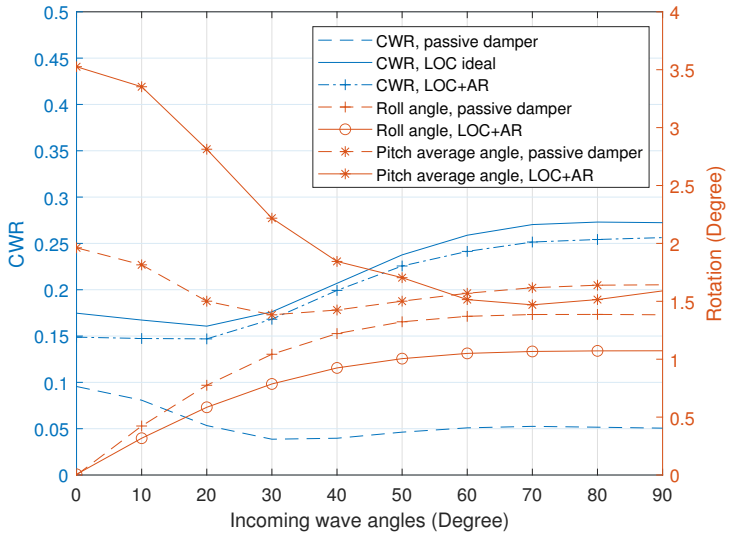

Figure 6.14: Left Y axis: CWR of passive damper and LNOC. Right Y axis, rotation motion angle (RMS value) of pitch and roll. X axis wave heading angle from 0 degrees to 90 degrees. Significant wave height $H_s = 0.04m$, peak period $T_p = 1.8s$, $\gamma = 3.3$.

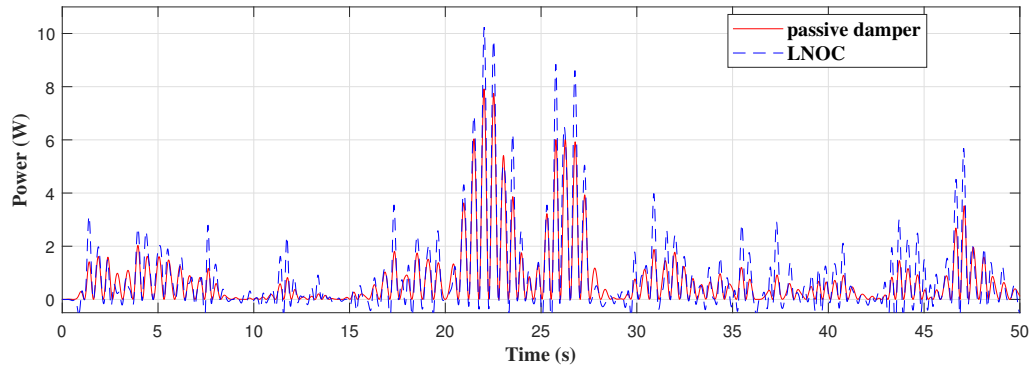

Figure 6.15: Sum of instant power from 4 PTOs. Significant wave height $H_s = 0.04m$, peak period $T_p = 1s$, $\gamma = 1$. Zero degrees heading.

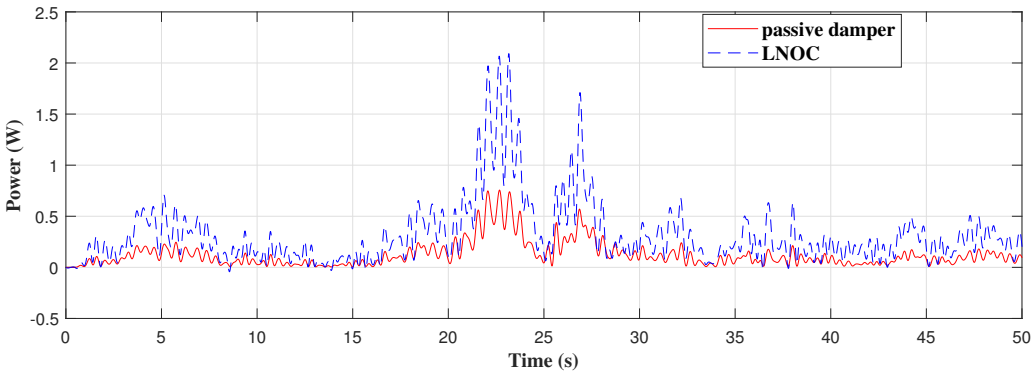

Figure 6.16: Sum of instant power from 4 PTOs. Significant wave height $H_s = 0.04m$, peak period $T_p = 1s$, $\gamma = 1$. 40 degrees heading.

Chapter 7

Conclusion and future work

In this chapter, all the presented work in this thesis is concluded, and the contribution from each chapter will be summarised. Finally, potential future directions of my research are discussed.

7.1 Conclusions

- In Chapter 2, knowledge of wave energy conversion technologies are reviewed. The differences between S-WEC and M-WEC in their theoretical power capture limit were discussed. The typical M-WEC design, M4, was then introduced. By reviewing some of the existing control strategies for WECs, I indicated that there is a gap of knowledge in this research area: most of the published control methods focus on S-WECs with simple dynamics, while the challenges for controlling M-WECs that enable higher energy conversion capacities, are not investigated. Based on these discussions, the research objective for this thesis is set up, which is to design a novel controller aiming for the M-WEC energy maximising control problem. The controller should at least have these advantages: guarantee optimum energy output, low computational burden and can handle operational constraints.

- In Chapter 3, a control-oriented state-space model is developed for the 3-float

1-1-1 M-WEC M4. The energy-based Euler-Lagrangian modelling method is adopted to provide a concise and generic mathematical description of the device's dynamics including coupling among different modes of motion. System identification and model order reduction algorithms are used to derive the state-space subsystems representing the radiation effects. There is a brief discussion on how to select the suitable sub-system order. The resulting state-space models with different orders are validated by comparing the response in time domain to those from a linear diffraction model, which has been experimentally validated. The advantage of this control-oriented modelling method is that the order of the model can be flexibly chosen to balance between model fidelity and computational efficiency. This paves the way for designing a model-based controller for the M-WEC M4.

- In Chapter 4, a linear optimal controller was designed for the M4 WEC using the discrete time format of the derived control-oriented state-space model from Chapter 3. A cost function aimed at maximising the energy output as well as penalising the soft constraints of system states and system input was adopted. The control policy is then obtained by solving the optimisation problem using dynamic programming. Numerical simulations show that the controller can effectively incorporate wave force prediction with a various prediction horizon. The CWR of the M4 WEC can be significantly improved by applying this controller, from 40% to 100% over a broad range of sea states. The controller was also shown to be relatively robust against two types of wave force prediction errors. Moreover, some useful guidelines are provided to show the readers how to optimally tuned the control parameters for better control performance.

- In Chapter 5, a comprehensive LNOC framework was proposed. Firstly, the necessity of short-term sea wave prediction in WEC control applications and some realisable solutions were discussed. Three potential realization methods for sea wave prediction are discussed and assessed comprehensively before one of them is selected. Then, two key components enabling the LNOC frame-

work, i.e. the KFRW state and wave force estimator and the AR wave force predictor, were introduced in detail. Critical factors for obtaining an stable and accurate AR model are discussed. The complete self-contained and low-cost LNOC framework is then proposed, followed by numerical simulations to demonstrate its efficacy on the M4 WEC. Results show that the AR predictor can predict future wave excitation force accurately for around $2T_p$ of time. The improvement on CWR of M4 provided by the LNOC framework is substantial.

- In Chapter 6, a different configuration of the M4 WEC, with 8 floats and 4 PTOs, was investigated. The increased of complexity of the WEC dynamic was briefly introduced. The LNOC framework was again applied to this M-WEC to improve its CWR, showing the genericness of this control method. More importantly, the overall energy conversion capacity provided by multi-PTO WEC and control was now around 2MW, which is similar to wind turbines in some sites, which is desirable for the supply of electricity to grid. The effect of off-design, arbitrary WEC headings in various incoming wave direction was studied as a sensitivity check, which provides valuable information for implementing the LNOC framework is reality. The CWR improvement in this case is again substantial. Finally, a discussion on the potential advantage of improving the power quality (P2A ratio) using multi-PTO configuration is presented.

In summary, the research objectives set up in Chapter 2 are mostly addressed. In the proposed LNOC framework, a energy maximising cost function is selected and solved by dynamic programming to guarantee optimum absorbed power for the M-WEC. Simulation results show that with sea wave prediction information incorporated, 40% to 100% energy output improvement can be obtained. Computational burden of the LNOC framework is not heavy, thanks to the extra stiffness term added to the control-oriented model to guarantee stability of the system, and thus a convergent solution can be derived from the DARE. Control parameters Q and r are there to deal with soft operational constraints. By selecting less aggressive (bigger)

value of the control parameters, the controller can operate within the allowed torque and position/velocity range to better protect the WEC system, although this will trade off some optimality from the energy output. The AR wave force predictor is shown to be robust and accurate enough for control purpose. It it shown that it can predict incoming wave force up to $2T_p$ in time. Some interesting points related to the M-WEC design and control problem are investigated as well, e.g. off-design non-zero heading performance of the M-WEC M4 with/without LNOC control; power quality can be potentially improved by co-design of M-WEC and control.

7.2 Future work

- In this thesis, the efficacy of the proposed LNOC framework on the M-WEC M4 is mainly demonstrated by numerical simulations. Experimental tank testing of the M4 incorporated with the LNOC framework would be valuable to validate these numerical results. This is planed and will be carried out later on this year in Plymouth, UK. Meanwhile, part of the the LNOC framework (with a DSWP wave predictor instead of the AR wave predictor) has been recently tested experimentally on a different M-WEC in a WEC control project supported by Wave Energy Scotland, which I have contributed to. A DC motor was controlled to provide the required torque from LNOC and the WEC motion was recorded to calculate the average absorbed power. With reliable wave force prediction, the improvement of average absorbed power compared with a passive damper was from around 40% to 120% depending on wave periods.

- In Chapter 3, although we have constrained the coordinate of WEC motion and reduced the order of the radiation subsystems, the order of the control-oriented state-space model of the M4 WEC is still relatively high (more than 100). For the off-line designed LNOC this will not cause intensive computational loads, but this would not be the case for on-line optimisation-based

control methods, like model predictive control, which might be more effective in handling operational constraints. The order of the state-space model can potentially be further decreased by applying model order reduction to the whole system, instead of only on the radiation subsystems. It would also be interesting to investigate other modelling methods, such as black box modelling, by system identification using experimental data, which might be able to construct a useful control-oriented model of lower order. Besides, due to the inherent linearity of the M4 design, the viscous damping force is negligible. This might not be the case for other M-WEC designs. The non-linearity of M-WEC can be significant, depending on the WEC structure as well as the operating sea conditions such as very high amplitude waves. Incorporating the non-linearity into the WEC dynamics when modelling and designing control methods for M-WECs is valuable.

- In Chapter 4, the linear non-causal optimal controller was derived based on a discrete-time state-space model using dynamic programming. However, the close-loop stability of the obtained controller has not been investigated theoretically. In would be interesting to study the stability of the close-loop system, and see how it relates to the controller's tuning parameter Q and R. Furthermore, when doing numerical simulations, one set of control parameters Q and R is used for all the tested sea states, for a relatively fair comparison to be made with the linear passive damper with one constant damping ratio. Nevertheless, it is valuable to investigate whether and how control performance can be further improved based on distinct tuning for various sea states.

- In Chapter 5, only one solution out of three for implementing the short-term wave prediction that performs prediction on excitation force directly was implemented. A comparison has not been made between the other two solutions that perform prediction on wave elevation. It would be interesting to quantify the differences between these methods.

- In Chapter 6, the power quality issue of WEC is briefly discussed. Indeed,

this is a very important aspect in real-time control implementation onto WEC systems. The high P2A ratio caused by active control is not ideal for mechanical to electrical power conversion system. There are many ways to tackle this issue which deserves further investigation. For example, from the control design point of view, a non-linear constraint that limits the peak absorbed power can be introduced to the control problem and model predictive control can be utilized to resolved this constraints optimal control problem. Also, a designed mechanism to enable multiple PTOs working out of phase and share the same power link is another solution coming from the WEC design perspective. Anyway, mitigating the bad power quality issue of WEC + control is a promising further research direction.

- Last but not least, the LNOC framework proposed in this thesis was compared against the most commonly used linear passive damper. It would be meaningful to compare it against other existing control strategies, such as latching control or model predictive control. Also, this research is mainly focussed on improving the wave to mechanical power conversion. A wave-to-wire model and control framework to generate electricity from ocean waves is yet to be designed. Although of profound importance, this achievement requires knowledge and cooperation from other disciplines.

Appendix A

Mass and inertia of the M4 WEC

Mass and position of centre of mass relative to the hinge point origin O for each mechanical part of the 1-3-4 M4 are shown in Table A.1. Centre of mass is relative to hinge point origin O. h (horizontal) is for x axis; t (transversal) is for y axis; v (vertical) is for z axis. Beam 1234 connect bow and mid floats. Radius is of circular cross section.

Inertia in pitch of the first 4 floats is $I_{1234} = 5.58\ kgm^2$. Inertia in pitch of each stern float is $I_5 = I_6 = I_7 = I_8 = 13.46\ kgm^2$. Inertia in roll of the whole WEC is $I_\psi = 56.51\ kgm^2$. These are used in the state-space model for numerical simulations.

Table A.1: Mass and centre of mass

Part	mass (kg)	h (m)	t (m)	v (m)	radius (m)
float 1	1.2	-1.33	0	-0.222	0.1
ballast 1	1.0	-1.33	0	-0.335	
beam 1234	0.289	-0.7	0	0.094	
float 2	1.887	0	-0.7	-0.214	0.125
ballast 2	3.0	0	-0.7	-0.327	
float 3	1.887	0	0	-0.214	0.125
ballast 3	3.0	0	0	-0.327	
float 4	1.887	0	0.7	-0.214	0.125
ballast 4	3.0	0	0.7	-0.327	
float 5	3.74	0.8	-1.05	-0.256	0.175
ballast 5	13.5	0.8	-1.05	-0.354	
beam 5	0.56	0.5	-1.05	0	
PTO 1	0.19	0.16	-1.05	-0.16	
float 6	3.74	0.8	-0.35	-0.256	0.175
ballast 6	13.5	0.8	-0.35	-0.354	
beam 6	0.56	0.5	-0.35	0	
PTO 2	0.19	0.16	-0.35	-0.16	
float 7	3.74	0.8	0.35	-0.256	0.175
ballast 7	13.5	0.8	0.35	-0.354	
beam 7	0.56	0.5	0.35	0	
PTO 3	0.19	0.16	0.35	-0.16	
float 8	3.74	0.8	1.05	-0.256	0.175
ballast 8	13.5	0.8	1.05	-0.354	
beam 8	0.56	0.5	1.05	0	
PTO 4	0.19	0.16	1.05	-0.16	

Bibliography

[1] IEA. *World Energy Balances: Overview*. Paris, 2020. URL: https://www.iea.org/reports/world-energy-balances-overview.

[2] REN21 Secretariat. *RENEWABLES 2020 GLOBAL STATUS REPORT*. Paris, France.

[3] Kester Gunn and Clym Stock-Williams. "Quantifying the global wave power resource". In: *Renewable Energy* 44 (2012), pp. 296 –304. ISSN: 0960-1481. DOI: https://doi.org/10.1016/j.renene.2012.01.101. URL: http://www.sciencedirect.com/science/article/pii/S0960148112001310.

[4] A. F. de O. Falcão. "Wave energy utilization: A review of the technologies". In: *Renewable and Sustainable Energy Reviews* 14.3 (2010), pp. 899 –918. ISSN: 1364-0321. DOI: https://doi.org/10.1016/j.rser.2009.11.003. URL: http://www.sciencedirect.com/science/article/pii/S1364032109002652.

[5] Alpaslan Aydingakko, Mohamed Mukhaini, and Salim Jassasi. "Renewable Energy Potential in Middle East and Particularly Oman case". In: Oct. 2016.

[6] J. Falnes. *Ocean Waves and Oscillating Systems: Linear Interactions Including Wave-Energy Extraction*. Cambridge University Press, 2002. DOI: 10.1017/CBO9780511754630.

[7] *AWS OCEAN ENERGY*. http://www.awsocean.com/. [Online; accessed 23-September-2019].

[8] *CorPower Ocean*. http://www.corpowerocean.com/. [Online; accessed 23-September-2019].

[9] *Seabased*. https://www.seabased.com/. [Online; accessed 23-September-2019].

[10] *OceanEnergy*. http://www.oceanenergy.ie/. [Online; accessed 23-September-2019].

[11] J.N. Newman. "Absorption of wave energy by elongated bodies". In: *Applied Ocean Research* 1.4 (1979), pp. 189 –196. ISSN: 0141-1187. DOI: https://doi.org/10.1016/0141-1187(79)90026-9. URL: http://www.sciencedirect.com/science/article/pii/0141118779900269.

[12] *Sea Power*. http://www.seapower.ie/. [Online; accessed 23-September-2019].

[13] *Mocean Energy*. https://www.mocean.energy. [Online; accessed 23-September-2019].

[14] P. Stansby et al. "Three-float broad-band resonant line absorber with surge for wave energy conversion". In: *Renewable Energy* 78 (2015), pp. 132 –140. ISSN: 0960-1481. DOI: https://doi.org/10.1016/j.renene.2014.12.057. URL: http://www.sciencedirect.com/science/article/pii/S0960148114008957.

[15] P. Stansby, E. Carpintero Moreno, and T. Stallard. "Large capacity multi-float configurations for the wave energy converter M4 using a time-domain linear diffraction model". In: *Applied Ocean Research* 68 (2017), pp. 53 – 64. ISSN: 0141-1187. DOI: https://doi.org/10.1016/j.apor.2017.07.018. URL: http://www.sciencedirect.com/science/article/pii/S0141118717302146.

[16] Stephen Salter. "Power conversion systems for ducks". In: *IN. PROC. INT. CONF. ON FUTURE ENERGY CONCEPTS, (LONDON, U.K.: JAN.30-FEB.1, 1979), LONDON, U.K., INST. ELECTR. ENGRS., 1979* (Jan. 1979).

[17] P Nebel. “Maximizing the Efficiency of Wave-Energy Plant Using Complex-Conjugate Control”. In: *Proceedings of the Institution of Mechanical Engineers, Part I: Journal of Systems and Control Engineering* 206.4 (1992), pp. 225–236. DOI: 10.1243/PIME_PROC_1992_206_338_02. eprint: https://doi.org/10.1243/PIME_PROC_1992_206_338_02. URL: https://doi.org/10.1243/PIME_PROC_1992_206_338_02.

[18] Stephen Salter, D.C. Jeffery, and Jamie Taylor. “The architecture of nodding duck wave power generators”. In: *The Naval Architect* (Jan. 1976), pp. 21–24.

[19] K Budal and J Falnes. “Optimum operation of improved wave-power converter”. In: *Mar. Sci. Commun.; (United States)* (). URL: https://www.osti.gov/biblio/7213955.

[20] Francesco Fusco and John Ringwood. “A Simple and Effective Real-Time Controller for Wave Energy Converters”. In: *Sustainable Energy, IEEE Transactions on* 4 (Jan. 2013), pp. 21–30. DOI: 10.1109/TSTE.2012.2196717.

[21] A.J. Hillis et al. “Active control for multi-degree-of-freedom wave energy converters with load limiting”. In: *Renewable Energy* 159 (2020). cited By 4, pp. 1177–1187. DOI: 10.1016/j.renene.2020.05.073. URL: https://www.scopus.com/inward/record.uri?eid=2-s2.0-85087929183&doi=10.1016%2fj.renene.2020.05.073&partnerID=40&md5=1351edeabb218d7aff80d29d77f615bc.

[22] K Budal and J Falnes. “Interacting point absorbers with controller motion.” In: *Power from Sea waves* (1980).

[23] Lars Chr. Iversen. “Numerical method for computing the power absorbed by a phase-controlled point absorber”. In: *Applied Ocean Research* 4.3 (1982), pp. 173–180. ISSN: 0141-1187. DOI: https://doi.org/10.1016/S0141-1187(82)80054-0. URL: https://www.sciencedirect.com/science/article/pii/S0141118782800540.

[24] M. Greenhow and S.P. White. “Optimal heave motion of some axisymmetric wave energy devices in sinusoidal waves”. In: *Applied Ocean Research*

19.3 (1997), pp. 141–159. ISSN: 0141-1187. DOI: https://doi.org/10.1016/S0141-1187(97)00020-5. URL: https://www.sciencedirect.com/science/article/pii/S0141118797000205.

[25] H. Eidsmoen. "Tight-moored amplitude-limited heaving-buoy wave-energy converter with phase control". In: *Applied Ocean Research* 20.3 (1998), pp. 157–161. ISSN: 0141-1187. DOI: https://doi.org/10.1016/S0141-1187(98)00013-3. URL: https://www.sciencedirect.com/science/article/pii/S0141118798000133.

[26] *Benefit of Latching Control For a Heaving Wave Energy Device In Random Sea*. Vol. All Days. International Ocean and Polar Engineering Conference. ISOPE-I-03-051. May 2003. eprint: https://onepetro.org/ISOPEIOPEC/proceedings-pdf/ISOPE03/All-ISOPE03/ISOPE-I-03-051/1870868/isope-i-03-051.pdf.

[27] A. Babarit. "A database of capture width ratio of wave energy converters". In: *Renewable Energy* 80 (2015), pp. 610 –628. ISSN: 0960-1481. DOI: https://doi.org/10.1016/j.renene.2015.02.049. URL: http://www.sciencedirect.com/science/article/pii/S0960148115001652.

[28] *A Critical Assessment of Latching As Control Strategy For Wave-Energy Point Absorbers*. Vol. All Days. International Ocean and Polar Engineering Conference. ISOPE-I-11-092. June 2011. eprint: https://onepetro.org/ISOPEIOPEC/proceedings-pdf/ISOPE11/All-ISOPE11/ISOPE-I-11-092/1668965/isope-i-11-092.pdf.

[29] Guang Li et al. "Wave energy converter control by wave prediction and dynamic programming". In: *Renewable Energy* 48 (2012), pp. 392–403. ISSN: 0960-1481. DOI: https://doi.org/10.1016/j.renene.2012.05.003. URL: https://www.sciencedirect.com/science/article/pii/S0960148112003163.

[30] Guang Li and Michael Belmont. "Model predictive control of sea wave energy converters – Part I: A convex approach for the case of a single device". In:

Renewable Energy 69 (Sept. 2014), pp. 453 –463. DOI: 10.1016/j.renene.2014.03.070.

[31] J. Cretel et al. "An Application of Model Predictive Control to a Wave Energy Point Absorber". In: *IFAC Proceedings Volumes* 43.1 (2010). 1st IFAC Conference on Control Methodologies and Technology for Energy Efficiency, pp. 267–272. ISSN: 1474-6670. DOI: https://doi.org/10.3182/20100329-3-PT-3006.00049. URL: https://www.sciencedirect.com/science/article/pii/S1474667015300719.

[32] J.A.M. Cretel et al. "Maximisation of Energy Capture by a Wave-Energy Point Absorber using Model Predictive Control". In: *IFAC Proceedings Volumes* 44.1 (2011). 18th IFAC World Congress, pp. 3714–3721. ISSN: 1474-6670. DOI: https://doi.org/10.3182/20110828-6-IT-1002.03255. URL: https://www.sciencedirect.com/science/article/pii/S1474667016441893.

[33] Jørgen Hals, Johannes Falnes, and Torgeir Moan. "Constrained Optimal Control of a Heaving Buoy Wave-Energy Converter". In: *Journal of Offshore Mechanics and Arctic Engineering* 133.1 (Nov. 2010). 011401. ISSN: 0892-7219. DOI: 10.1115/1.4001431. eprint: https://asmedigitalcollection.asme.org/offshoremechanics/article-pdf/133/1/011401/5931345/011401_1.pdf. URL: https://doi.org/10.1115/1.4001431.

[34] Ted K.A. Brekken. "On Model Predictive Control for a point absorber Wave Energy Converter". In: *2011 IEEE Trondheim PowerTech*. 2011, pp. 1–8. DOI: 10.1109/PTC.2011.6019367.

[35] Umesh A. Korde. "Latching control of deep water wave energy devices using an active reference". In: *Ocean Engineering* 29.11 (2002), pp. 1343–1355. ISSN: 0029-8018. DOI: https://doi.org/10.1016/S0029-8018(01)00093-2. URL: https://www.sciencedirect.com/science/article/pii/S0029801801000932.

[36] Changhai Liu, Qingjun Yang, and Gang Bao. "Latching control using optimal control method for a raft-type wave energy converter". In: *Ships and Offshore Structures* 13 (Jan. 2018), pp. 1–17. DOI: 10.1080/17445302.2018.1427317.

[37] J. Davidson et al. “Evaluation of Energy Maximising Control Systems for Wave Energy Converters Using OpenFOAM”. In: Cham: Springer International Publishing, 2019, pp. 157–171. ISBN: 978-3-319-60846-4. DOI: 10.1007/978-3-319-60846-4_12. URL: https://doi.org/10.1007/978-3-319-60846-4_12.

[38] M. Penalba et al. “A high-fidelity wave-to-wire simulation platform for wave energy converters: Coupled numerical wave tank and power take-off models”. In: *Applied Energy* 226 (2018), pp. 655 –669. ISSN: 0306-2619. DOI: https://doi.org/10.1016/j.apenergy.2018.06.008. URL: http://www.sciencedirect.com/science/article/pii/S0306261918308754.

[39] ChangHai Liu, QingJun Yang, and Gang Bao. “Performance investigation of a two-raft-type wave energy converter with hydraulic power take-off unit”. English. In: *Applied Ocean Research* 62.Complete (2017), pp. 139–155. DOI: 10.1016/j.apor.2016.12.002.

[40] H. Gu et al. “Drag, added mass and radiation damping of oscillating vertical cylindrical bodies in heave and surge in still water”. English. In: *Journal of Fluids and Structures* 82 (Oct. 2018), 343–356. ISSN: 0889-9746. DOI: 10.1016/j.jfluidstructs.2018.06.012.

[41] Z. Yu and J. Falnes. “State-space modelling of a vertical cylinder in heave”. In: *Applied Ocean Research* 17.5 (1995), pp. 265 –275. ISSN: 0141-1187. DOI: https://doi.org/10.1016/0141-1187(96)00002-8. URL: http://www.sciencedirect.com/science/article/pii/0141118796000028.

[42] H. Santo et al. “Extreme motion and response statistics for survival of the three-float wave energy converter M4 in intermediate water depth”. In: *Journal of Fluid Mechanics* 813 (2017), 175–204. DOI: 10.1017/jfm.2016.872.

[43] C.H. Lee and J. N. Newman. “WAMIT – User manual version 7.0”. In: *WAMIT Inc, Chestnut Hill, Massachusetts*. 2013.

[44] E. Kristiansen, A. Hjulstad, and O. Egeland. "State-space representation of radiation forces in time-domain vessel models". In: *Ocean Engineering* 32.17 (2005), pp. 2195 –2216. ISSN: 0029-8018. DOI: https://doi.org/10.1016/j.oceaneng.2005.02.009. URL: http://www.sciencedirect.com/science/article/pii/S0029801805000946.

[45] M.G. Safonov and R.Y. Chiang. "A Schur method for balanced-truncation model reduction". In: *IEEE Transactions on Automatic Control* 34.7 (1989), pp. 729–733. DOI: 10.1109/9.29399.

[46] Richard Bellman. "The theory of dynamic programming". In: *Bulletin of the American Mathematical Society* 60.6 (1954), pp. 503 –515. DOI: bams/1183519147. URL: https://doi.org/.

[47] S. Zhan and G. Li. "Linear Optimal Noncausal Control of Wave Energy Converters". In: *IEEE Transactions on Control Systems Technology* 27.4 (2019), pp. 1526–1536. DOI: 10.1109/TCST.2018.2812740.

[48] H. Zienkiewicz M. Pourzanjani J. Flower Morris E. and M. Belmont. "Techniques for sea-state prediction." In: *Manoeuvring and Control of Marine Craft: Proceedings of the Second International Conference* (1992). ISSN: P. A. Wilson, Ed., WIT Press, 547–571.

[49] M.R. Belmont et al. "Filters for linear sea-wave prediction". In: *Ocean Engineering* 33.17 (2006), pp. 2332–2351. ISSN: 0029-8018. DOI: https://doi.org/10.1016/j.oceaneng.2005.11.011. URL: https://www.sciencedirect.com/science/article/pii/S0029801806000205.

[50] Michael Belmont et al. "An Examination of the Feasibility of Linear Deterministic Sea Wave Prediction in Multidirectional Seas Using Wave Profiling Radar: Theory, Simulation, and Sea Trials". In: *Journal of Atmospheric and Oceanic Technology* 31 (July 2014), pp. 1601–1614. DOI: 10.1175/JTECH-D-13-00170.1.

[51] Francesco Fusco and John Ringwood. “Short-Term Wave Forecasting for Real-Time Control of Wave Energy Converters”. In: *Sustainable Energy, IEEE Transactions on* 1 (Aug. 2010), pp. 99 –106. DOI: 10.1109/TSTE.2010.2047414.

[52] Marco P. Schoen, Jørgen Hals, and Torgeir Moan. “Wave Prediction and Robust Control of Heaving Wave Energy Devices for Irregular Waves”. In: *IEEE Transactions on Energy Conversion* 26.2 (2011), pp. 627–638. DOI: 10.1109/TEC.2010.2101075.

[53] Yerai Peña-Sanchez, Alexis Mérigaud, and John V. Ringwood. “Short-Term Forecasting of Sea Surface Elevation for Wave Energy Applications: The Autoregressive Model Revisited”. In: *IEEE Journal of Oceanic Engineering* 45.2 (2020), pp. 462–471. DOI: 10.1109/JOE.2018.2875575.

[54] H. Akaike. “A new look at the statistical model identification”. In: *IEEE Transactions on Automatic Control* 19.6 (1974), pp. 716–723. ISSN: 0018-9286. DOI: 10.1109/TAC.1974.1100705.

[55] Y. Peña-Sanchez, A. Mérigaud, and J. V. Ringwood. “Short-Term Forecasting of Sea Surface Elevation for Wave Energy Applications: The Autoregressive Model Revisited”. In: *IEEE Journal of Oceanic Engineering* (2018), pp. 1–10. ISSN: 0364-9059. DOI: 10.1109/JOE.2018.2875575.

[56] Steven M Kay. *Modern Spectral Estimation: Theory and Application*. Englewood Cliffs, N.J. : Prentice-Hall, ©1988.

[57] H. . Nguyen and P. Tona. “Wave Excitation Force Estimation for Wave Energy Converters of the Point-Absorber Type”. In: *IEEE Transactions on Control Systems Technology* 26.6 (2018), pp. 2173–2181. ISSN: 1063-6536. DOI: 10.1109/TCST.2017.2747508.

[58] Jonas Sjolte, Gaute Tjensvoll, and Marta Molinas. “All-electric Wave Energy Converter array with energy storage and reactive power compensation

for improved power quality". In: *2012 IEEE Energy Conversion Congress and Exposition (ECCE)*. 2012, pp. 954–961. DOI: 10.1109/ECCE.2012.6342716.

[59] Jonas Sjolte, Gaute Tjensvoll, and Marta Molinas. "All-electric wave energy converter connected in array with common DC-link for improved power quality". In: *2012 3rd IEEE International Symposium on Power Electronics for Distributed Generation Systems (PEDG)*. 2012, pp. 431–436. DOI: 10.1109/PEDG.2012.6254038.